NASA/TP-2019-220419

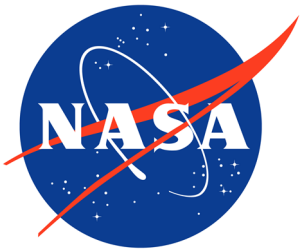

The Badhwar-O'Neill 2020 Model

Tony C. Slaba
Langley Research Center, Hampton, Virginia

Kathryn Whitman
University of Houston, Houston, Texas

November 2019

NASA STI Program . . . in Profile

Since its founding, NASA has been dedicated to the advancement of aeronautics and space science. The NASA scientific and technical information (STI) program plays a key part in helping NASA maintain this important role.

The NASA STI program operates under the auspices of the Agency Chief Information Officer. It collects, organizes, provides for archiving, and disseminates NASA's STI. The NASA STI program provides access to the NTRS Registered and its public interface, the NASA Technical Reports Server, thus providing one of the largest collections of aeronautical and space science STI in the world. Results are published in both non-NASA channels and by NASA in the NASA STI Report Series, which includes the following report types:

- TECHNICAL PUBLICATION. Reports of completed research or a major significant phase of research that present the results of NASA Programs and include extensive data or theoretical analysis. Includes compilations of significant scientific and technical data and information deemed to be of continuing reference value. NASA counter-part of peer-reviewed formal professional papers but has less stringent limitations on manuscript length and extent of graphic presentations.

- TECHNICAL MEMORANDUM. Scientific and technical findings that are preliminary or of specialized interest, e.g., quick release reports, working papers, and bibliographies that contain minimal annotation. Does not contain extensive analysis.

- CONTRACTOR REPORT. Scientific and technical findings by NASA-sponsored contractors and grantees.

- CONFERENCE PUBLICATION. Collected papers from scientific and technical conferences, symposia, seminars, or other meetings sponsored or co-sponsored by NASA.

- SPECIAL PUBLICATION. Scientific, technical, or historical information from NASA programs, projects, and missions, often concerned with subjects having substantial public interest.

- TECHNICAL TRANSLATION. English-language translations of foreign scientific and technical material pertinent to NASA's mission.

Specialized services also include organizing and publishing research results, distributing specialized research announcements and feeds, providing information desk and personal search support, and enabling data exchange services.

For more information about the NASA STI program, see the following:

- Access the NASA STI program home page at http://www.sti.nasa.gov

- E-mail your question to help@sti.nasa.gov

- Phone the NASA STI Information Desk at 757-864-9658

- Write to:
  NASA STI Information Desk
  Mail Stop 148
  NASA Langley Research Center
  Hampton, VA 23681-2199

NASA/TP-2019-220419

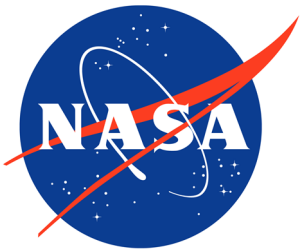

The Badhwar-O'Neill 2020 Model

Tony C. Slaba
Langley Research Center, Hampton, Virginia

Kathyrn Whitman
University of Houston, Houston, Texas

National Aeronautics and
Space Administration

Langley Research Center
Hampton, Virginia 23681-2199

November 2019

Available from:

NASA STI Program / Mail Stop 148
NASA Langley Research Center
Hampton, VA 23681-2199
Fax: 757-864-6500

Contents

Figures

Tables

Appendix A Tables

Appendix B Tables

Appendix C Tables

Appendix C Figures

Appendix D Figures

Abstract

The Badhwar-O'Neill (BON) model has been used for some time to describe the galactic cosmic ray (GCR) environment encountered in deep space by astronauts and sensitive electronics. The most recent version of the model, BON2014, was calibrated to available measurements to reduce model errors for particles and energies of significance to astronaut exposure. Although subsequent studies showed the model to be reasonably accurate for such applications, modifications to the sunspot number (SSN) classification system and a large number of new high-precision measurements suggested the need to develop an improved and more capable model. In this work, the BON2020 model is described. The new model relies on daily integral flux from the Advanced Composition Explorer Cosmic Ray Isotope Spectrometer (ACE/CRIS) to describe solar activity. For time periods not covered by ACE/CRIS, the updated international SSN database is used. Parameters in the new model are calibrated to available data, which includes the new Alpha Magnetic Spectrometer (AMS-02) and Payload for Antimatter Matter Exploration and Light-nuclei Astrophysics (PAMELA) high-precision measurements. It is found that the BON2020 model is a significant improvement over BON2014. Systematic errors associated with BON2014 have been removed. The average relative error of the BON2020 model compared to all available measurements is found to be <1%, and BON2020 is found to be within $\pm$15% of a large fraction of the available measurements (26,269 of 27,646 $\rightarrow$ 95%).

Introduction

The galactic cosmic ray (GCR) environment in space is a complex spectrum of ions and energies that pose a significant risk to astronauts and sensitive electronics. Accurately and efficiently describing this radiation environment is therefore vital for mission planning, shield design, and astronaut safety. The Badhwar-O'Neill (BON) model was created to meet this need and is periodically updated as new data become available [Aguilar et al. 2017, 2018a-c; Adriani et al. 2011, 2013] and improved methods for calibration and uncertainty quantification are developed [Slaba and Blattnig 2014a,b; Slaba et al. 2014].

Although differences between past versions of the BON model exist, all of them rely on the same basic formalism [O'Neill et al. 2015]. First, the local interstellar spectrum (LIS) for each ion is described by a simple parametric function. Next, the state of the heliosphere at any time and radial distance from the Sun is described by a diffusion coefficient, which depends, in part, on the time-dependent solar modulation potential, $\phi(t)$ (MV). The modulation potential is obtained through empirical relationships to solar indices such as neutron monitor counts or sunspot number (SSN). Finally, the LIS is transported to 1 AU using a numerical solution to the steady-state, spherically symmetric Fokker-Planck equation with the aforementioned diffusion coefficient. The main differences between the various versions of the BON model are found in the solar indices used to derive modulation potential and the data and methods used to calibrate free parameters in the LIS function for each ion. The most recent version, BON2014 [O'Neill et al. 2015], used SSN to obtain the modulation potential, and parameter calibration was guided by sensitivity studies highlighting the energies and ions of interest to space radiation protection [Slaba and Blattnig 2014a].

In ~2015 the Royal Observatory of Belgium revised their SSN classification system [Clette et al. 2016]. The resulting SSN database, referred to as version 2 (V2), contained markedly different values than the original database (V1). The change in SSN values had a significant impact on $\phi(t)$ and the subsequent behavior of the GCR energy spectrum predicted by BON2014. The observatory abandoned the V1 database after May 2015, thereby leaving no means of determining $\phi(t)$ from the original SSN classification system beyond the termination date. The V2 values could also not be used directly in BON2014 without completely re-deriving the $\phi(t)$ relationship. Further analysis revealed that between January 2014 and May 2015, the V1 and V2 values differed fairly consistently by a multiplicative factor of ~0.7. To enable the use of BON2014 beyond the May 2015 termination date of the V1 database, the V2 values were simply scaled by 0.7. This provided a temporary, albeit suboptimal, extension of the V1 database to current dates. Although this approach continues to be used for the BON2014 model, it is clear that more robust methods of determining $\phi(t)$ are needed.

Along with the SSN classification system changing, there has been a significant number of new and important measurements from the Alpha Magnetic Spectrometer (AMS-02) [Aguilar et al. 2015a,b, 2017, 2018a-c] and the Payload for Antimatter Matter Exploration and Light-nuclei Astrophysics (PAMELA) [Adriani et al. 2011, 2013, 2017; Martuicci et al. 2018]. Some of this data has been used in comparative studies with available GCR models [Norbury et al. 2018, Whitman et al. 2019], revealing areas where spectral characteristics and solar modulation effects can be improved. Both experiments have also published GCR measurements on monthly timescales covering the descending phase of solar cycle 23 and the ascending phase of cycle 24. The AMS-02 collaboration released monthly proton and helium data from May 2011 to May 2017 [Aguilar et al. 2018c], and the

PAMELA group released monthly proton data from October 2006 to January 2014 [Adriani et al. 2013, Martucci et al. 2018]. Since GCR protons and helium account for ~70% of the astronaut exposure behind shielding [Slaba and Blattnig 2014a], it is clear that these new datasets fill an important measurement gap for space radiation protection and create a new opportunity to improve models.

In this work, the BON2020 model is presented. This updated model contains new methods to compute $\phi(t)$, and the new data from AMS-02 and PAMELA are utilized in LIS parameter calibration. Using previously described methods for uncertainty quantification [Slaba et al. 2014], it is shown that BON2020 is significantly better than its predecessor, BON2014. Uncertainty propagation methods are used to show that these updates reduce propagated errors in effective dose equivalent as compared to BON2014. We refrain from making direct comparisons to other GCR models, as these models have not yet been updated as a result of the new measurements. It is expected that all of the models will eventually account for the new data, at which time, a fair comparison may be made.

Model Description

The BON model is based on a numerical solution to the Fokker-Planck equation accounting for diffusion, convection, and adiabatic deceleration under the assumptions of a quasi-steady state and spherically symmetric interplanetary medium [O'Neill et al. 2015]. The boundary condition for the Fokker-Planck equation is the LIS which is described within the model for each ion as

$$f_{\mathrm{LIS}}(T) = j_0 \beta^{\delta} (T + m)^{-\gamma}, \tag{1}$$

where T is the ion kinetic energy (MeV/n), m is the proton rest mass (MeV), β is the ion velocity relative to the speed of light, and j_0, γ, and δ are free parameters for each ion. The units of f_{LIS} are particles/(m^2-MeV/n-sr-sec). The values of j_0 and γ fix the magnitude and high-energy slope of the GCR spectrum for each ion. The δ parameter controls the lower energy behavior in conjunction with the solar modulation potential.

The state of the heliosphere at any radial distance, r, and time, t, is described by the diffusion coefficient, κ, evaluated as

$$\frac{\kappa(r,t)}{V_{sw}} = \frac{\beta R k_0}{\phi(t) V_{sw}} \left[1 + \left(\frac{r}{r_0} \right)^2 \right], \tag{2}$$

where R is the ion rigidity (MV), $\phi(t)$ the solar modulation potential, V_{sw} = 400 km/s is the solar wind speed (specified as a constant), r_0 = 4 AU, and k_0 = 8.8×10^{20} cm^2/s. The values selected for V_{sw}, r_0, and k_0 have been discussed elsewhere [O'Neill 2006, 2010] and were left unchanged for BON2020. Mertens et al. [2013] describe the theoretical basis for the functional form of equation (2).

The overall mechanism of particle transport is also unchanged in BON2020. Mertens et al. [2013] provide a complete derivation and discussion of the transport equation; however, the numerical methods used to solve the Fokker-Planck equation have not been previously described in detail, and therefore, a full description is given here.

The following details apply to BON2020, BON2014, and all previous versions of the Badhwar-O'Neill model. In order to produce modulated spectra at Earth (1 AU), a LIS is generated for all ions at the edge of the heliosphere, assumed to be located at 100 AU. This spectrum is transported to 1 AU according to the particle transport equation, first proposed by Parker [1965] and written by Fisk [1970] in the form of a Fokker-Planck equation, given by

$$\frac{1}{r^2}\frac{\partial}{\partial r}(r^2 V_{sw} U) - \left[\frac{1}{3r^2}\frac{\partial}{\partial r}(r^2 V_{sw}) \right] \left[\frac{\partial}{\partial T}(\alpha T U) \right] = \frac{1}{r^2}\frac{\partial}{\partial r}\left(r^2 \kappa \frac{\partial U}{\partial r} \right), \tag{3}$$

where r is the distance from the Sun, $U(r,T)$ is the omnidirectional particle density distribution, and α = (T+2m)/(T+m). As mentioned above, this equation assumes a quasi-steady, spherically symmetric heliosphere and includes the effects of convection of particles with the solar wind, adiabatic cooling due to the expansion of the solar wind, and diffusion of particles due to scattering off irregularities in the magnetic field.

As recommended by Fisk [1970], the following substitution is made

$$u(r,T) = \sqrt{r}\,U(r,T)\,, \tag{4}$$

so that equation (3) becomes

$$\frac{1}{r^2}\frac{\partial}{\partial r}(r^{3/2}V_{sw}u) - \left[\frac{1}{3r^2}\frac{\partial}{\partial r}(r^2V_{sw})\right]\left[\frac{\partial}{\partial T}(\alpha T r^{-1/2}u)\right] = \frac{1}{r^2}\frac{\partial}{\partial r}\left[r^2\kappa\frac{\partial}{\partial r}(r^{-1/2}u)\right]. \tag{5}$$

Based on the assumption that the solar wind speed, V_{sw}, is constant, equation (5) simplifies to

$$V_{sw}\frac{1}{r^2}\frac{\partial}{\partial r}(r^{3/2}u) - V_{sw}\frac{2}{3r^{3/2}}\left[\frac{\partial}{\partial T}(\alpha T u)\right] = \frac{1}{r^2}\frac{\partial}{\partial r}\left[r^2\kappa\frac{\partial}{\partial r}(r^{-1/2}u)\right]. \tag{6}$$

Multiplying by r^2 and dividing by V_{sw} reduces equation (6) to

$$\frac{\partial}{\partial r}(r^{3/2}u) - \frac{2}{3}r^{1/2}\left[\frac{\partial}{\partial T}(\alpha T u)\right] = \frac{\partial}{\partial r}\left[r^2\tilde{\kappa}\frac{\partial}{\partial r}(r^{-1/2}u)\right], \tag{7}$$

where $\tilde{\kappa} = \kappa \,/\, V_{sw}$. After expanding all of the terms in equation (7), grouping like-derivatives, and simplifying, one obtains

$$\left[\frac{2}{3}\alpha T\right]\frac{\partial u}{\partial T} = \left[-\tilde{\kappa}r\right]\frac{\partial^2 u}{\partial r^2} + \left[r - \tilde{\kappa} - r\frac{\partial\tilde{\kappa}}{\partial r}\right]\frac{\partial u}{\partial r} + \left[\frac{1}{2}\frac{\partial\tilde{\kappa}}{\partial r} + \frac{\tilde{\kappa}}{4r} + \frac{3}{2} - \frac{2}{3}\alpha - \frac{2}{3}T\frac{\partial\alpha}{\partial T}\right]u\ . \tag{8}$$

The transport equation is now the form of a parabolic partial differential equation

$$p(r,T)\frac{\partial u}{\partial T} = f(r,T)\frac{\partial^2 u}{\partial r^2} + g(r,T)\frac{\partial u}{\partial r} + q(r,T)u\ , \tag{9}$$

where the functions p, f, g, and q are the bracketed terms in equation (8). Gleeson and Urch [1971] show that the Crank-Nicholson method can be applied to discretize equation (9) and produce the finite difference equation

$$\begin{aligned}\frac{p_i^j}{h_T}(u_i^{j+1} - u_i^j) = {} & \frac{f_i^j}{2h_r^2}(u_{i+1}^{j+1} - 2u_i^{j+1} + u_{i-1}^{j+1} + u_{i+1}^j - 2u_i^j + u_{i-1}^j) \\ & + \frac{g_i^j}{4h_r}(u_{i+1}^j + u_{i+1}^{j+1} - u_{i-1}^j - u_{i-1}^{j+1)} \\ & + q_i^j\frac{(u_i^j + u_i^{j+1})}{2}\ ,\end{aligned} \tag{10}$$

where i is the numerical step in radius, r, with step size h_r, and j is a step in kinetic energy, T, with step size h_T. After collecting like-terms, equation (10) forms a tridiagonal matrix which is solved analytically via the tridiagonal matrix algorithm (Thomas algorithm) to obtain the flux spectrum at 1 AU.

The level of modulation is controlled by the single parameter, $\phi(t)$, in the diffusion coefficient. As described in the introduction, various solar indices have been used to determine $\phi(t)$, and BON2014 relied on SSN with an empirical delay function [Nymmik 2000] that accounts for the time-lag between observed sunspots and magnetic field disturbances capable of modulating GCR spectra near Earth. Because the BON model relies on a one-dimensional transport equation, the time delay also serves as a proxy for the three-dimensional drift effects that cause positive particles to drift into the heliosphere over the poles when the sun's polarity is positive and along the heliospheric current sheet when the sun's polarity is negative. This drift effect, typically called the charge-sign drift

effect, is responsible for the alternating peaked and plateau shapes observed in neutron monitor and other GCR data from one solar cycle to the next [Lockwood et al. 2001, Potgieter 2014]. The two different paths that GCR particles take into the heliosphere (over the solar poles or along the heliospheric current sheet) affect the timescales on which particles will start to modulate at Earth following changes in the solar magnetic field. Because this is a 3D effect, it cannot be modeled directly by BON, however the time-lag function within the model is constructed to treat positive and negative solar cycles differently, serving to approximate the drift effect and produce alternating peaked and plateau solar cycles.

Comparison against data from the Advanced Composition Explorer Cosmic Ray Isotope Spectrometer (ACE/CRIS) as a function of time revealed this approach to be reasonably accurate, although moderate uncertainties in excess of 20% were found in some time periods [O'Neill et al. 2015]. It is important to note that in most circumstances, the BON model is evaluated by specifying mission start and end dates. The function relating SSN to ϕ is integrated over this time period to obtain an average value of ϕ to be used in equation (2). Alternatively, a value of ϕ may be input directly into the model, thereby bypassing the dependence on SSN or any other solar index.

Parameter Calibration

For BON2020, the two primary goals were to develop a more descriptive and robust solar modulation function, $\phi(t)$, and to utilize the new AMS-02 [Aguilar et al. 2015a,b, 2017, 2018a-c] and PAMELA [Adriani et al. 2011, 2013, 2017; Martucci et al. 2018] data sources to re-calibrate the LIS parameters. More specifically, for the solar modulation potential, we wanted to extend the capability of the model to utilize either ACE/CRIS data or SSN. Although it is expected ACE/CRIS data should provide a better description of solar activity than SSN for the applications in which the BON model is used, there are still advantages in using SSN. For example, space radiation protection studies often consider historical solar epochs (e.g. 1977 solar minimum) over which ACE/CRIS data is unavailable.

This section is organized as follows. First, the computational tools used to determine ϕ from ACE/CRIS integral flux and SSN are described. These tools are utilized in the LIS parameter calibration and are therefore described first. Next, the multi-step parameter calibration procedure developed for ions between Z = 5 and $Z = 28$ is discussed. Finally, the modified procedure for $Z = 1 – 4$ ions is defined. Specific results are shown and discussed for $Z = 8$ throughout this section for illustrative purposes.

$\phi_Z(t)$ from ACE/CRIS

ACE/CRIS measures low energy (<500 MeV/n) ions between $Z = 5$ and $Z = 28$ that may be used as a proxy for solar modulation. For example, Matthia et al. [2013] used the ACE/CRIS carbon flux in a specified energy range to define solar modulation in their model. Corti et al. [2016, 2019] analyzed BESS and AMS-02 data and found that protons and helium have distinct modulation characteristics in some epochs due to differing mass-to-charge ratios (which therefore affects the β term in the diffusion coefficient). This suggests that a single data source (e.g. ACE/CRIS data for a single ion) may not precisely specify solar modulation for all ions. To account for this, Z-dependent data from ACE/CRIS may be used to define a time-dependent solar modulation potential function for each ion, referred to as $\phi_Z(t)$. Oxygen ($Z = 8$) is used in this section as an example to help describe the computational procedures.

First, we utilize the BON2014 LIS parameters for oxygen ($j_0 = 1.50\times10^{-6}$, $\gamma = 2.725$, $\delta = -1.9$) and evaluate the model over a range of input ϕ values in the interval [100, 2000]. This interval extends over the range of ϕ values estimated for the past 250 years from SSN. The resulting fluxes are integrated over the ACE/CRIS energy bands to provide model-generated integral flux as a function of ϕ. The 27 day average integral fluxes measured by ACE/CRIS are then compared to the model-generated values, as shown in Figure 1. From this comparison, a value ϕ can be determined that provides the best agreement between the model and each of the ACE/CRIS measurements. Figure 2 shows the optimal ϕ values obtained from this analysis plotted as a function of ACE/CRIS integral flux. The ACE/CRIS integral flux was calculated by multiplying the differential fluxes in each energy bin of the data set by their bin widths and summing across all bins.

The data in Figure 2 were found to be well-described by the simple function

$$\phi_{fit}(F_{\mathrm{ACE}}; a, b) = \left[a - b \cdot \ln F_{\mathrm{ACE}} \right]^2 , \tag{11}$$

where F_{ACE} is the integral ACE/CRIS flux, and a and b are fit parameters. For the oxygen data shown in Figure 2, it was found that $a = 52.51$, $b = 6.50$, and the fitting produced a coefficient of determination value of $r^2 = 0.99999126$ (perfect agreement corresponds to $r^2 = 1$). The computational procedure for determining the optimal ϕ may be repeated for each ion between $Z = 5$ and $Z = 28$ resulting in a unique solar modulation function for each Z.

Since F_{ACE} is easily obtained from the ACE/CRIS data set as a function of time for a given ion, the time-dependent solar modulation potential may be more generally written as

$$\begin{aligned} \phi_Z(t) &\equiv \phi_{fit}[F_{\mathrm{ACE}}(t,Z); a_Z, b_Z] \\ &= \left[a_Z - b_Z \cdot \ln F_{\mathrm{ACE}}(t,Z)\right]^2 , \end{aligned} \tag{12}$$

where the Z-dependence of the a and b parameters has been made explicit for clarity. This approach produces a distinct value of ϕ for each ion and is markedly different than past versions of the BON model where a common ϕ was defined for all ions.

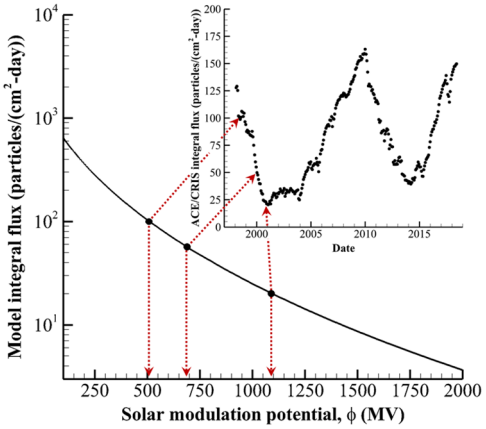

Figure 1. Comparison of model integral flux as a function of ϕ to ACE/CRIS integral flux as a function of time for oxygen.

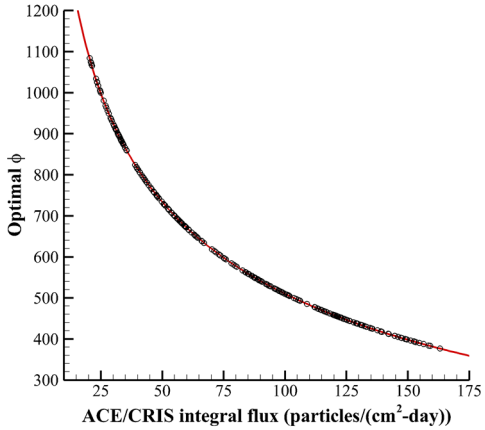

Figure 2. Optimal ϕ as a function of ACE/CRIS integral flux for oxygen. The value of ϕ shown in the plot provides excellent agreement between the model-generated integral flux and ACE/CRIS integral flux. The solid line through the data points is a parametric fit given by equation (11).

$\phi_Z(t)$ from ACE/CRIS oxygen flux

Driving the modulation of each ion directly by its associated ACE/CRIS integral flux has the benefit of linking the model results directly with real measurements of the GCR environment for a specified mission duration.

This approach becomes difficult to interpret, however, if the model needs to be evaluated with a prescribed level of solar modulation (i.e. input ϕ) instead of mission dates. In this case, a user would need to know the value of ϕ for all GCR ions, which adds significant complexity and possibly confusion to the model.

A simpler approach is to link the behavior of all ions directly to ACE/CRIS oxygen. We first consider the correlation between ACE/CRIS integral oxygen flux and all other ions. An example is shown in Figure 3 for oxygen and silicon where a high degree of correlation between the ions is observed. The solid line in the plot was obtained from linear regression (r^2 = 0.951), and the dashed lines show that a majority of the silicon flux values are within $\pm$15% of the simple linear fit. The regression coefficients between ACE/CRIS integral oxygen flux and all other ions between Z = 5 and Z = 28 were computed and are given in Appendix A.

The computational procedure for determining $\phi_Z(t)$ from only ACE/CRIS integral oxygen flux is described as follows. For a given set of input mission dates, the average ACE/CRIS integral oxygen flux is determined. The regression coefficients from Appendix A are used to estimate all other ACE/CRIS integral ion fluxes between Z = 5 and Z = 28. These approximate integral flux values are inserted into equation (12) to obtain $\phi_Z(t)$. In cases where the solar modulation potential, instead of mission dates, are specified for model evaluation, only a single input ϕ value is required. In this case, the value is interpreted by the model as the oxygen solar modulation potential. The inverse of equation (11), given as

$$F_{ACE}(\phi_8; a_8, b_8) = \exp\left[\frac{a_8 - \sqrt{\phi_8}}{b_8}\right], \tag{13}$$

is evaluated to determine the associated ACE/CRIS oxygen integral flux value. The regression coefficients from Appendix A are employed to estimate the ACE/CRIS integral fluxes for all other ions. Finally, these approximate integral flux values are inserted back into equation (12) to obtain $\phi_Z(t)$. This computational procedure guarantees self-consistent results whether mission dates or a specific level of solar modulation are considered.

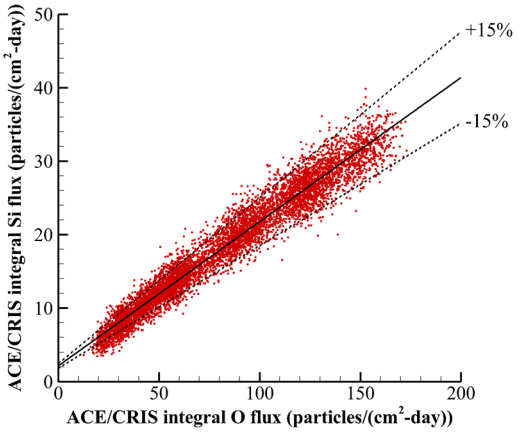

Figure 3. Correlation plot for ACE/CRIS integral silicon and oxygen flux. The solid line is the best-fit linear regression.

$\phi_Z(t)$ from SSN

Figure 4 shows the relationship between V2 SSN and ACE/CRIS integral oxygen flux as a function of time. Using the methods from BON2014, the monthly SSN values have been smoothed over a 12 month forward window and are plotted as a function of the delayed-time determined from the empirical model of Nymmik [2000]. Also shown in the plot is a parametric fit that relates time-delayed SSN values to ACE/CRIS integral oxygen flux. The function is given as

$$F_8(\mathrm{SSN}) = c_1 + c_2\,\mathrm{SSN}(\ln \mathrm{SSN}) + c_3(\ln \mathrm{SSN})^2 + c_4\sqrt{\mathrm{SSN}}\,, \tag{14}$$

where c_1 = 255.3375, c_2 = 0.22131531, c_3 = 20.95727, and c_4 = -74.465603. In the time period covered by ACE/CRIS, the parametric fit provides a reasonable estimate for the measured data (r^2 = 0.915).

To obtain the oxygen solar modulation function from time-delayed SSN, equation (14) is evaluated to estimate the ACE/CRIS oxygen flux, and the solar modulation potential is determined from equation (12). Note that the parametric function in equation (14) depends only on the time-delay function of Nymmik [2000], but not on the LIS parameters or theoretical formalism of the BON model.

The computational procedure for determining $\phi_Z(t)$ from SSN for each ion is described as follows. For a given set of input mission dates, the time-delayed average SSN is computed (exactly the same as in BON2014). The average SSN value and equation (14) are used to estimate the associated ACE/CRIS integral oxygen flux value, F_8. The procedure described in the previous section for obtaining $\phi_Z(t)$ from ACE/CRIS integral oxygen flux is then carried out.

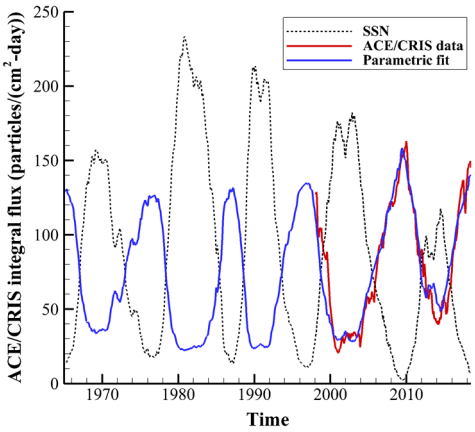

Figure 4. ACE/CRIS integral oxygen flux and V2 SSN as a function of time.

$\phi_Z(t)$ Summary

For ions between Z = 5 and Z = 28, the solar modulation potential is obtained from ACE/CRIS data, if available. If the input mission dates fall outside the time-period covered by ACE/CRIS, the solar modulation potential is determined from the V2 SSN values which extend from the year ~1750 to present day. The oxygen solar modulation potential is used for ions between Z = 1 and Z = 4.

Parameter Calibration (Z = 5 – 28)

The computational procedure outlined in this section was used to calibrate the three LIS parameters (j_0, γ, δ) for each ion. We begin by selecting the BON2014 LIS parameters j_0, γ, and δ as the initial guesses and label them as $j^{(1)}$, $\gamma^{(1)}$, and $\delta^{(1)}$. The optimal ϕ is determined using the methods outlined in the previous sub-sections using the initial specification of the LIS parameters. This step provides a solar modulation function that ensures good agreement between the model and measurement data that are sensitive to solar activity.

The parameters j_0 and γ set the magnitude and high-energy slope of the LIS and ideally would be calibrated against measurements taken at sufficiently high energy to be insensitive to solar activity; however, gaps in the measurement database make this difficult in practice. These parameters are therefore calibrated using data extending down to 1.5 GeV/n, thereby increasing the amount of available data but introducing moderate dependence on solar activity. Fortunately, the first step in this process provides a solar modulation potential ensuring near perfect agreement between the model and ACE/CRIS for the selected value of δ. This also allows j_0 and γ to be calibrated against available data while maintaining a reliable description of solar modulation effects.

To perform the calibration for j_0 and γ, the model is evaluated over a broad range of j_0 and γ values and compared to selected measurements. The following error metrics are considered

$$R_D = \frac{1}{N}\sum_{i=1}^{N}\frac{f_{\mathrm{mod}}^{(i)} - f_{\mathrm{meas}}^{(i)}}{f_{\mathrm{meas}}^{(i)}} , \tag{15}$$

$$R_{|D|} = \frac{1}{N}\sum_{i=1}^{N}\frac{\left|f_{\mathrm{mod}}^{(i)} - f_{\mathrm{meas}}^{(i)}\right|}{f_{\mathrm{meas}}^{(i)}}\ , \tag{16}$$

$$\chi^2 = \frac{1}{N}\sum_{i=1}^{N}\frac{\left[f_{\mathrm{mod}}^{(i)} - f_{\mathrm{meas}}^{(i)}\right]^2}{f_{\mathrm{meas}}^{(i)}}\ , \tag{17}$$

where f_{mod} and f_{meas} are the model and measured fluxes, respectively, and N denotes the total number of measurements in energy bins found in a prescribed energy range. The error metrics were computed separately for measurements covering the energy range 1.5 – 4 GeV/n and measurements covering the energy range above 4 GeV/n. This yielded six error metrics for each pair of j_0 and γ values. The average errors associated with each j_0 and γ pair were sorted by rank, and an average rank was computed by giving equal weight to the six metrics. The combination of parameters giving rise to the best average rank was identified as the optimal solution. It was found that separating the energy domain consistent with prior sensitivity studies [Slaba and Blattnig 2014a] and considering three error metrics instead of one provided better results that were less likely to introduce systematic model errors. The optimal parameter pair is labeled as $j^{(2)}$ and $\gamma^{(2)}$. A comparison of the oxygen flux computed by BON2014 and the corrected model to AMS-02 measurements [Aguilar et al. 2017] is shown in Figure 5. It can be seen that the corrected model is in excellent agreement with AMS-02 and is clearly an improvement from the BON2014 result.

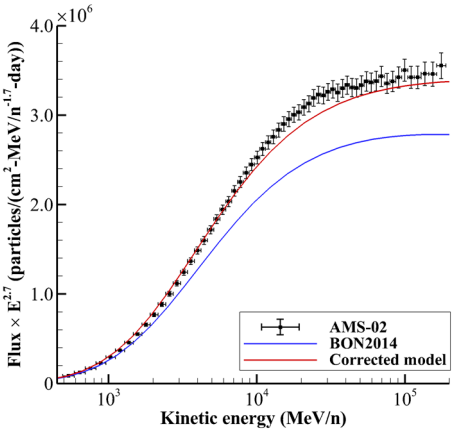

Figure 5. Comparison of oxygen flux computed by BON2014 and corrected model to AMS-02 measurements.

The final step in the calibration process is to correct δ. To accomplish this, the optimal ϕ is re-calculated over a range of δ values in the interval [-5, 5], but this time the corrected parameters, $j^{(2)}$ and $\gamma^{(2)}$, obtained from the previous step, are used. The model results are then compared to all available measurements. The following error metrics are considered for this step [Slaba and Blattnig 2014b]

$$\varepsilon_{R_D} = \sum_{i=1}^{5} R_D^{(i)}\ , \tag{18}$$

$$\varepsilon_{R_{|D|}} = \sum_{i=1}^{5} R_{|D|}^{(i)}\ , \tag{19}$$

$$\tilde{\varepsilon}_{R_D} = \left[1 - \sum_{i=1}^{5} \frac{w_i}{1 + R_D^{(i)}}\right] \Bigg/ \sum_{i=1}^{5} \frac{w_i}{1 + R_D^{(i)}}, \tag{20}$$

$$\tilde{\varepsilon}_{R_{|D|}} = \left[1 - \sum_{i=1}^{5} \frac{w_i}{1 + R_{|D|}^{(i)}}\right] \Bigg/ \sum_{i=1}^{5} \frac{w_i}{1 + R_{|D|}^{(i)}}, \tag{21}$$

where w_i are the weights defined over specific energy bins identified in Table 2 of Slaba and Blattnig [2014a], and the error metrics R_D and $R_{|D|}$ have already been defined. Equations (18) and (19) are simply the average relative errors computed over the pre-defined energy bins. Equations (20) and (21) quantify the expected relative error propagated into effective dose equivalent behind 20 g/cm^2 shielding as a result of errors in the GCR model. It was found that consideration of all four error metrics provided an improved global fit compared to the outcomes achieved with just using one of the metrics. The average errors associated with each δ value were sorted by rank, and an average rank was computed by giving equal weight to the four metrics. The δ value giving rise to the best average rank was identified as the optimal solution.

Modified process for Z = 1 – 4

For ions with Z = 1 – 4, there are no ACE/CRIS measurements to find an optimal solar modulation potential. The available measurements for these ions also do not contain sufficient time resolution to directly quantify the solar modulation function. As a result, the oxygen solar modulation function is used for these ions. The remainder of the calibration process outlined in the previous section is then repeated to obtain corrected LIS parameters for these ions. The parameters obtained for all ions are given in the Appendix B.

Validation and Uncertainty Quantification

In this section, the updated model is compared to BON2014 and available measurements. A description of the measurements used for LIS parameter calibration and uncertainty quantification may be found in Appendix C. Appendix D provides plots comparing fluxes from the models to a representative subset of the measurements. Results provided in this section summarize the validation results for specific ions, energies, and time-intervals. Comparisons are made between BON2014 and three variants of the updated model. These variants are defined as

- BON2020$_{\text{ACE}}$ – The solar modulation potential is obtained for each ion between Z = 5 and Z = 28 from daily ACE/CRIS integral flux if available and from V2 SSN outside of the time period covered by ACE/CRIS. The Z = 8 solar modulation function is used for ions between Z = 1 and Z = 4.
- BON2020$_{\text{ACE-O}}$ – Same as BON2020$_{\text{ACE}}$, except that only daily ACE/CRIS integral oxygen flux is used to described solar activity. The linear regression coefficients are used to estimate ACE/CRIS integral fluxes for all other ions.
- BON2020$_{\text{SSN}}$ – Same as BON2020$_{\text{ACE}}$, except that only V2 SSN values are used to obtain the solar modulation potential.

These extra comparisons are being included to demonstrate that the options for describing solar activity within the model are self-consistent and yield similar, if not identical, results in most cases. This consistency is particularly important for historical analyses wherein the model may be driven directly by ϕ, SSN, or ACE/CRIS data.

Table 1 provides the average model errors against all available measurements. The R_D error metric provides a measure for systematic model trends relative to the data. Negative R_D values indicate that a model underestimates measured values, while positive values indicate the opposite. Note from the definition of equation (15) that R_D allows cancellation of positive and negative model errors to occur. The $R_{|D|}$ error metric does not allow cancellation and therefore provides a measure of dispersion between the model and measurement. The χ^2 metric also provides a measure of dispersion between model and measurement, but because the differences are squared, extreme errors are amplified in the summary value.

It can be seen in Table 1 that all variants of BON2020 are markedly better than BON2014. The systematic under prediction associated with BON2014 has been corrected, and the overall dispersion has been reduced by more than a factor of two. One can also see that the average errors associated with BON2020$_{\text{ACE}}$ and BON2020$_{\text{ACE-O}}$ are

nearly identical, suggesting that driving the model with all ACE/CRIS ion data or just ACE/CRIS oxygen data yields similar results.

Table 1. Average model errors against all available measurements. The χ^2 values have been multiplied by 10^4 to clarify comparisons between the models.

Model	R_D (%)	$R_{\|D\|}$ (%)	$\chi^2 \times 10^4$
BON2014	-4.6	12.0	42.4
$BON2020_{ACE}$	-0.3	5.2	8.6
$BON2020_{ACE\text{-}O}$	-0.4	5.3	8.6
$BON2020_{SSN}$	0.6	8.8	33.0

Further information is gained by examining Figure 6, which shows the distribution of model errors giving rise to the average values shown in Table 1. The distributions in the Figure for the BON2020 variants are centered near 0% and appear to be symmetric, suggesting no systematic bias in the models. The BON2014 distribution is shifted towards negative values and is also noticeably broader than any of the BON2020 variants. The width of the distributions is related to the level of dispersion between model and measurements. For the BON2014 model, the fraction of R_D values that fell between $\pm$15% was 0.73, while for $BON2020_{ACE}$, $BON2020_{ACE\text{-}O}$, and $BON2020_{SSN}$ these fractions were increased to 0.95, 0.95, and 0.83, respectively. Phrased differently, the 95% confidence level (CL) of the $BON2020_{ACE}$ and $BON2020_{ACE\text{-}O}$ relative errors is $\pm$15%.

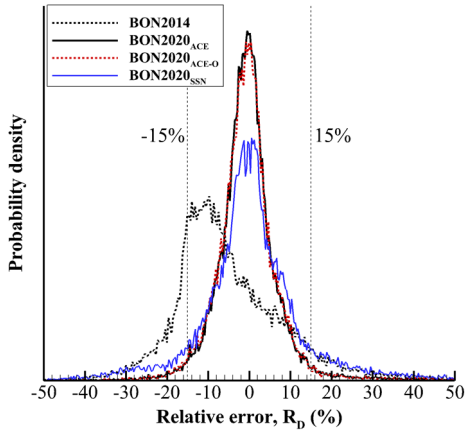

Figure 6. Distribution of model errors against all available measurements.

Specific ions and energy groups account for large fractions of the exposure received behind shielding in space. It is therefore instructive to consider model errors in this way. Figure 7 shows the average model relative differences (R_D) separated into energy groups shown along the horizontal axes and charge groups indicated by different colored symbols. The error bars in the plot reflect the interval associated with measurement uncertainty. The figure shows negative relative errors for BON2014 for $Z = 1$ and $Z = 2$ in the three highest energy bins which have been shown to be significant for space radiation protection applications. The BON2020 variants all show minimal error for these same ions and energy groups.

Figures 8 – 10 provide more detailed information regarding the time-dependent behavior of the model for protons and helium. Figure 9 is of particular interest since the Cosmic Ray Telescope for the Effects of Radiation (CRaTER) data [Zeitlin et al. 2019] were not used in the calibration process and therefore provide an opportunity for independent validation.

The $BON2020_{ACE}$ and $BON2020_{ACE\text{-}O}$ results in these figures are identical since the proton and helium solar modulation functions in both versions of the model are obtained from the oxygen solar modulation function (i.e. ACE/CRIS oxygen data). It can be seen that these models track very well with the measurements, suggesting that the short term heliospheric perturbations reflected in ACE/CRIS oxygen data are a suitable proxy for protons and helium. The $BON2020_{SSN}$ model lacks the same level of detail since it is driven by SSN, but it still shows an overall improvement compared to the BON2014 results as the systematic underestimation of the proton flux in solar cycle 23 (Figures 8 left and 10) and helium flux (Figure 8 right) by BON2014 have been corrected.

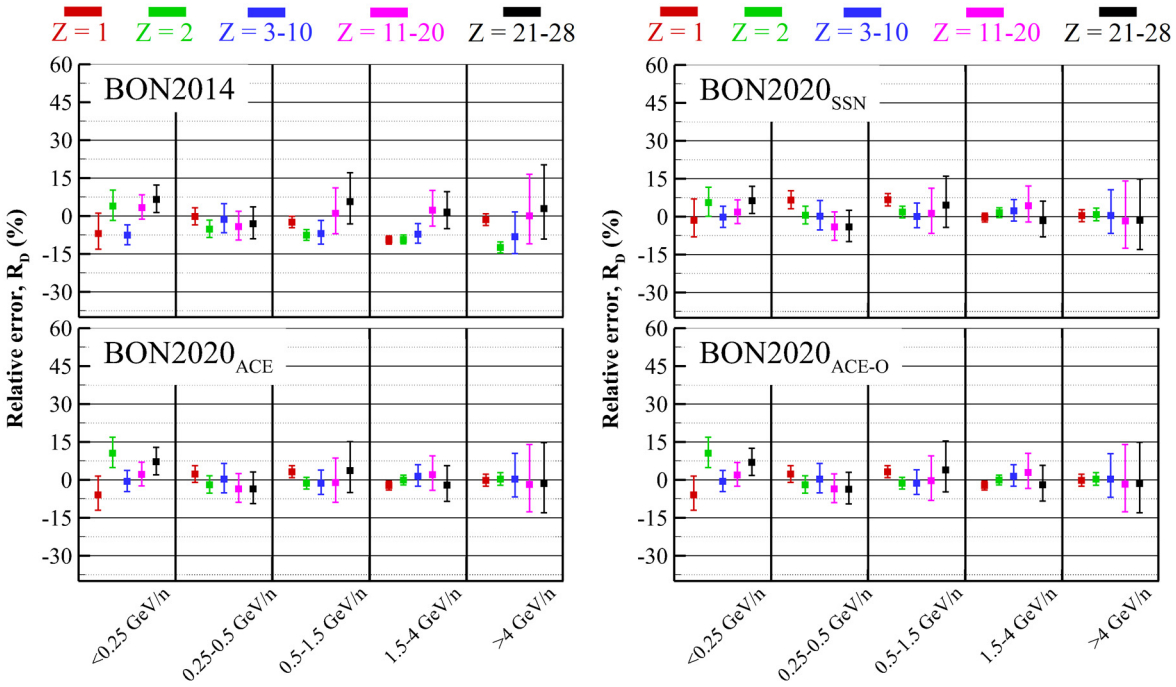

Figure 7. Average model relative error separated into energy groups indicated on the horizontal axes and charge groups indicated with different colored symbols. The error bars are closely related to measurement uncertainty.

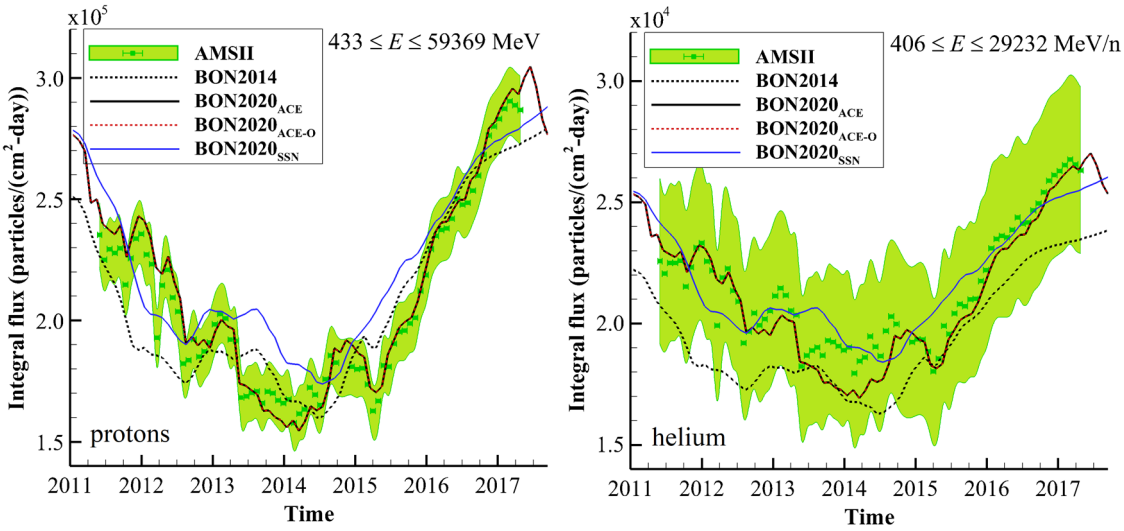

Figure 8. Model integral flux compared to AMS-02 measurements. The shaded region represents total measurement uncertainty.

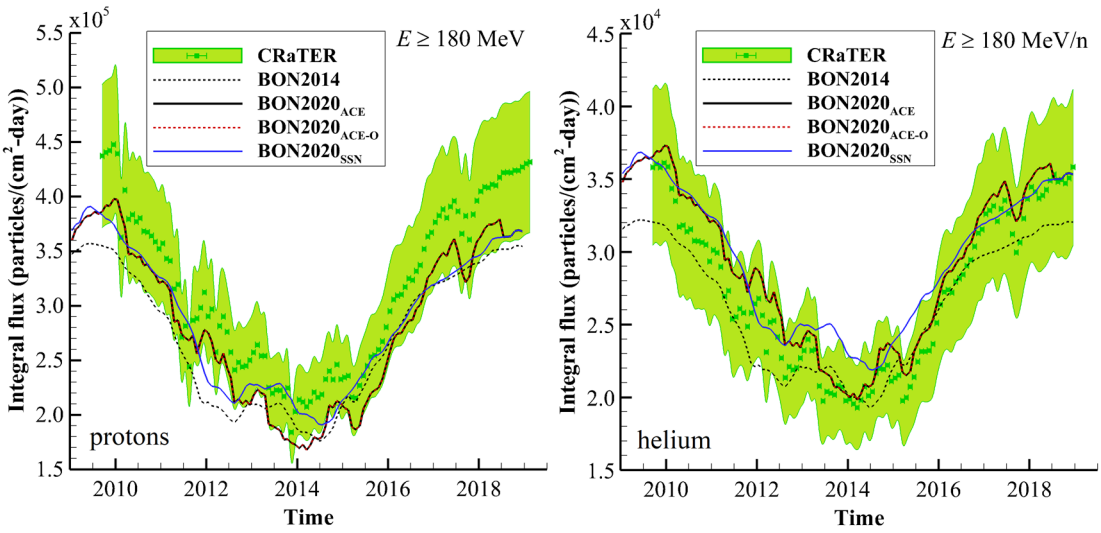

Figure 9. Model integral flux compared to CRaTER measurements. The shaded region represents total measurement uncertainty.

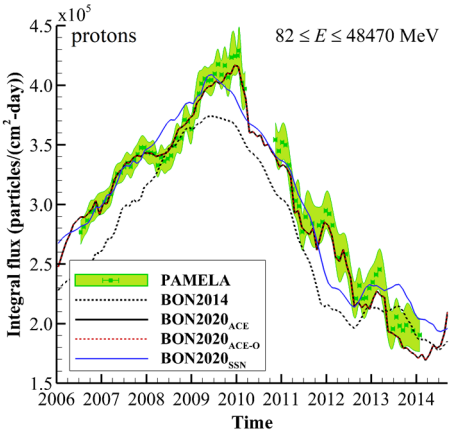

Figure 10. Model integral flux compared to PAMELA measurements. The shaded region represents total measurement uncertainty.

A quantitative assessment of the results shown in these figures is given in Table 2. The r^2 values for $BON2020_{ACE}$ and $BON2020_{ACE\text{-}O}$ are identical, as expected, and are all greater than 0.92, indicating a high degree of correlation between model results and measurement data. The $R_{|D|}$ values are also given in the table to highlight that not only is the updated model more closely correlated with time-dependent measurement data, but also provides flux values that are closer in overall magnitude to measurement data than BON2014.

Table 2. r^2 values obtained by comparing models to time-series integral flux data from various detectors. The corresponding $R_{|D|}$ values are given in parentheses.

Model	AMS-02		CRaTER		PAMELA
	protons	helium	protons	helium	protons
BON2014	0.79 (7%)	0.78 (10%)	0.91 (14%)	0.91 (6%)	0.89 (10%)
$BON2020_{ACE}$	0.98 (3%)	0.93 (3%)	0.97 (12%)	0.98 (6%)	0.99 (3%)
$BON2020_{ACE\text{-}O}$	0.98 (3%)	0.93 (3%)	0.97 (12%)	0.98 (6%)	0.99 (3%)
$BON2020_{SSN}$	0.82 (8%)	0.79 (4%)	0.92 (10%)	0.92 (8%)	0.98 (5%)

Figure 11 shows the average model relative differences compared to ACE/CRIS data for Z = 5 - 28 as a function of time. It can be seen that again $BON2020_{ACE}$ and $BON2020_{ACE\text{-}O}$ yield almost identical results. This is a significant result since it establishes that the linear regression coefficients used to relate integral ACE/CRIS oxygen flux to all other ions are a suitable proxy for describing solar activity for all ions between $Z = 5$ and $Z = 28$. Also evident in the plot is that the method outlined in the previous section used to generate an optimal ϕ allows the model to accurately reproduce the low energy ACE/CRIS data throughout the solar cycle. $BON2020_{SSN}$ lacks the same level of fidelity, but is still an improvement over BON2014, especially near the 2000 solar maximum.

Finally, in Figure 12 the LIS from BON2014 and BON2020 (all variants of BON2020 use the same LIS) are compared to the models of Corti et al. [2016] and HELMOD [Boschini et al. 2018]. These additional models were developed specifically to represent the shape and magnitude of the LIS and utilize over 10 free parameters each to represent available data. The BON LIS, on the other hand, is a consequence of only three parameters that are calibrated only by near Earth measurements. The comparison in Figure 12 therefore provides an indirect test of the physics included in BON describing solar modulation and heliospheric transport and also provides independent verification for the specified LIS parameters.

When compared to HELMOD or Corti et al., the overall BON2020 LIS spectral shapes show a significant improvement compared to BON2014. The BON2020 proton LIS shows a more realistic rise, rollover, and high energy spectral slope. The BON2020 helium LIS corrects the systematic underestimate at high energies that was present in BON2014 and is in excellent agreement with the other models across all energies up to 2×10^5 MeV/n. Discrepancies at larger energies are of little consequence to space radiation protection applications since the flux of particles at these energies is exceedingly small.

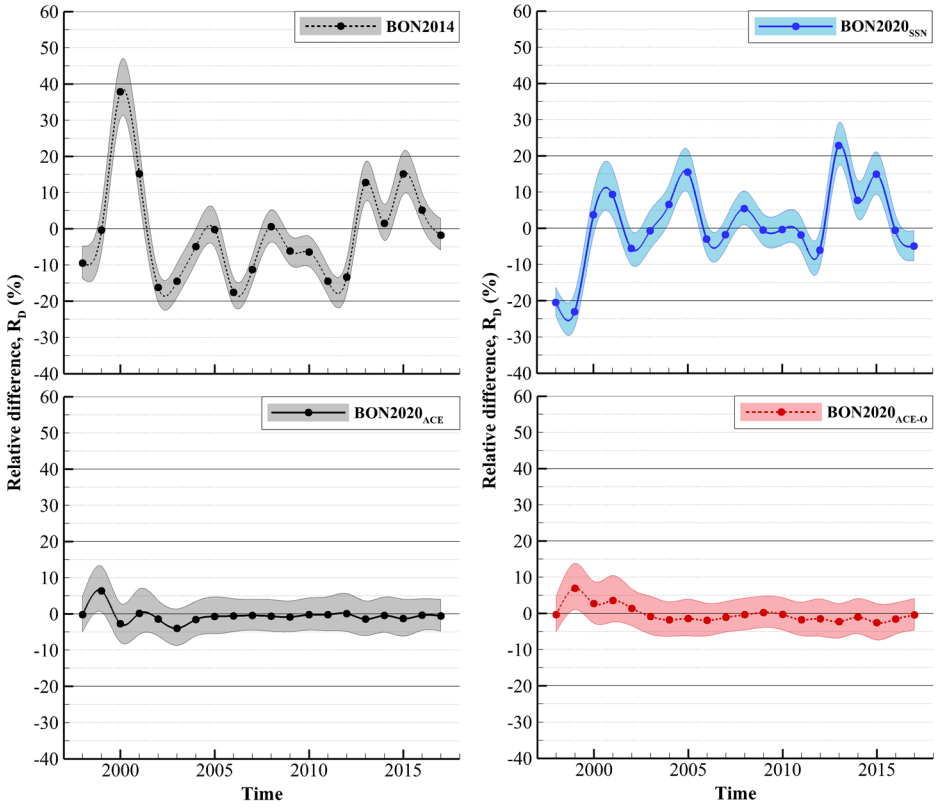

Figure 11. Average model relative differences compared to ACE/CRIS data for Z = 5 - 28 as a function of time. The shaded regions are closely related to measurement uncertainty.

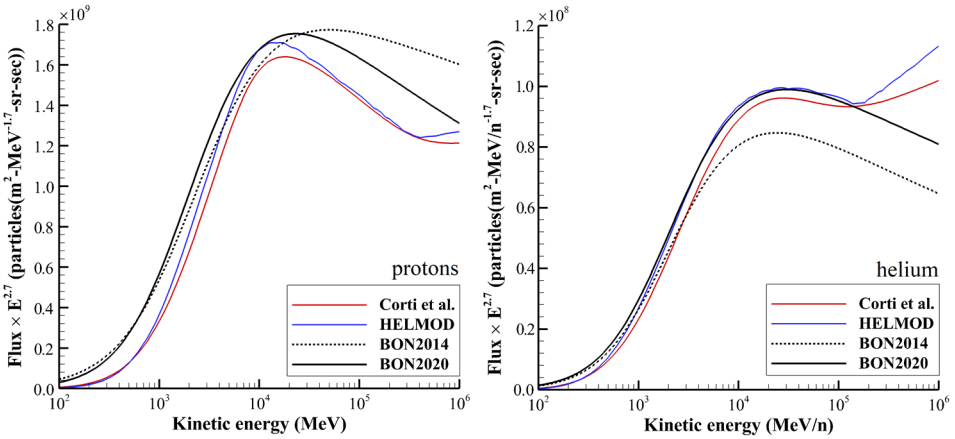

Figure 12. Comparison of LIS from BON2014, BON2020 and other parametric models for protons and helium.

Propagated Errors

Model uncertainties described in the previous section may be propagated into effective dose behind shielding [Slaba and Blattnig 2014b], as shown in Figure 13. Results in the figure are for the June 1, 2009 - June 1, 2010 solar minimum. The methods used to compute effective dose are described elsewhere [Slaba et al. 2010a,b; Slaba et al. 2013].

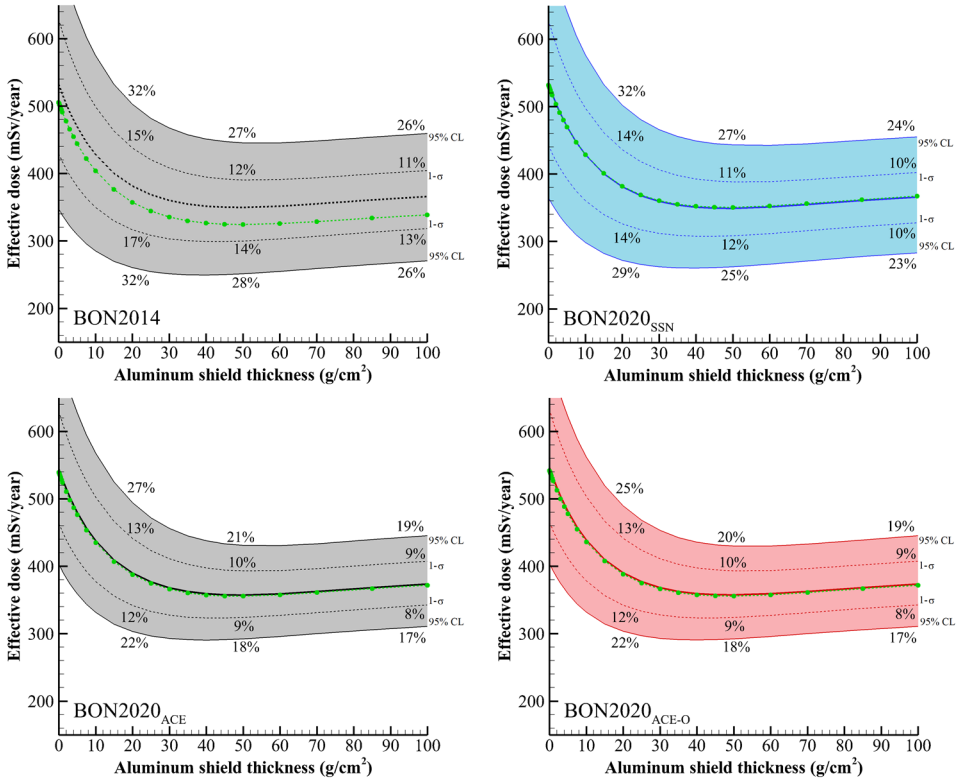

Figure 13. Female effective dose versus shield thickness for the June 1, 2009 – June 1, 2010 solar minimum. The green dashed line with circles is the nominal model result, while the shaded region indicates the distribution of effective doses resulting from uncertainty in the GCR model. Specific intervals of the distributions and relative differences at specific depths are shown.

The green dashed line with symbols in each figure corresponds to the nominal model result. These are the values one would obtain if the mission dates were input into the GCR model to provide a boundary condition for the remainder of the analysis tools. The shaded region corresponds to the distribution of effective dose values attributable to the uncertainties outlined in the previous section. The standard deviation interval (1-σ) and 95% CL of the distributions are explicitly shown. For each model, the line appearing closest to the nominal result is the median of the distribution. Percent differences between the 1-σ and 95% CL value relative to the median are explicitly shown at depths of 20, 50, and 100 g/cm^2.

In the case of the BON2020 variants, the nominal and median model results are nearly identical. This is consistent with the results of Figure 6 where it was shown that these models have negligible systematic bias. For BON2014, it is seen that the nominal model result is below the median, suggesting that the nominal model result is under-estimating what would be expected from measurements (also consistent with Figure 6). The BON2020$_{ACE}$ and BON2020$_{ACE\text{-}O}$ error intervals are all smaller than those found for BON2014. Moderate reductions in uncertainty compared to BON2014 are also found for BON2020$_{SSN}$. As in all other results shown thus far, the BON2020$_{ACE}$ and BON2020$_{ACE\text{-}O}$ are almost indistinguishable and were found to be within 0.5% of each other across all depths.

A final comparison of the models is given in Figure 14 which shows effective dose as a function of time for 20 g/cm^2 aluminum shielding. The BON2020$_{ACE}$ and BON2020$_{ACE\text{-}O}$ results were within 3% of each other across all mission times. Prior to ~1998, all of the BON2020 variants revert back to SSN to obtain ϕ and therefore yield identical results. After 1998, the BON2020$_{SSN}$ values appear consistent with BON2020$_{ACE}$ and BON2020$_{ACE\text{-}O}$. The average $R_{|D|}$ between BON2020$_{ACE}$ and BON2020$_{SSN}$ over all mission times was found to be 2%; although, R_D values as high as $\pm$24% were found. The results from BON2014 appear consistently lower than the others.

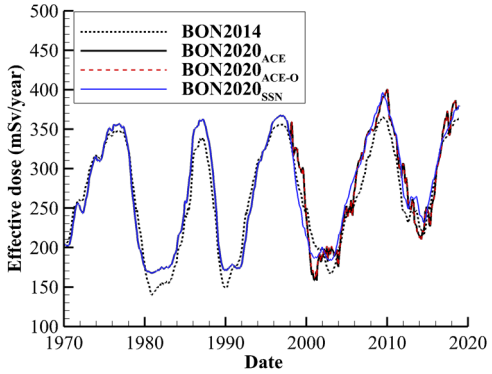

Figure 14. Female effective dose versus time behind 20 g/cm^2 aluminum shielding using different GCR models.

Summary

The BON2020 model has been fully described and its improved performance demonstrated. The updated model has been calibrated to available measurement data, including the high precision measurements from AMS-02 and PAMELA. Solar activity is quantified through a simple parametric function relating daily ACE/CRIS integral flux to the solar modulation potential for each ion. For time periods outside of the region covered by ACE/CRIS, the model utilizes empirical relationships to relate time-delayed SSN values to ACE/CRIS integral oxygen flux. The estimated oxygen flux is combined with linear regression coefficients to estimate integral fluxes for all other ions between Z = 5 and Z = 28. These estimated fluxes are then used to compute the solar modulation potential for each ion. In all cases, the oxygen solar modulation potential is used for Z = 1 – 4 ions.

Three variants of the BON2020 model were identified:

- BON2020$_{ACE}$ – The solar modulation potential is obtained for each ion between Z = 5 and Z = 28 from daily ACE/CRIS integral flux if available and from V2 SSN elsewhere. The Z = 8 solar modulation function is used for ions between Z = 1 and Z = 4.
- BON2020$_{ACE\text{-}O}$ – Same as BON2020$_{ACE}$, except that only daily ACE/CRIS integral oxygen flux is used to described solar activity. The linear regression coefficients are used to estimate ACE/CRIS integral fluxes for all other ions.

- $BON2020_{SSN}$ – Same as $BON2020_{ACE}$, except that only V2 SSN values are used to obtain the solar modulation potential.

Along with BON2014, the BON2020 variants were compared to available measurements and uncertainty was quantified. It was found that the BON2020 is a significant improvement over BON2014. The systematic tendency of BON2014 to under-estimate measurements was corrected. The dispersion between model and measurement, expressed through the $R_{|D|}$ and χ^2 metrics, was reduced by more than a factor of two. Comparison of the models against time-resolved AMS-02, PAMELA, CRaTER, and ACE/CRIS data showed that the BON2020 is able to accurately describe short and long-term solar activity effects.

It is suggested that the $BON2020_{ACE\text{-}O}$ variant be used for space radiation protection applications. It was clearly shown that the $BON2020_{ACE}$ and $BON2020_{ACE\text{-}O}$ models yield similar, if not identical, results in terms of uncertainty quantification and radiation protection quantities such as effective dose. The $BON2020_{ACE\text{-}O}$ is driven by a simpler dataset (daily ACE/CRIS integral oxygen flux) and also maintains perfect consistency in results whether mission dates or the solar modulation parameter is specified.

Acknowledgements

The authors gratefully acknowledge and thank Pat O'Neill for his thoughtful review of the model and manuscript. This work was supported by the Advanced Exploration Systems (AES) under the Human Exploration and Operations Mission Directorate of NASA and NASA contract NNJ15HK11B.

References

Abe, K., et al., Measurements of cosmic-ray proton and helium spectra from the BESS-polar long-duration balloon flights over Antarctica. *Astrophys. J.* **822**: 1-16; 2016.

Adriani, O., et al., PAMELA measurements of cosmic-ray proton and helium spectra. *Science* **332**: 69-72; 2011.

Adriani, O., et al., Time dependence of the proton flux measured by PAMELA during the 2006 July – 2009 December solar minimum. *Astrophys. J.* **765**: 1-8; 2013.

Adriani, O., et al., Ten years of PAMELA in space. *Rivista del Nuovo Cimento* **40**: 473-522; 2017.

Aguilar, M., et al., Precision measurement of the helium flux in primary cosmic rays of rigidities 1.9 GV to 3 TV with the Alpha Magnetic Spectrometer on the International Space Station. *Phys. Rev. Lett.* **115**: 211101; 2015a.

Aguilar, M., et al., Precision measurement of the proton flux in primary cosmic rays from rigidity 1 GV to 1.8 TV with the Alpha Magnetic Spectrometer on the International Space Station. *Phys. Rev. Lett.* **114**: 171103; 2015b.

Aguilar, M., et al., Observation of the identical rigidity dependence of He, C, and O cosmic rays at high rigidities by the Alpha Magnetic Spectrometer on the International Space Station. *Phys. Rev. Lett.* **119**: 251101; 2017.

Aguilar, M., et al., Observation of new properties of secondary cosmic rays lithium, beryllium, and boron by the Alpha Magnetic Spectrometer on the International Space Station. *Phys. Rev. Lett.* **120**: 021101; 2018a.

Aguilar, M. et al., Precision measurement of cosmic-ray nitrogen and its primary and secondary components with the Alpha Magnetic Spectrometer on the International Space Station. *Phys. Rev. Lett.* **121**: 051103; 2018b.

Aguilar, M., et al., Observation of fine time structures in the cosmic proton and helium fluxes with the alpha Magnetic Spectrometer on the International Space Station. *Phys. Rev. Lett*., **121**:, 051101; 2018c.

Ahn, H.S., et al., Energy spectra of cosmic-ray nuclei at high energies. *Astrophys. J.* **707**: 593-603; 2009.

Alcaraz, J., et al., Cosmic protons. *Phys. Lett. B* **490**: 27-35; 2000a.

Alcaraz, J., et al., Helium in near earth orbit. *Phys. Lett. B* **494**: 193-202; 2000b.

Ave, M., Boyle, P.J., Gahbauer, F., Hoppner, C., Horandel, J.R., Ichimura, M., Muller, D., Romero-Wolf, A., Composition of primary cosmic-ray nuclei at high energies. *Astrophys. J.* **678**: 262-273; 2008.

Bellotti, R., et al., Balloon measurements of cosmic ray muon spectra in the atmosphere along with those of primary protons and helium nuclei over midlatitude. *Phys. Rev. D* **60**: 052002-1; 1999.

Boezio, M., et al., The cosmic-ray proton and helium spectra between 0.4 and 200 GV. *Astrophys. J.* **518**: 457-472; 1999.

Boezio, M., et al., The cosmic-ray proton and helium spectra measured with the CAPRICE98 balloon experiment. *Astroparticle Phys.* **19**: 583-604; 2003.

Boschini, M.J., Della Torre, S., Gervasi, M., La Vacca, G., Rancoita, P.G., Propagation of cosmic rays in the heliosphere: the HELMOD model. *Adv. Space Res.* **62**: 2859-2879; 2018.

Clette, F., Cliver, E.W., Lefèvre, L, Svalgaard, L., Vaquero, J.M., Leibacher, J.W., 2016: Preface to topical issue: recalibration of the sunspot number, *Solar Phys.* **291**: 2479-2486; 2016.

Corti, C., Bindi, V., Consolandi, C., Whitman, K., Solar modulation of the local interstellar spectrum with Voyager 1, AMS-02, PAMELA, and BESS. *Astrophys. J.* **829**: 1-9; 2016.

Corti, C., Potgieter, M.S., Bindi, V., Consolandi, C., Light, C., Palermo, M., Popkow, A., Numerical modeling of galactic cosmic-ray proton and helium observed by AMS-02 during the solar maximum of solar cycle 24. *Astrophys. J.* **871**: 253-268; 2019.

Engelmann, J.J., Ferrando, P., Soutoul, A., Goret, P., Juliusson, E., Koch-Miramond, L., Lund, N., Masse, P., Peters, B., Petrou, N., Rasmussen, I.L., Charge composition and energy spectra of cosmic-ray nuclei for elements from Be to Ni. Results from HEAO-3-C2. *Astron. Astrophys.* **233**: 96-111; 1990.

Fisk, L. A., Solar modulation of galactic cosmic rays, 2. NASA Technical Memorandum X-63932; 1970

Garcia-Munoz, M., Mason, G.M., Simpson, J.A., Wefel, J.P., Charge and energy spectra of heavy cosmic rays at intermediate energies. 15th International Cosmic Ray Conference, Plovdiv, Bulgaria; 1977.

Gleeson, L.J, Urch, I.H., Energy losses and modulation of galactic cosmic rays. *Astrophys. Space Sci.* **11**: 288-308; 1971.

Lezniak, J.A., Webber, W.R., The charge composition and energy spectra of cosmic-ray nuclei from 3000 MeV per nucleon to 50 GeV per nucleon. *Astrophys. J.* **233**: 676-696; 1978.

Lockwood, J.A., Webber, W.R., Debrunner, H., Differences in the maximum intensities and the intensity-time profiles of cosmic rays in alternate solar magnetic field polarities. *J. Geo. Res.* **106**: 10,653-10,644; 2001.

Martucci, M., et al., Proton fluxes measured by the PAMELA experiment from the minimum to the maximum solar activity for solar cycle 24. *Astrophys. J. Lett.* **854**; 2018.

Matthia, D., Berger, T., Mrigakshi, A.I., Reitz, G., A ready-to-use galactic cosmic ray model. *Adv. Space Res.* **51**: 329-338; 2013.

Menn, W., et al., The absolute flux of protons and helium at the top of the atmosphere using IMAX. *Astrophys. J.* **533**: 281-297; 2000.

Mertens, C.J., Meier, M.M., Brown, S., Norman, R.B., Xu, X., NAIRAS aircraft radiation model development, dose climatology, and initial validation. *Space Weather* **11**: 603-605; 2013.

Minagawa, G., The abundances and energy spectra of cosmic ray iron and nickel at energy from 1 to 10 GeV per amu. *Astrophys. J.* **248**: 847-855; 1981.

Norbury, J.W., Whitman, K., Lee, K., Slaba, T.C., Badavi, F.F., Comparison of space radiation GCR models to recent AMS data. *Life Sci. Space Res.* **18**: 64-71; 2018.

Nymmik, R.A., Time lag of galactic cosmic ray modulation: conformity to general regularities and influence on particle energy spectra. *Adv. Space Res.* **26**: 1875-2000; 2000.

O'Neill, P.M., Badhwar-O'Neill galactic cosmic ray model updated based on advanced composition explorer (ACE) energy spectra from 1997 to present. *Adv. Space Res.* **37**: 1727-1733; 2006.

O'Neill, P.M., Badhwar-O'Neill galactic cosmic ray flux model – revised. *IEEE Trans. Nucl. Sci.* **57**: 3148 – 3153; 2010.

O'Neill, P.M., Golge, S., Slaba, T.C., Badhwar-O'Neill 2014 galactic cosmic ray flux model description. NASA Technical Paper 2015-218569; 2015.

Panov, A.D., et al., Energy spectra of abundant nuclei of primary cosmic rays from the data of ATIC-2 experiment: final results. *Russ. Acad. Sci. Phys.* **73**: 564-567; 2009.

Parker, E. N., The passage of energetic charged particles through interplanetary space. *Plan. Space Sci.* **13**: 9; 1965.

Potgieter, M. S., The charge-sign dependent effect in the solar modulation of cosmic rays. *Adv. Space Res*. **53**: 1415-1425; 2014.

Shikaze, Y., et al., Measurements of 0.2-20 GeV/n cosmic-ray proton and helium spectra from 1997-2002 with the BESS spectrometer. *Astroparticle Phys.* **28**: 154-167; 2008.

Simon, M., Ormes, J.F., Balasubrahmanyan, V.K., Arens, J.F., Energy spectra of cosmic-ray nuclei to above 100 GeV per nucleon. *Astrophys. J.* **239**: 712-724; 1980.

Slaba, T.C., Qualls, G.D., Clowdsley, M.S., Blattnig, S.R., Walker, S.A., Simonsen, L.C., Utilization of CAM, CAF, MAX, and FAX for space radiation analyses using HZETRN. *Adv. Space Res.* **45**: 866-883; 2010a.

Slaba, T.C., Blattnig, S.R., Badavi, F.F., Faster and more accurate transport procedures for HZETRN. *J. Comp. Phys.* **229**: 9397-9417; 2010b.

Slaba, T.C., Blattnig, S.R., Reddell, B., Bahadori, A., Norman, R.B., Badavi, F.F., Pion and electromagnetic contribution to dose: comparisons of HZETRN to Monte Carlo results and ISS data. *Adv. Space Res.* **52**: 62-78; 2013.

Slaba, T.C., Blattnig, S.R., GCR environmental models I: sensitivity analysis for GCR environments. *Space Weather* **12**: 217-224; 2014a.

Slaba, T.C., Blattnig, S.R., GCR environmental models II: uncertainty propagation methods for GCR environments. *Space Weather* **12**: 225-232; 2014b.

Slaba, T.C., Xu, X., Blattnig, S.R., Norman, R.B., GCR environmental models III: GCR model validation and propagated uncertainties in effective dose. *Space Weather* **12**: 233-245; 2014.

Stone, E.C., Frandsen, A.M., Mewaldt, R.A., Christian, E.R., Margolies, D., Ormes, J.F., Snow, F., The advanced composition explorer, *Space Sci. Rev.* **86**: 1-22; 1998.

Whitman, K., Norbury, J.W., Lee, K., Slaba, T.C., Badavi, F.F., Comparison of space radiation GCR models to AMS heavy ion data. *Life Sci. Space Res.* **22**: 76-88; 2019.

Zeitlin, C., Schwadron, N.A., Spence, H.E., Jordan, A.P., Looper, M.D., Wilson, J., Mazur, J.E., Townsend, L.W., Update on galactic cosmic ray integral flux measurements in lunar orbit with CRaTER. *Space Weather* **17**: 1011-1017; 2019.

Appendix A

The linear relationship between ACE/CRIS integral oxygen flux (F_8) and ACE/CRIS integral flux for any other ion between Z = 5 and Z = 28 (F_Z) is written as

$$F_Z = \alpha F_8 + \beta \,. \tag{22}$$

Table A1 gives the linear regression coefficients found from the daily ACE/CRIS integral flux data. Equation (22) and the regression coefficients are used to estimate ACE/CRIS integral flux for ions inside the updated BON model.

Table A1. Linear regression coefficients relating ACE/CRIS integral oxygen flux to all other ions between Z = 5 and Z = 28.

Z	α	β	Z	α	β
5	0.14485829	1.51582500	17	0.00503104	0.24662716
6	0.81573219	-0.72465207	18	0.01271422	0.45690837
7	0.20036156	1.57610755	19	0.00952531	0.40500960
8	1.00000000	0.00000000	20	0.03007700	0.87703765
9	0.01377807	0.25171284	21	0.00626074	0.21763124
10	0.15261210	1.43415417	22	0.02455841	0.69740806
11	0.03035187	0.45963452	23	0.01215822	0.32291215
12	0.24310154	2.09412215	24	0.02462712	0.64977124
13	0.03701433	0.54833313	25	0.01574368	0.41069961
14	0.19620901	2.14312987	26	0.17033059	4.42746263
15	0.00500258	0.17342666	27	0.00098556	0.02982341
16	0.03259685	0.73208661	28	0.00849537	0.26150686

Appendix B

The LIS serves as the boundary condition for the BON model and is given by the parametric form defined in equation (1). This functional form requires three parameters (j_0, γ, δ) to be specified for each ion. Two additional parameters (a, b) are needed for equation (12) to determine the optimal solar modulation potential for each ion. The LIS and solar modulation potential parameters are given in Tables B1 and B2, respectively.

Table B1. LIS parameters (j_0, γ, δ) for each ion.

Z	j_0	γ	δ	Z	j_0	γ	δ
1	9.35958×10^{-4}	2.80583	2.12	15	7.00114×10^{-9}	3.07083	1.76
2	5.31867×10^{-5}	2.78079	-2.04	16	5.86173×10^{-8}	2.70070	-1.74
3	1.60292×10^{-7}	3.11530	1.86	17	6.09709×10^{-9}	3.10022	0.78
4	9.40500×10^{-8}	3.04829	1.95	18	1.32512×10^{-8}	3.00133	2.75
5	2.19596×10^{-7}	3.05504	0.78	19	8.60410×10^{-9}	3.06630	0.29
6	1.65248×10^{-6}	2.72725	-1.40	20	3.14380×10^{-8}	2.73290	-1.88
7	3.15343×10^{-7}	2.89393	-1.66	21	4.02263×10^{-9}	3.05437	-1.18
8	1.78878×10^{-6}	2.69771	-1.95	22	1.26982×10^{-8}	3.03093	-1.10
9	1.89162×10^{-8}	3.02882	0.26	23	6.53956×10^{-9}	3.01542	-1.39
10	2.47948×10^{-7}	2.73606	-1.25	24	1.69119×10^{-8}	2.91752	-1.21
11	4.00947×10^{-8}	2.78163	-1.95	25	1.39910×10^{-8}	2.79527	-0.88
12	2.86573×10^{-7}	2.74120	-1.57	26	1.91393×10^{-7}	2.61473	-2.68
13	4.88895×10^{-8}	2.79137	-1.20	27	9.70709×10^{-10}	2.65139	-2.98
14	2.71499×10^{-7}	2.65875	-1.80	28	1.18883×10^{-8}	2.53385	-3.71

Table B2. Solar modulation potential function parameters for ions between $Z = 5$ and $Z = 28$.

Z	a	b	Z	a	b
5	8.16584721	42.52927240	17	8.85946321	23.22430086
6	6.48550337	50.47748170	18	14.97644279	23.06985704
7	6.35227073	44.09970682	19	8.74898604	26.98599661
8	6.49624149	53.17273558	20	7.72335159	32.98591723
9	7.94905387	27.49440443	21	8.04037226	24.53215444
10	7.15427126	42.43194677	22	8.34244357	33.72147645
11	6.90386498	32.66672192	23	8.26268864	28.79332093
12	7.22429559	45.64661974	24	8.50720999	33.90214558
13	7.57400616	34.34321589	25	9.13590019	28.84594897
14	7.33607493	44.87787677	26	8.03410596	48.52332652
15	9.73252962	19.74107511	27	7.92714856	8.22280925
16	7.46683928	35.34635734	28	7.61917328	26.28921545

Appendix C

Table C1 provides a summary of the measurements considered in this work. The remainder of this appendix provides spectral comparisons of a selected subset of the measurement data. The particle flux unit (pfu) is defined in the plots as particles/(cm^2-MeV/n-day). Scaled fluxes shown in Figures C1 – C7 are obtained by multiplying the flux by $E^{2.7}$, where E is the kinetic energy of the particle (MeV/n). The scaled particle flux unit (spfu) is defined as particles/(cm^2-MeV/n$^{1.7}$-day).

Table C1. Summary of collected measurements.

Name	Flight	Time	Ions (Z)	Energy (GeV/n)	Data points	Median Error
ACE/CRIS[1]	Satellite	1998-present	5-28	0.05 – 0.5	12446	9%
AMS[2]	STS-91	1998	1, 2	0.1 – 200	58	11%
AMS-02[3]	ISS	2011-2017	1-9	0.4-10^3	7170	3%
ATIC-2[4]	Balloon	2002	1, 2, 6, 8, 10,…,14, 26	4.6 – 10^3	61	33%
BESS[5]	Balloon	1997-2000, 2002, 2004, 2007	1, 2	0.2 – 22	479	11%
CAPRICE[6]	Balloon	1994, 1998	1, 2	0.15 – 350	93	6%
CREAM-II[7]	Balloon	2005	6-8, 10, 12, 14, 26	18 – 10^3	42	25%
HEAO-3[8]	Satellite	1979	4-28	0.62 – 35	332	9%
IMAX[9]	Balloon	1992	1, 2	0.18 – 208	56	18%
MASS[10]	Balloon	1991	1, 2	1.6 – 100	41	9%
PAMELA[11]	Satellite	2006-2009	1, 2	0.08 – 10^3	6614	5%
TRACER[12]	Balloon	2003	8, 10, 12,…,20, 26	0.8 – 10^3	60	10%
Garcia-Munoz[13]	Satellite	1974	6, 8, 10, 12, 14	0.05 – 1	57	27%
Lezniak[14]	Balloon	1974	4-14, 16, 20, 26	0.35 – 52	114	11%
Minagawa[15]	Balloon	1975	26, 28	1.3 – 10	16	8%
Simon[16]	Balloon	1976	5-8	2.5 – 10^3	46	32%

[1][Stone et al. 1998], [2][Alcaraz et al. 2000a, 2000b], [3][Aguilar et al. 2015a,b, 2017, 2018a-c], [4][Panov et al. 2009], [5][Shikaze et al. 2008, Abe et al. 2016], [6][Boezio et al. 1999, Boezio et al. 2003], [7][Ahn et al. 2009], [8][Engelmann et al. 1990], [9][Menn et al. 2000], [10][Bellotti et al. 1999], [11][Adriani et al. 2011, 2013, 2017; Martuicci et al. 2018], [12][Ave et al. 2008], [13][Garcia-Munoz et al. 1977], [14][Lezniak and Webber 1978], [15][Minagawa 1981], [16][Simon et al. 1980]

Visualizing the measurement data demonstrates the significant coverage for some ions in energy and time and extremely sparse coverage for others. In addition, it is clear how the inclusion of new measurements from AMS-02, not available during the calibration of BON2014, have allowed for significant improvement in the overall spectral shapes of hydrogen to oxygen (Z = 1 – 8) in BON2020.

Figure C1 shows the large number of observations for H (left) and He (right). The most recent high-precision AMS-02 fluxes better define the H and He spectral shapes at high energies. Both AMS-02 [Aguilar et al. 2018c] and PAMELA [Martucci et al. 2018] recently published H fluxes on monthly timescales. AMS-02 also published 78 He fluxes on monthly timescales [Aguilar et al. 2018c]. Figure C2 demonstrates the significant improvements that the new AMS-02 measurements integrated over 5 years (May 19, 2011 to May 26, 2016) have provided for Li (left) and Be (right). Prior to AMS-02, these ions were only sparsely measured. Knowledge of Li, in particular, has greatly increased with these recent data. Figures C3 and C4 show measurements for B, C, N, and O. These ions are of particular interest when seeking to understand the physics of GCR, thus they have been measured by multiple experiments. The early data sets used in the calibration of BON2014 had large error bars at high energies compared to the recently published AMS-02 measurements that have been included in the calibration of BON2020.

Some heavy ions of interest, such as Mg, Si, Ca, and Fe shown in Figures C5 and C6 have been observed by multiple experiments across a wide energy range. However, measurements at high energies have large errors bars. Ne has similar coverage to Ca. Many ions, such as F shown in Figure C7 (top left) and P (top right) are measured by only one or two experiments for energies above 500 MeV/n and have extremely limited coverage at high energies. Spectral shapes for these ions are largely unconstrained above 10 GeV/n. Other ions similarly measured by only one or two high-energy experiments include Na, Al, Cl, Ar, K, Sc, Ti, V, Cr, Mn, Co, Ni. Below 500 MeV/n, the ACE/CRIS experiment provides an extremely valuable data set for all ions from B to Ni (Z = 5 - 28). These data were critical in calibrating the LIS for each ion at lower energies and are used to drive the solar modulation in BON2020 for time periods with ACE availability. Figure C7 shows example ACE/CRIS data for F (bottom left) and P (bottom right).

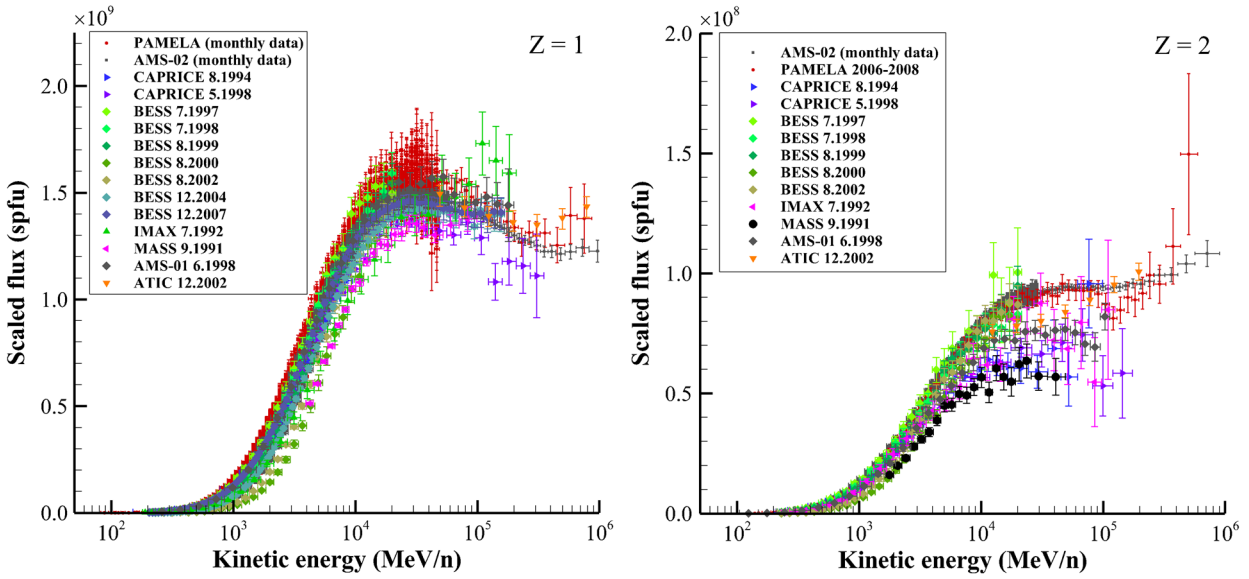

Figure C1. Z = 1 (left) and Z = 2 (right) measurement data.

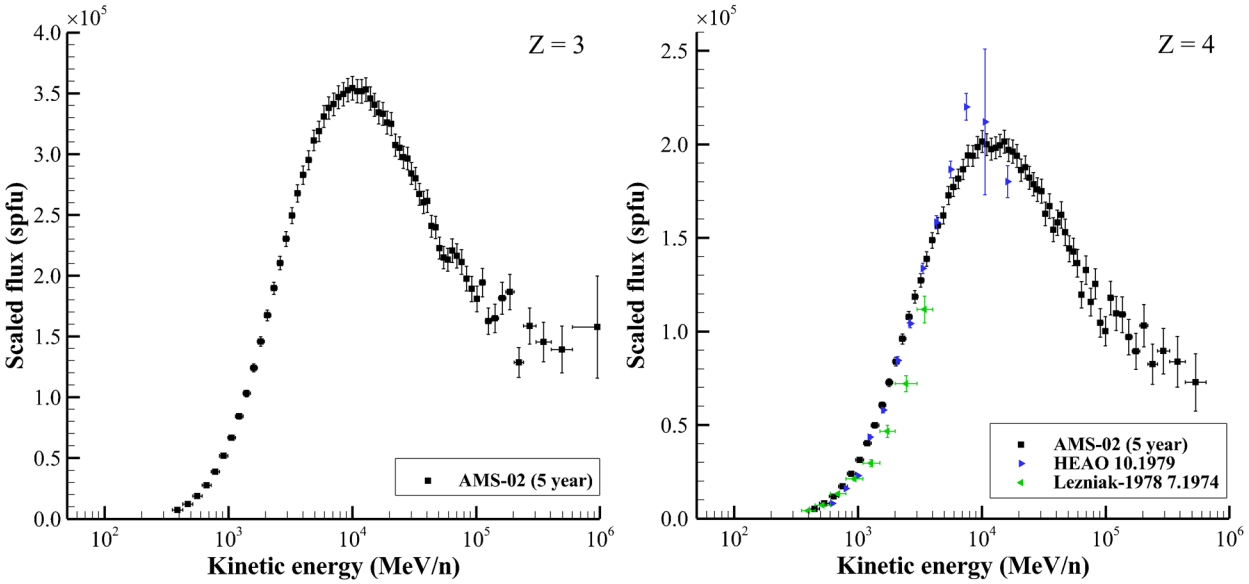

Figure C2. Z = 3 (left) and Z = 4 (right) measurement data.

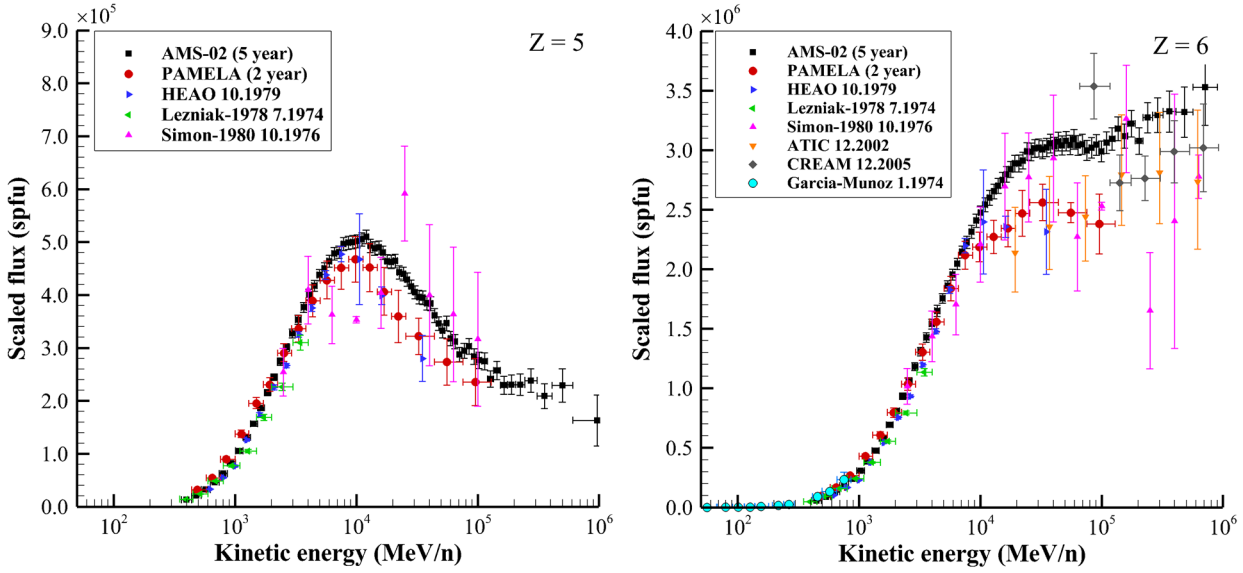

Figure C3. Z = 5 (left) and Z = 6 (right) measurement data.

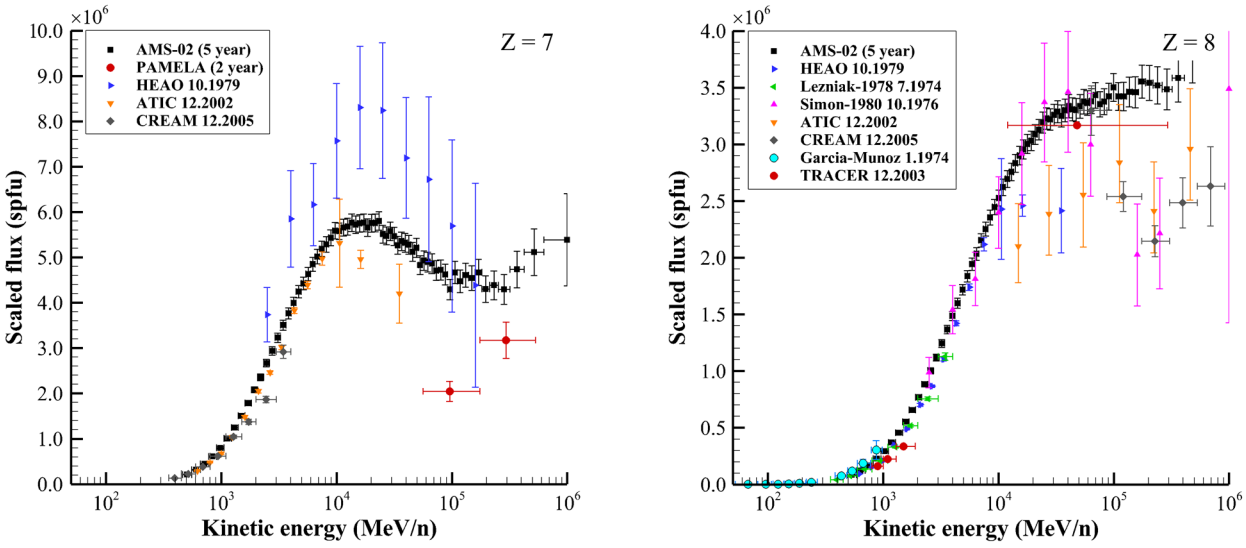

Figure C4. Z = 7 (left) and Z = 8 (right) measurement data.

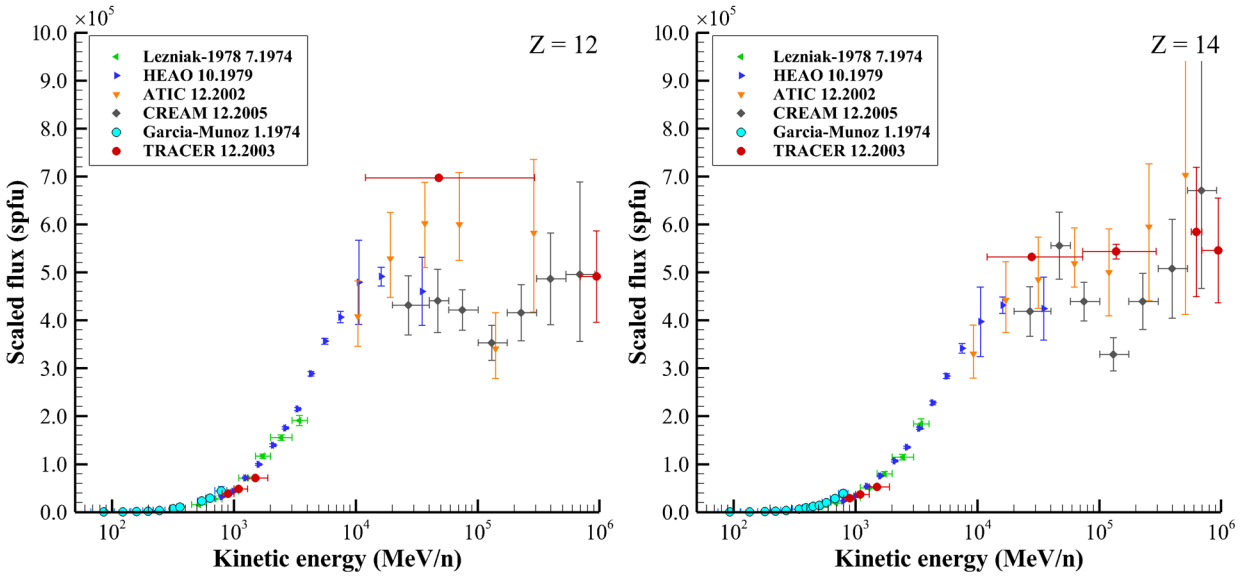

Figure C5. Z = 12 (left) and Z = 14 (right) measurement data.

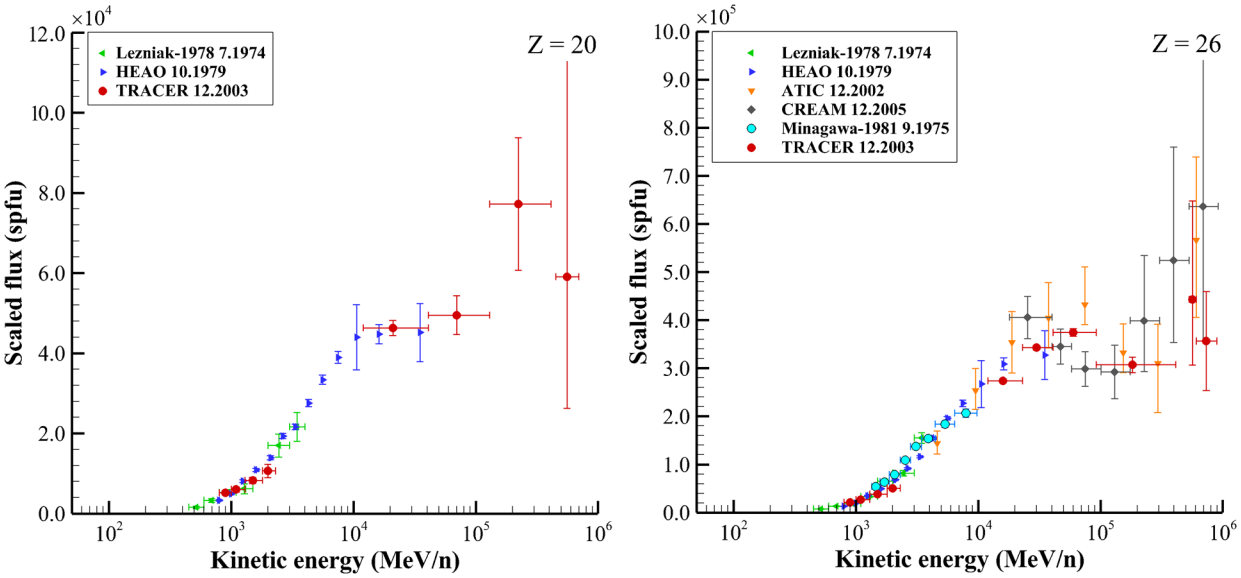

Figure C6. Z = 20 (left) and Z = 26 (right) measurement data.

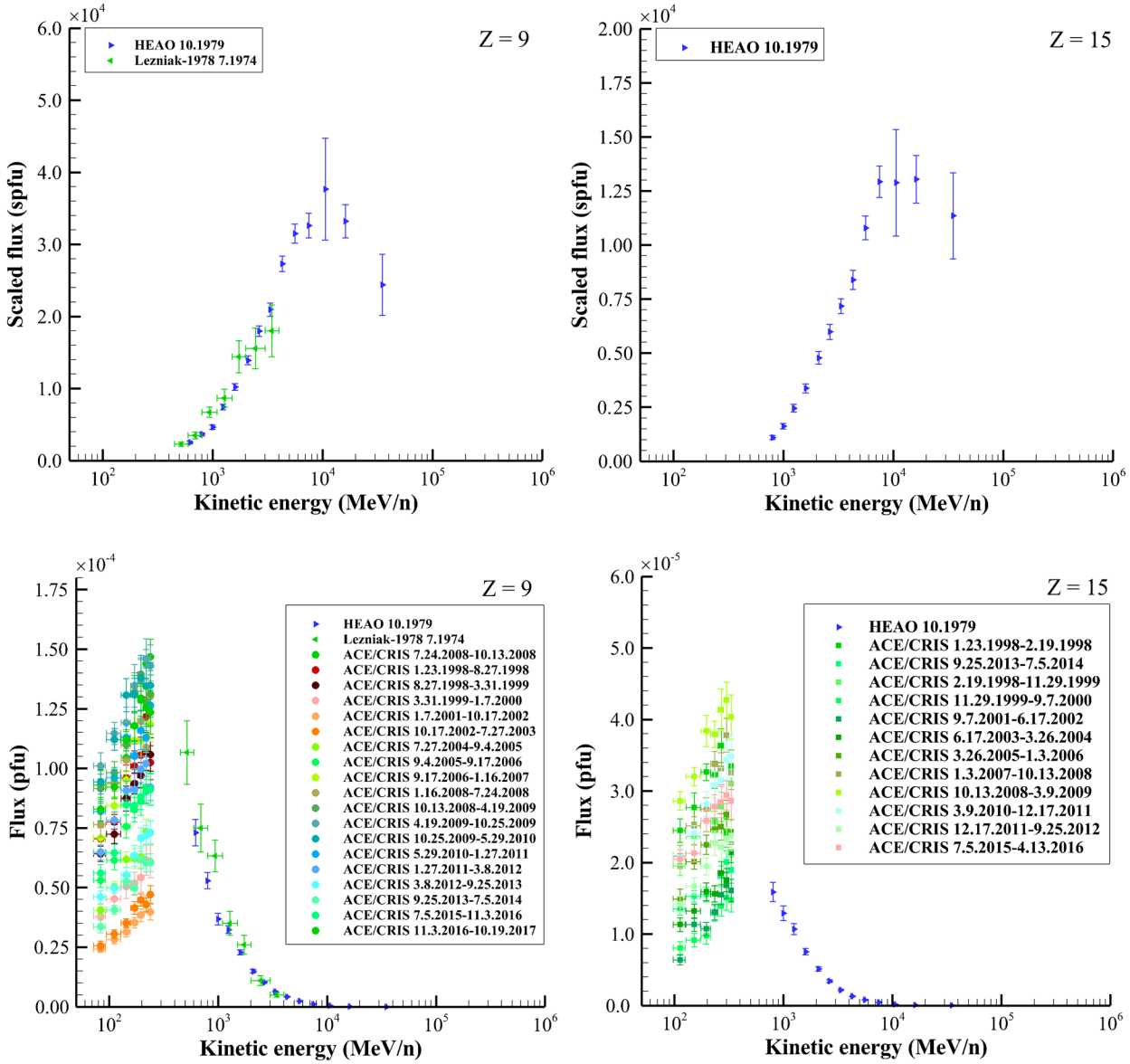

Figure C7. Z = 9 (left) and Z = 15 (right) measurement data. Fluxes in the bottom plots have not been scaled by $E^{2.7}$.

Appendix D

The particle flux unit (pfu) is defined in the plots as particles/(cm^2-MeV/n-day). Scaled fluxes shown in Figures D1 – D30 are obtained by multiplying the flux by $E^{2.7}$, where E is the kinetic energy of the particle (MeV/n). The scaled particle flux unit (spfu) is defined as particles/(cm^2-MeV/n$^{1.7}$-day).

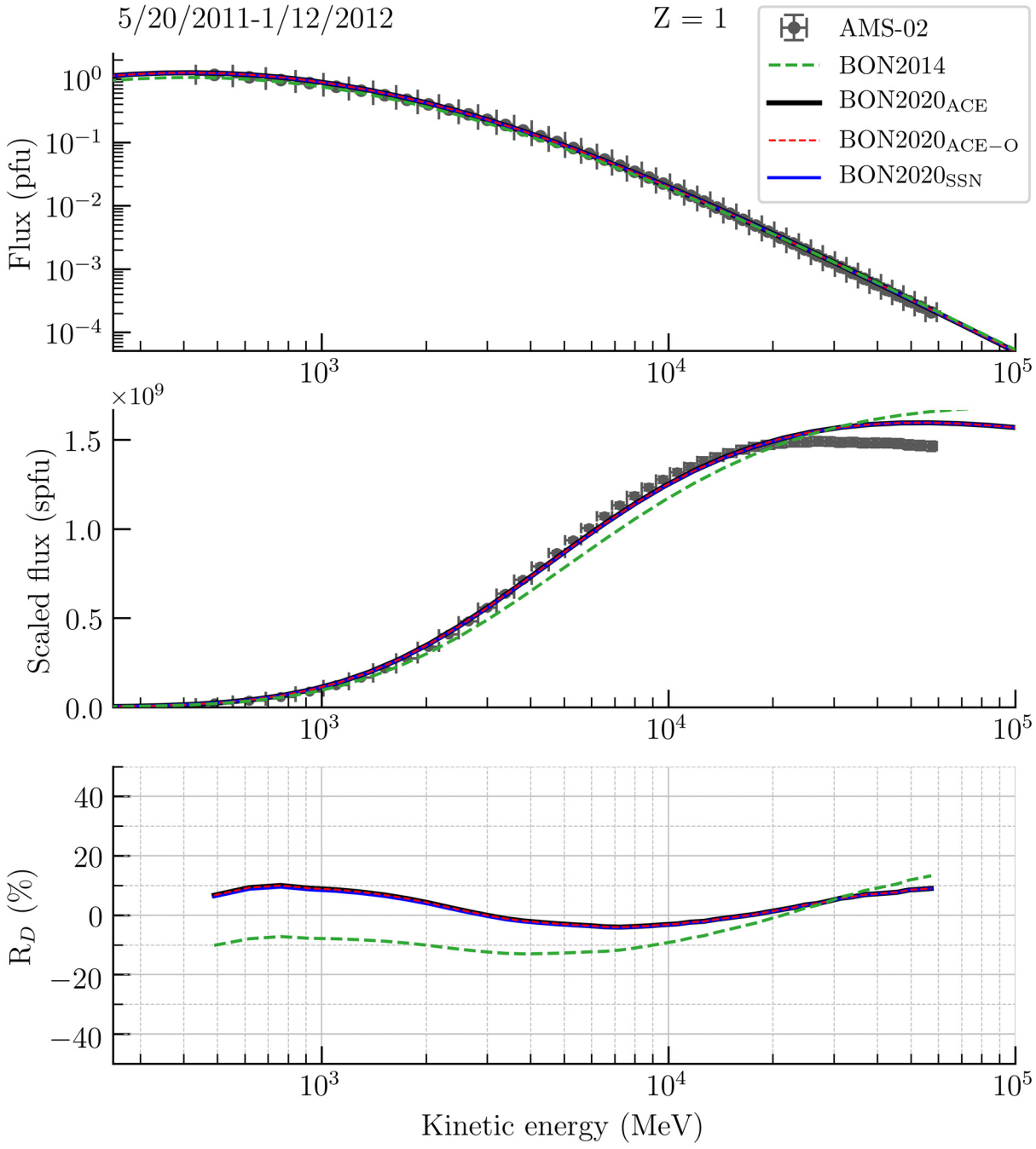

Figure D1. Comparison of model Z = 1 flux to AMS-02 measurements integrated over 5/20/2011 – 1/12/2012.

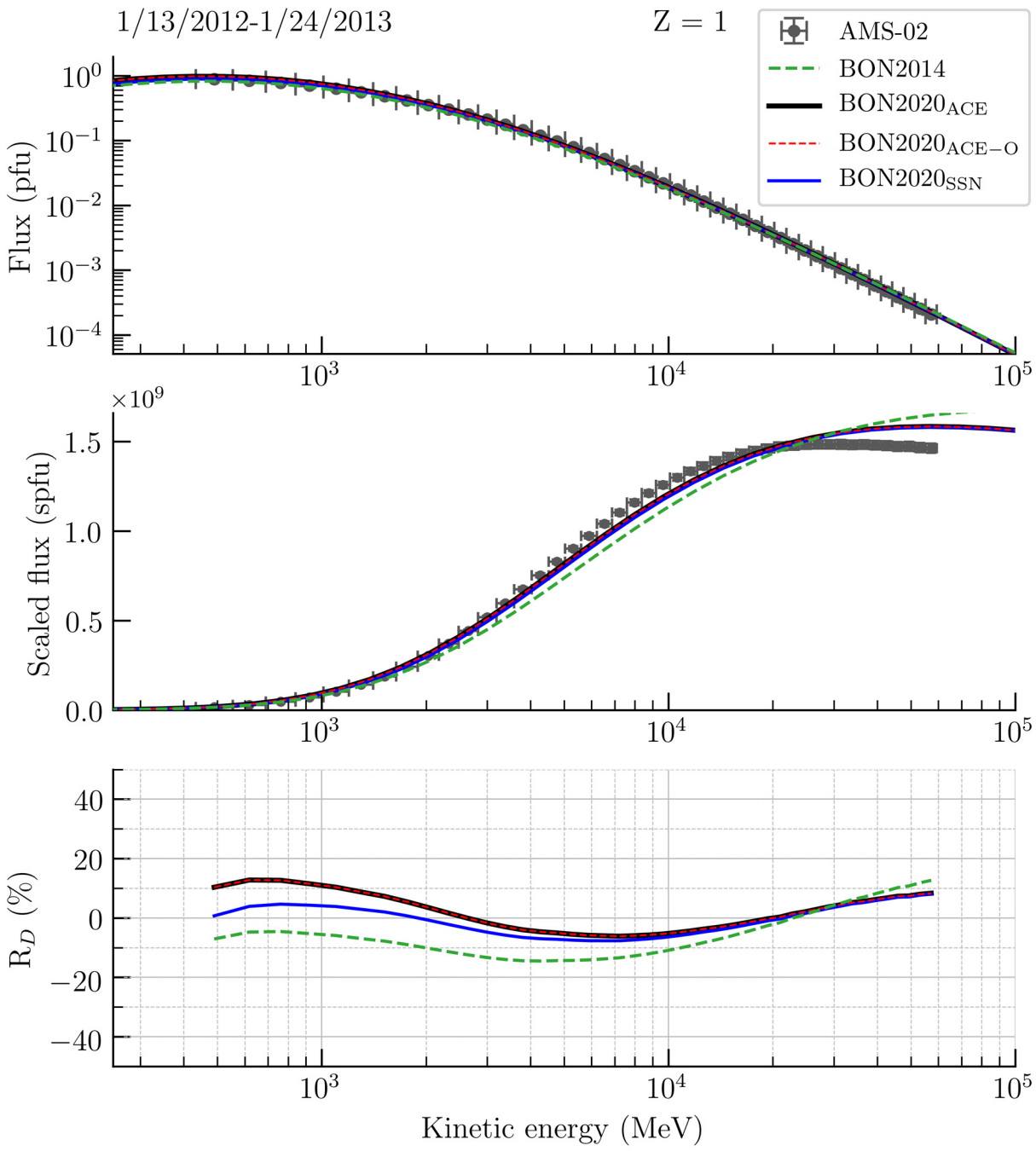

Figure D2. Comparison of model Z = 1 flux to AMS-02 measurements integrated over 1/13/2012 – 1/24/2013.

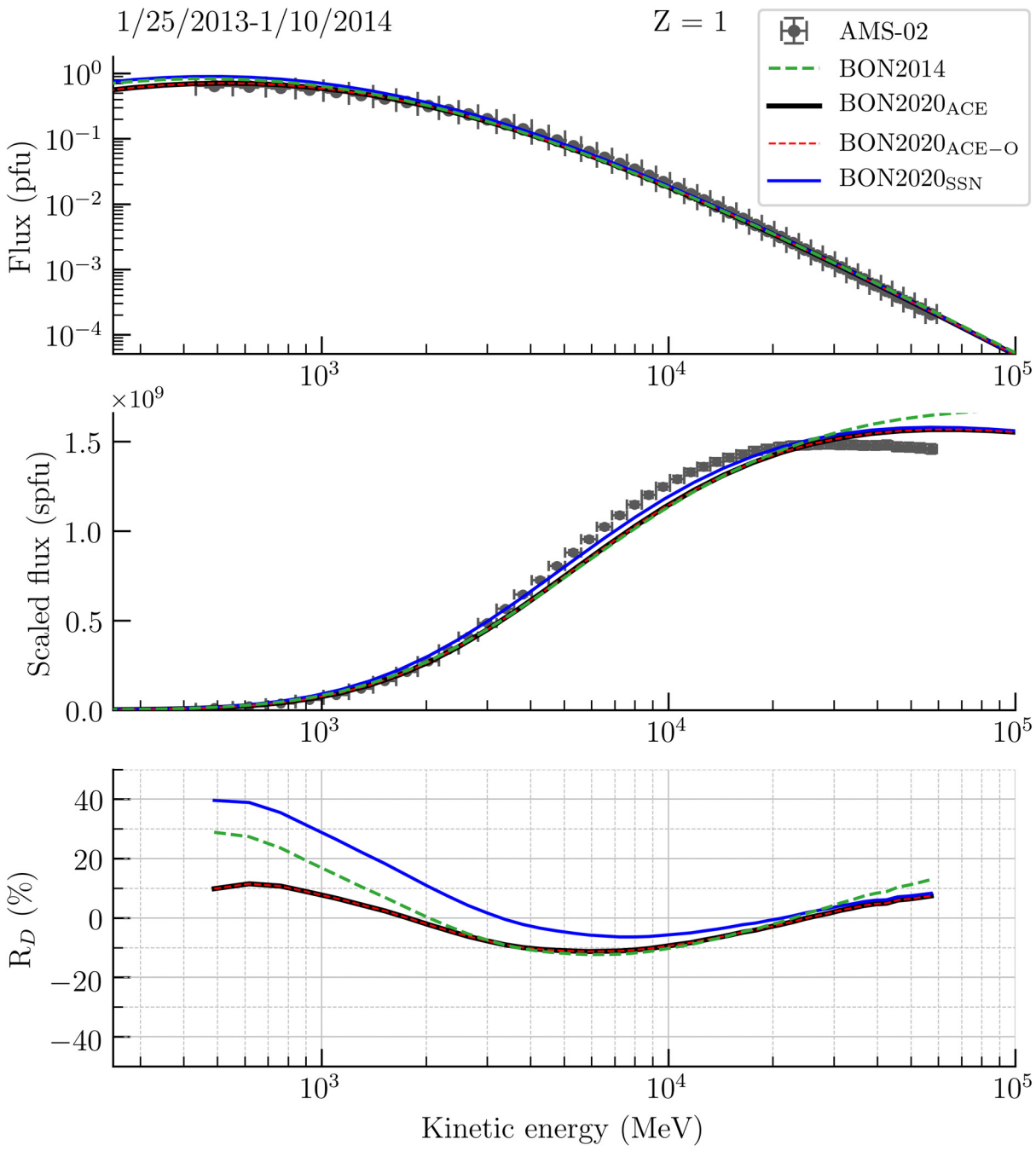

Figure D3. Comparison of model Z = 1 flux to AMS-02 measurements integrated over 1/25/2013 – 1/10/2014.

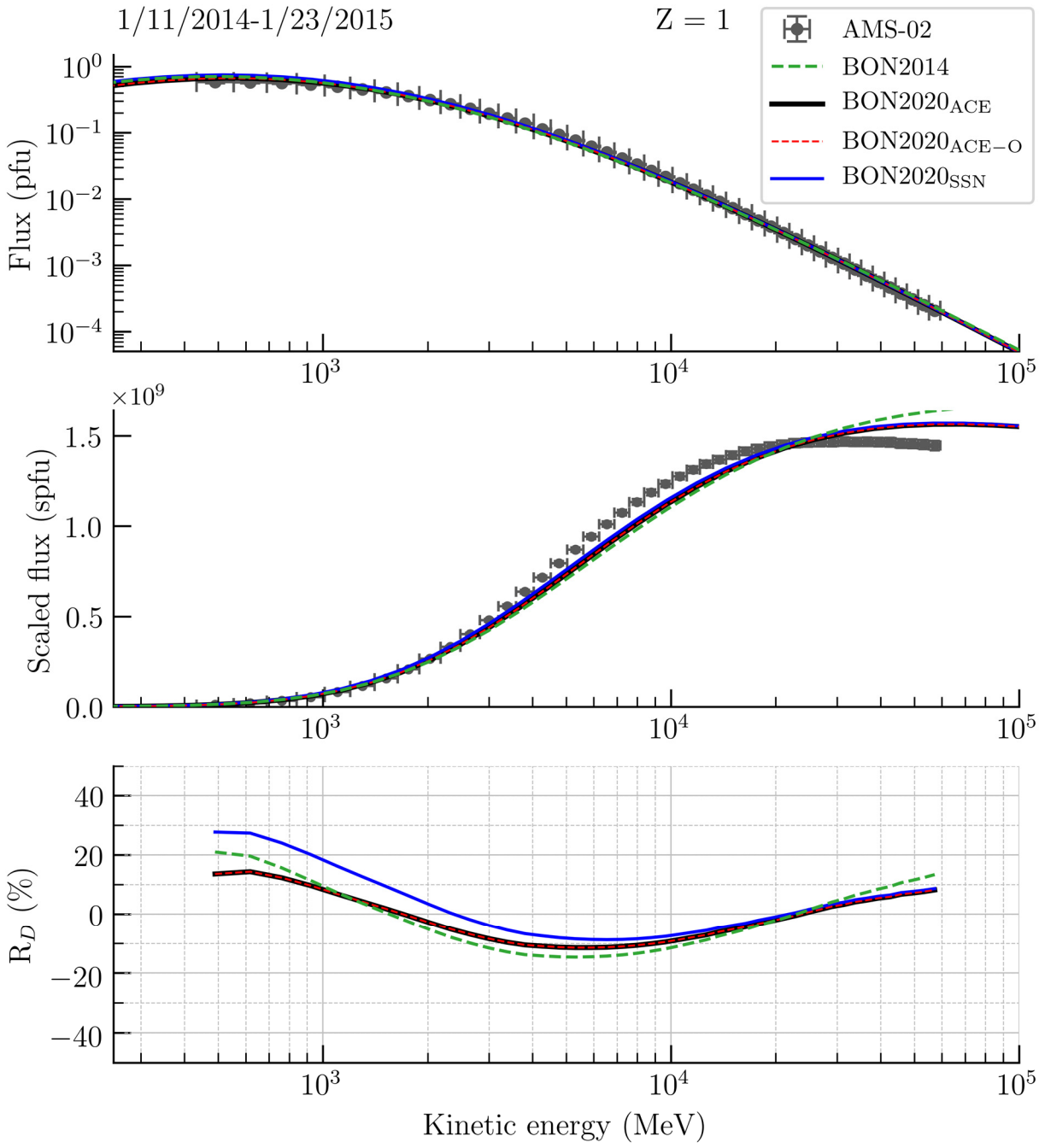

Figure D4. Comparison of model Z = 1 flux to AMS-02 measurements integrated over 1/11/2014 – 1/23/2015.

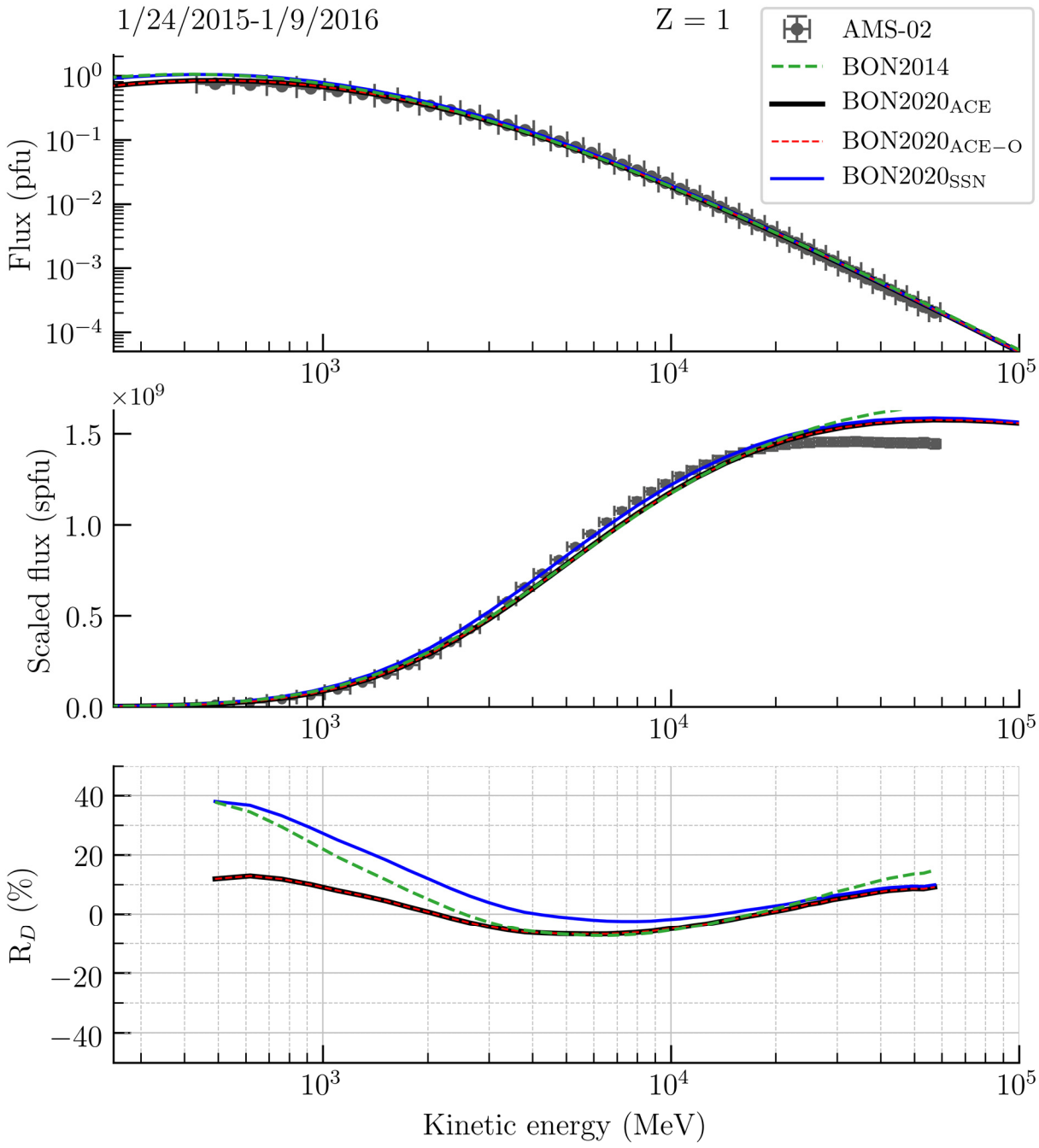

Figure D5. Comparison of model Z = 1 flux to AMS-02 measurements integrated over 1/24/2015-1/9/2016.

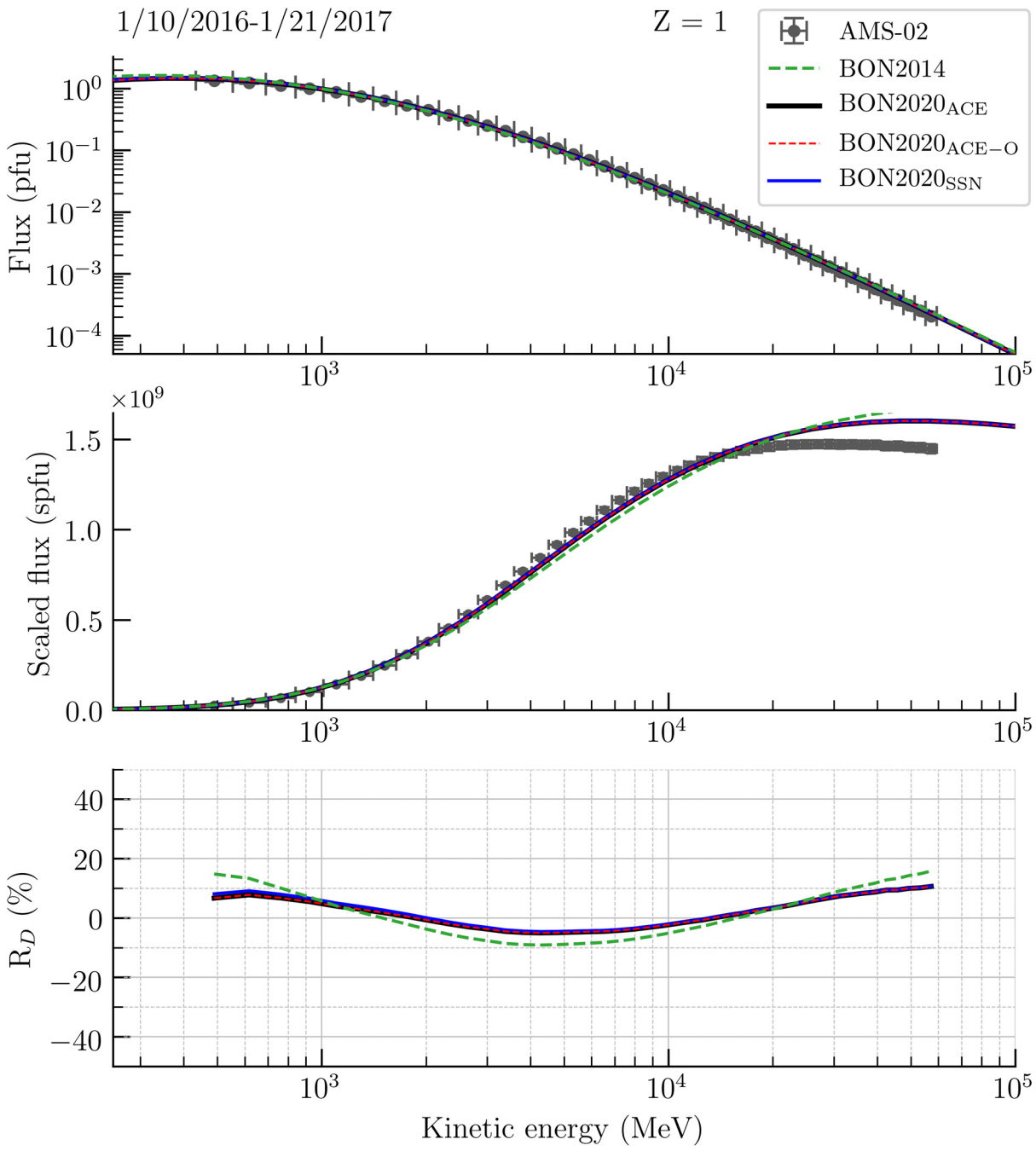

Figure D6. Comparison of model Z = 1 flux to AMS-02 measurements integrated over 1/10/2016-1/21/2017.

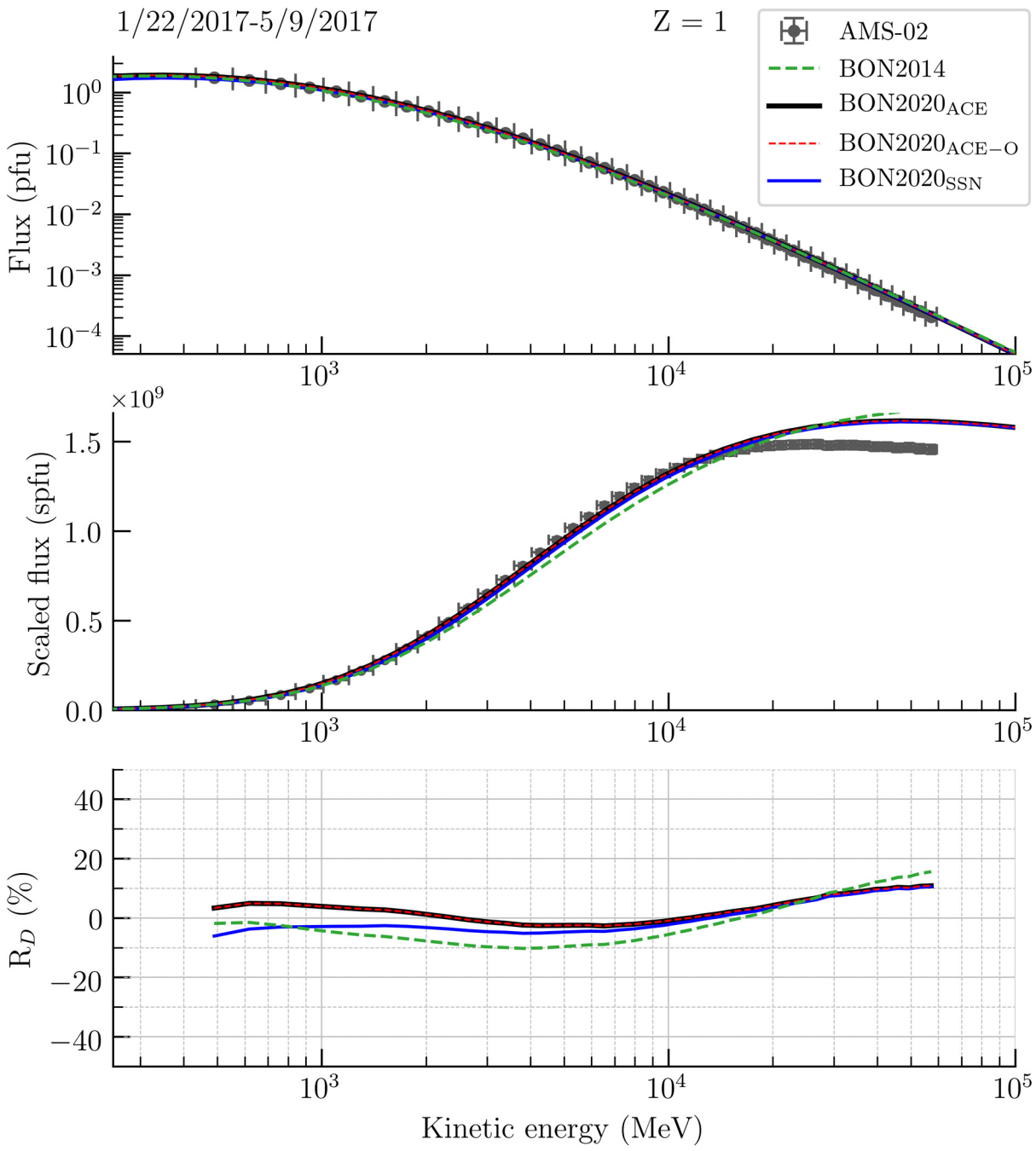

Figure D7. Comparison of model Z = 1 flux to AMS-02 measurements integrated over 1/22/2017-5/9/2017.

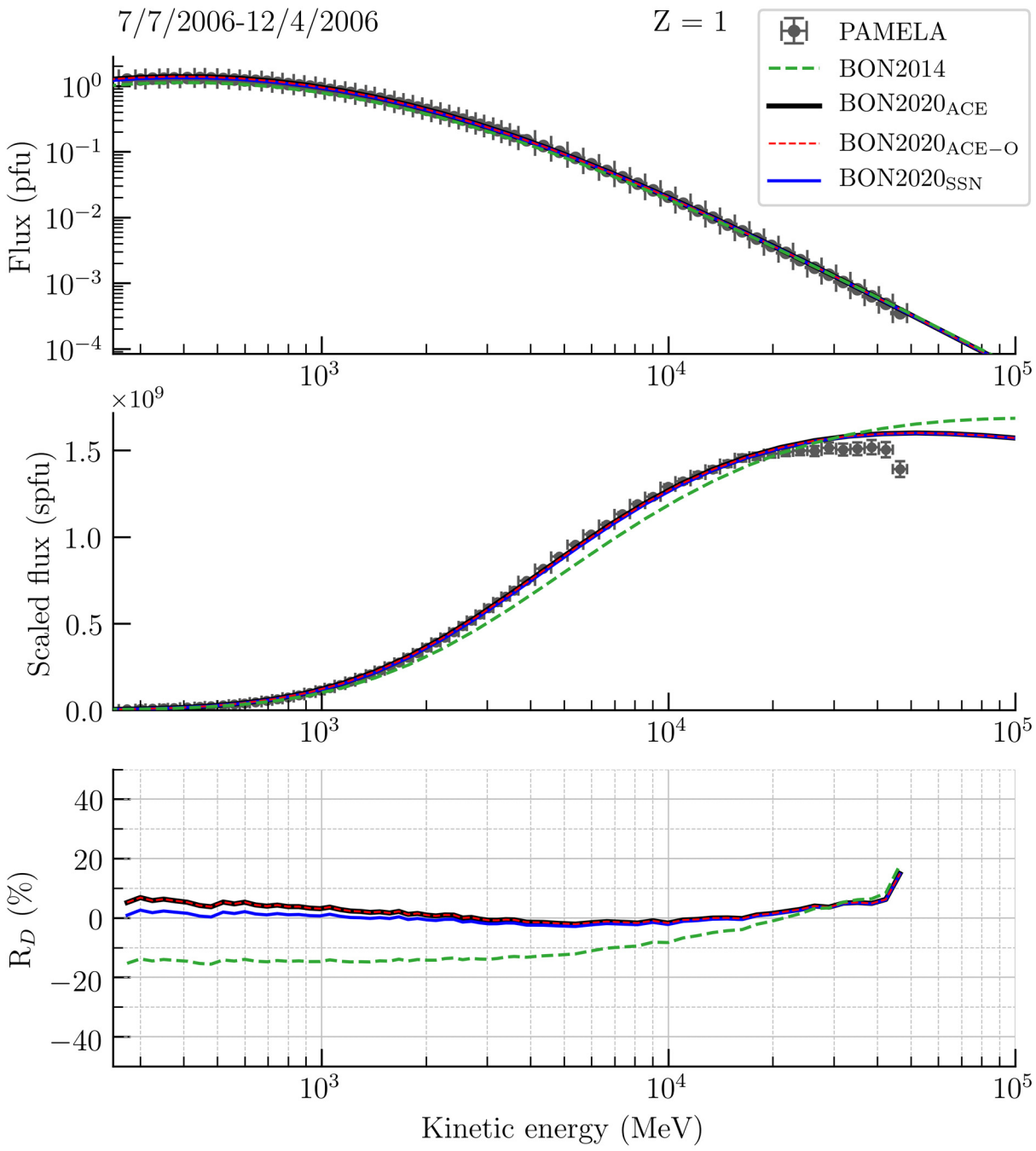

Figure D8. Comparison of model Z = 1 flux to PAMELA measurements integrated over 7/7/2006-12/4/2006.

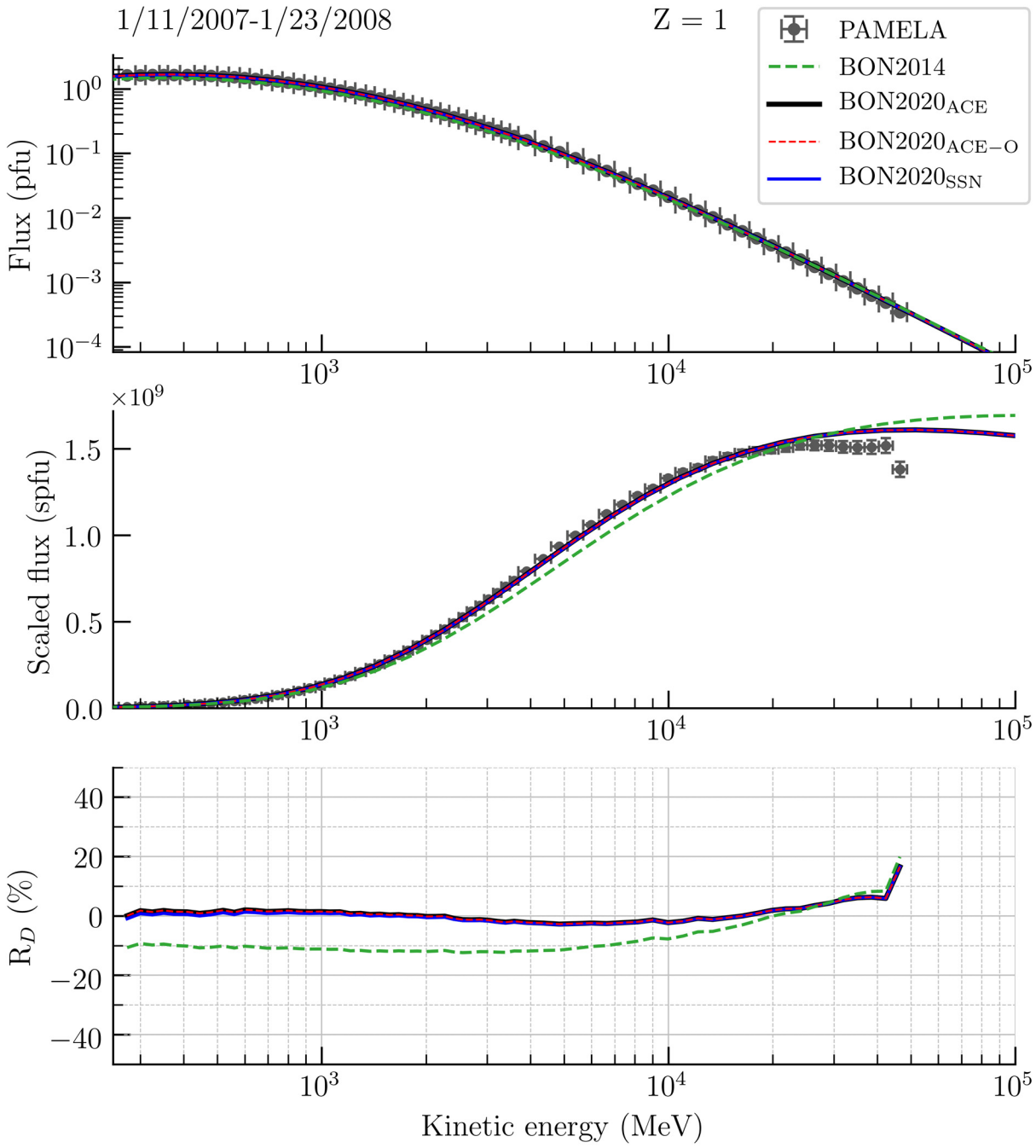

Figure D9. Comparison of model Z = 1 flux to PAMELA measurements integrated over 1/11/2007-1/23/2008.

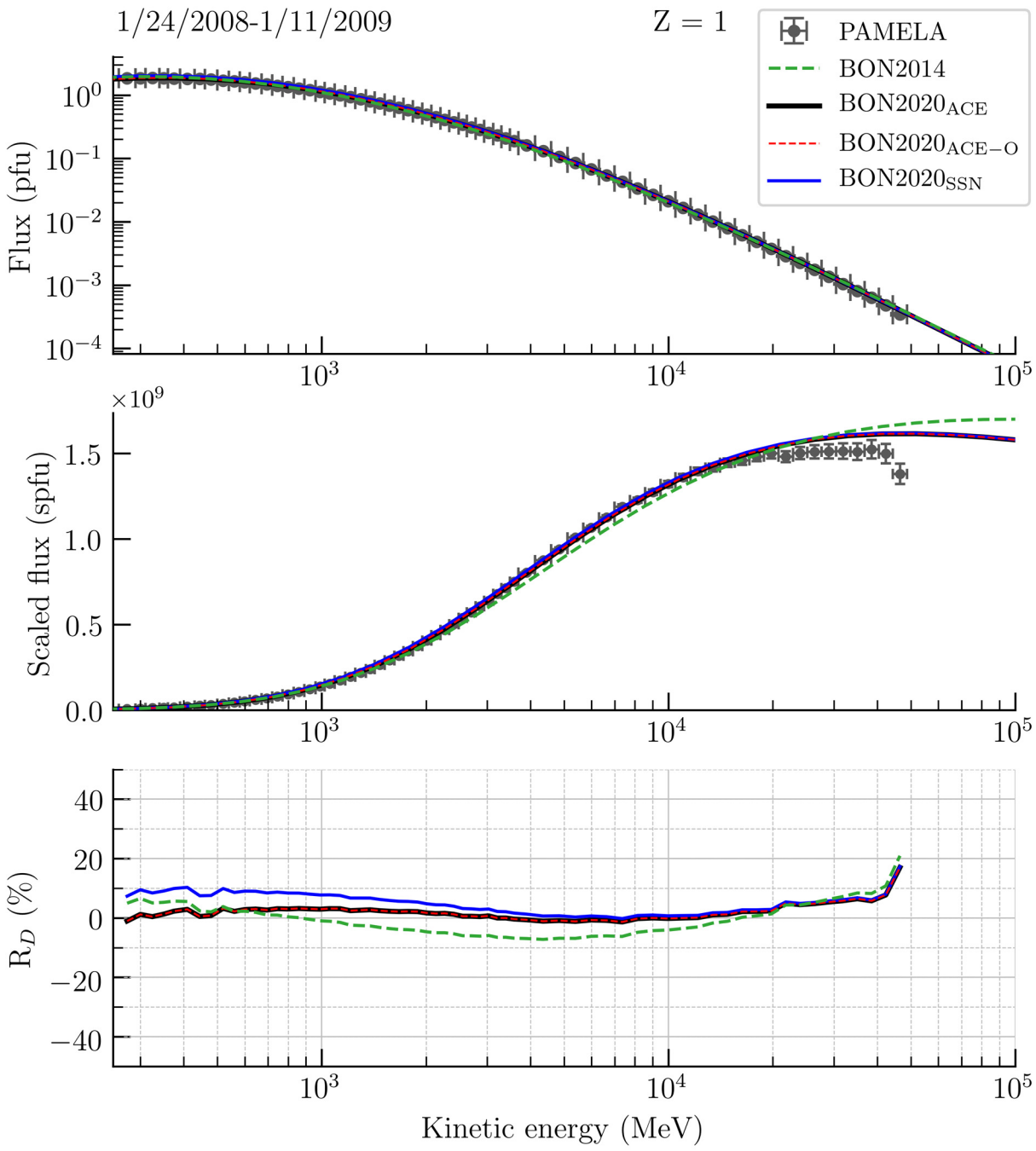

Figure D10. Comparison of model Z = 1 flux to PAMELA measurements integrated over 1/24/2008-1/11/2009.

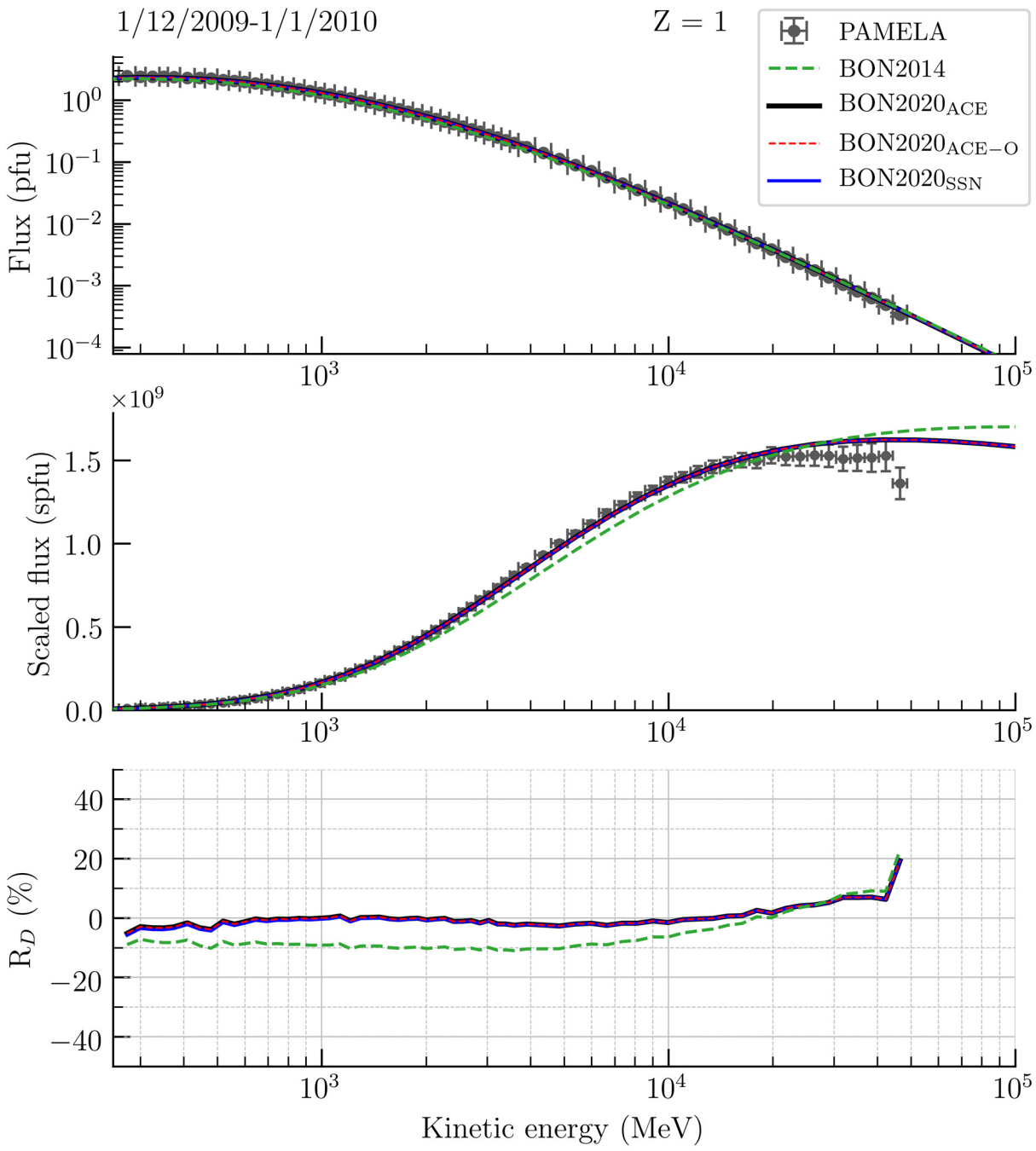

Figure D11. Comparison of model Z = 1 flux to PAMELA measurements integrated over 1/12/2009-1/1/2010.

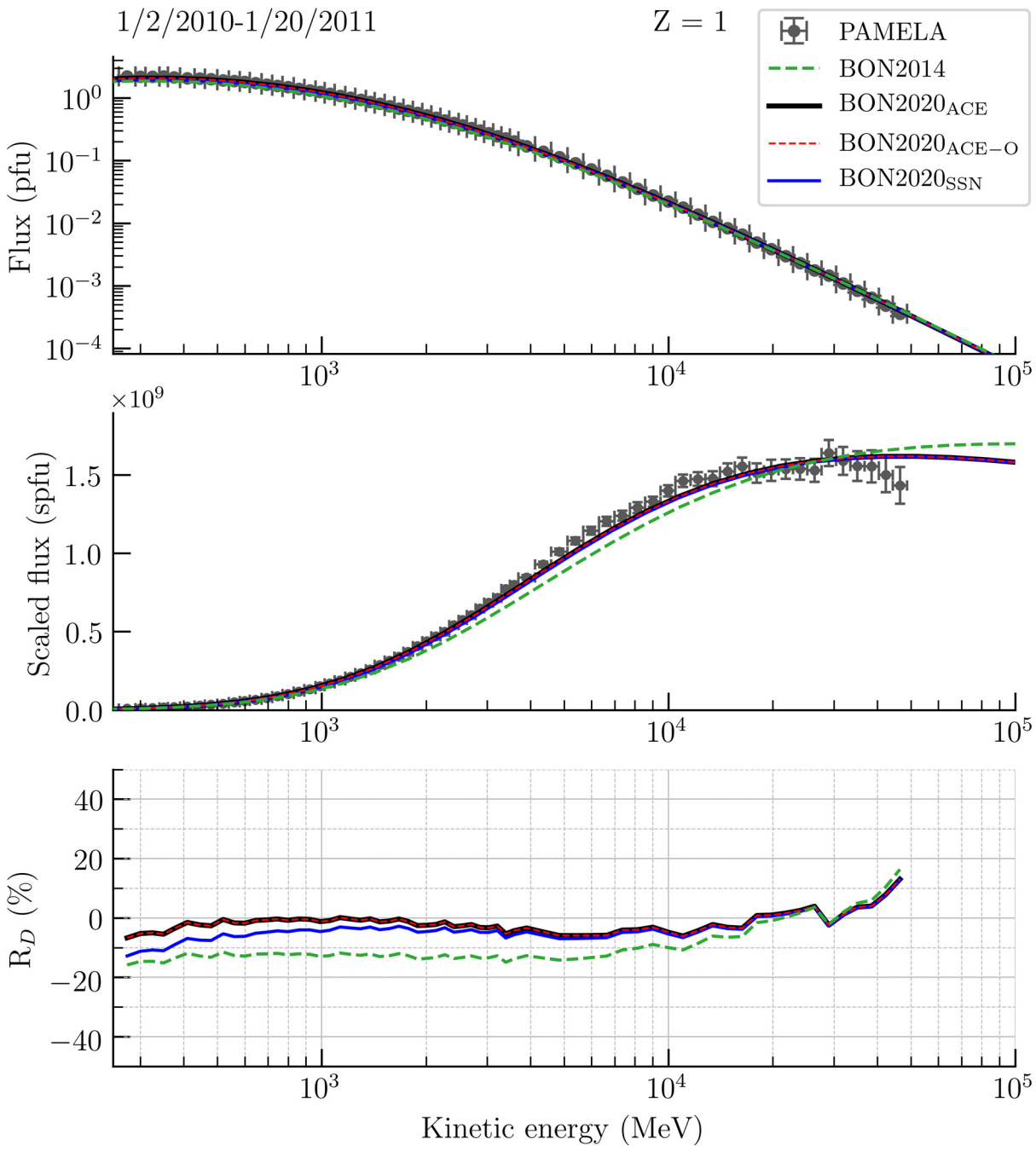

Figure D12. Comparison of model Z = 1 flux to PAMELA measurements integrated over 1/2/2010-1/20/2011.

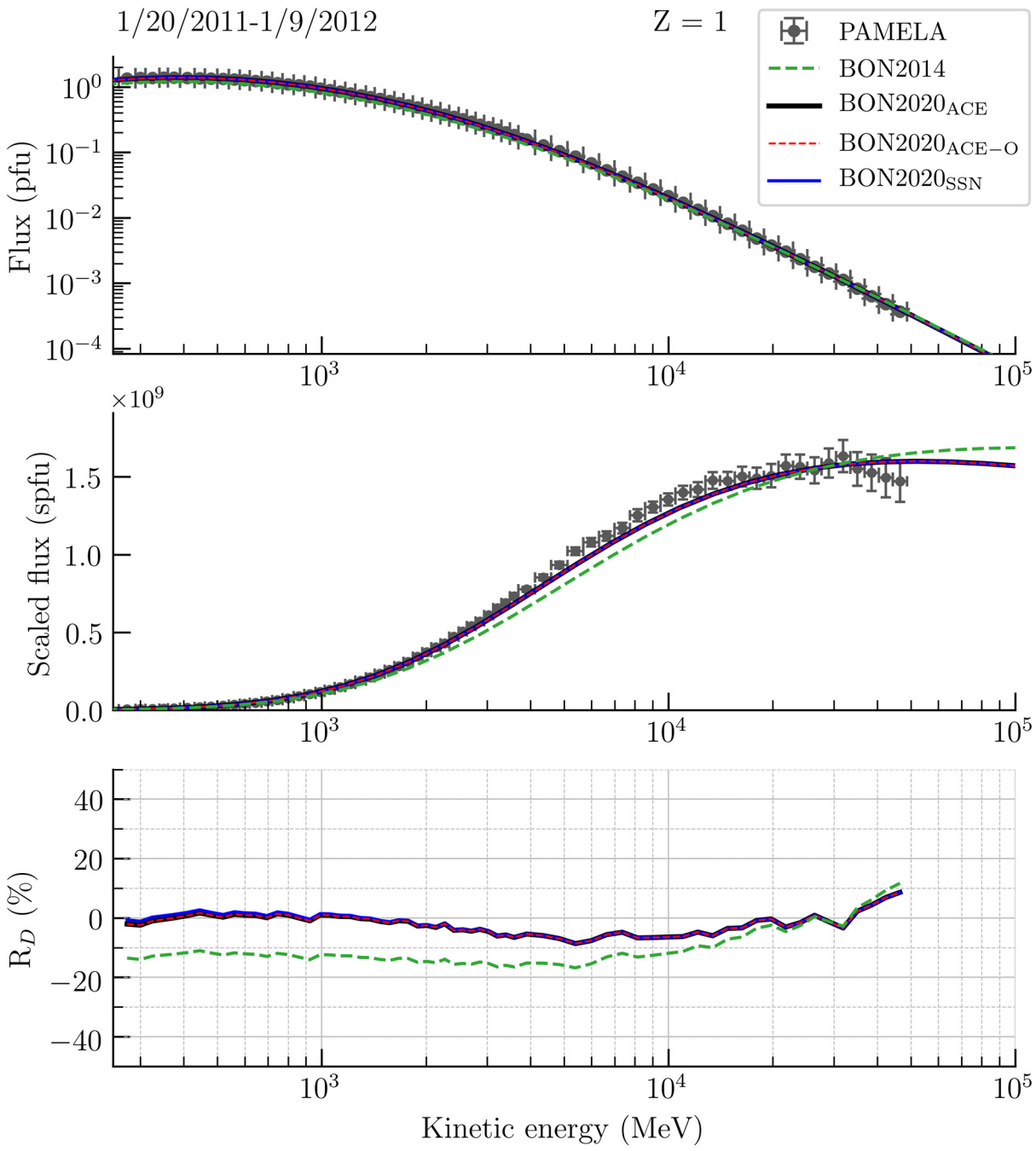

Figure D13. Comparison of model Z = 1 flux to PAMELA measurements integrated over 1/20/2011-1/9/2012.

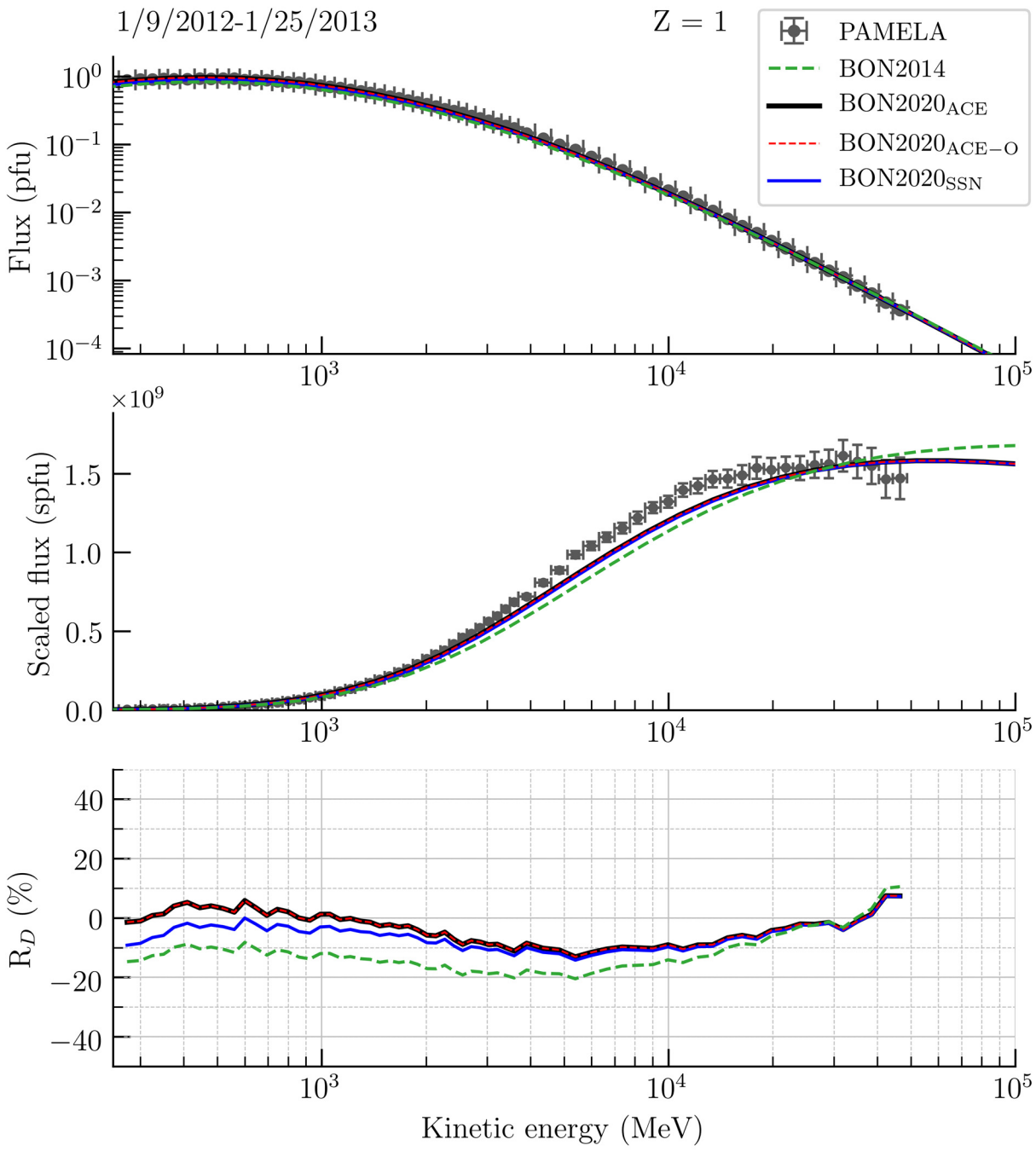

Figure D14. Comparison of model Z = 1 flux to PAMELA measurements integrated over 1/9/2012-1/25/2013.

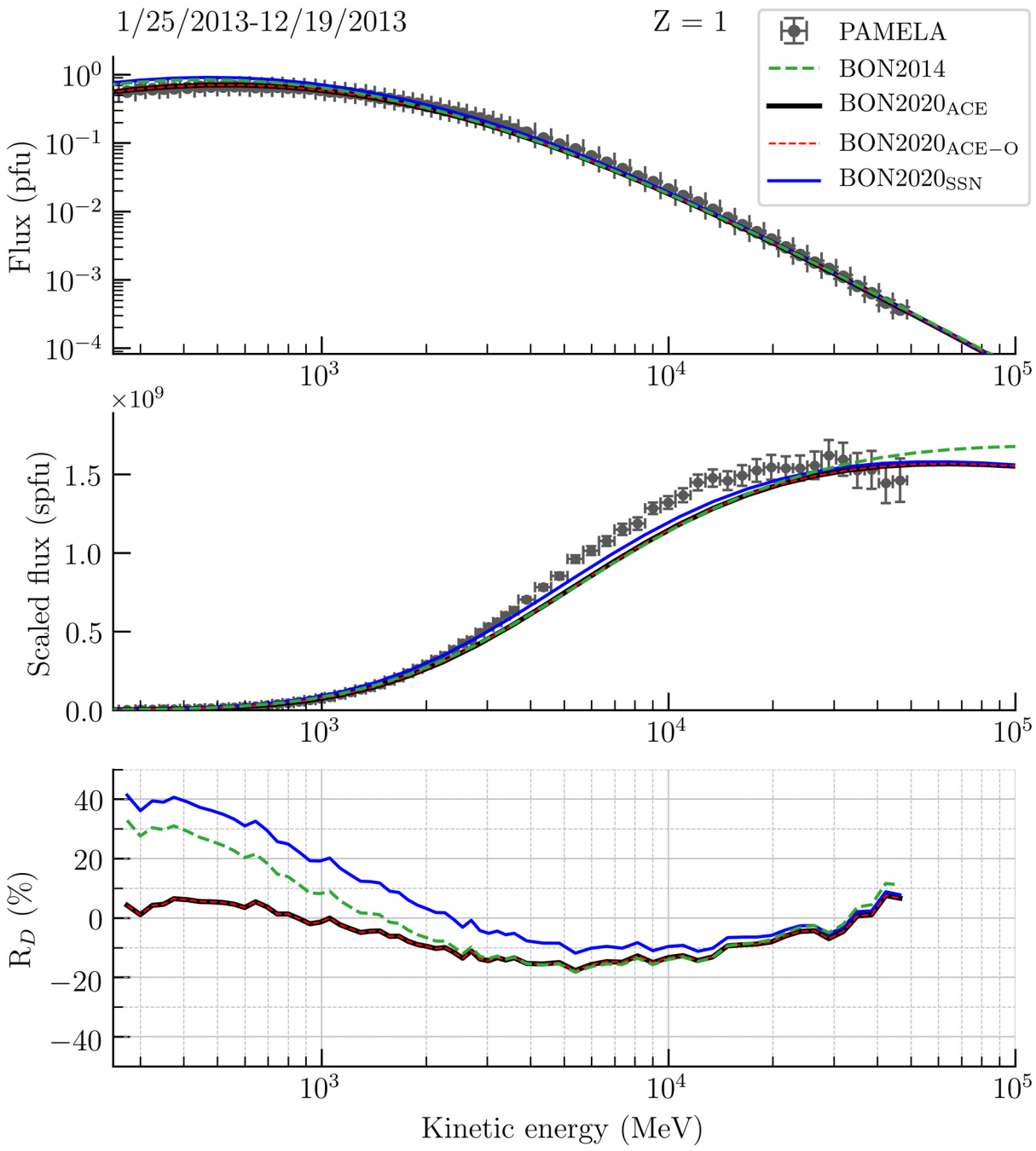

Figure D15. Comparison of model Z = 1 flux to PAMELA measurements integrated over 1/25/2013-12/19/2013.

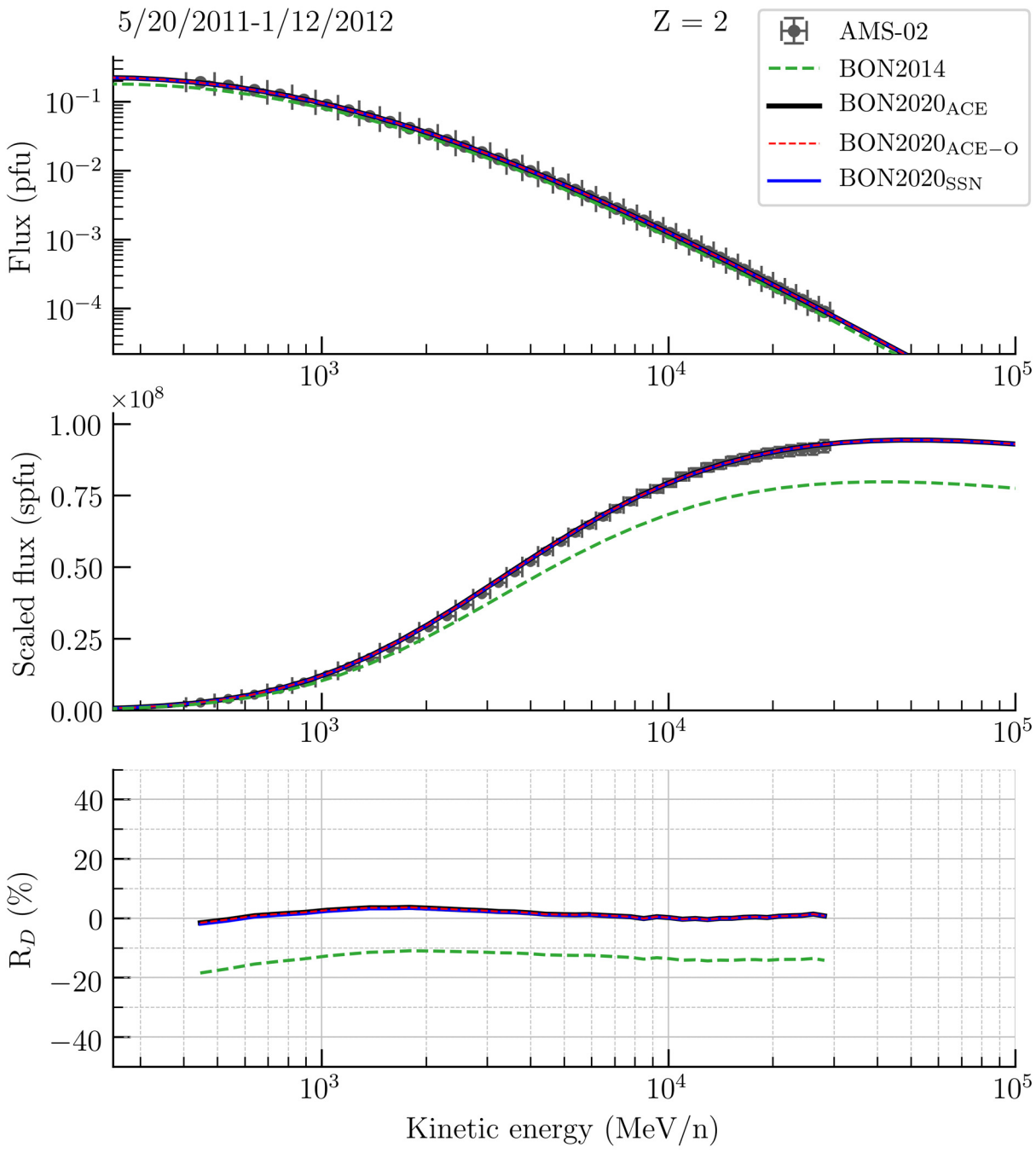

Figure D16. Comparison of model Z = 2 flux to AMS-02 measurements integrated over 5/20/2011 – 1/12/2012.

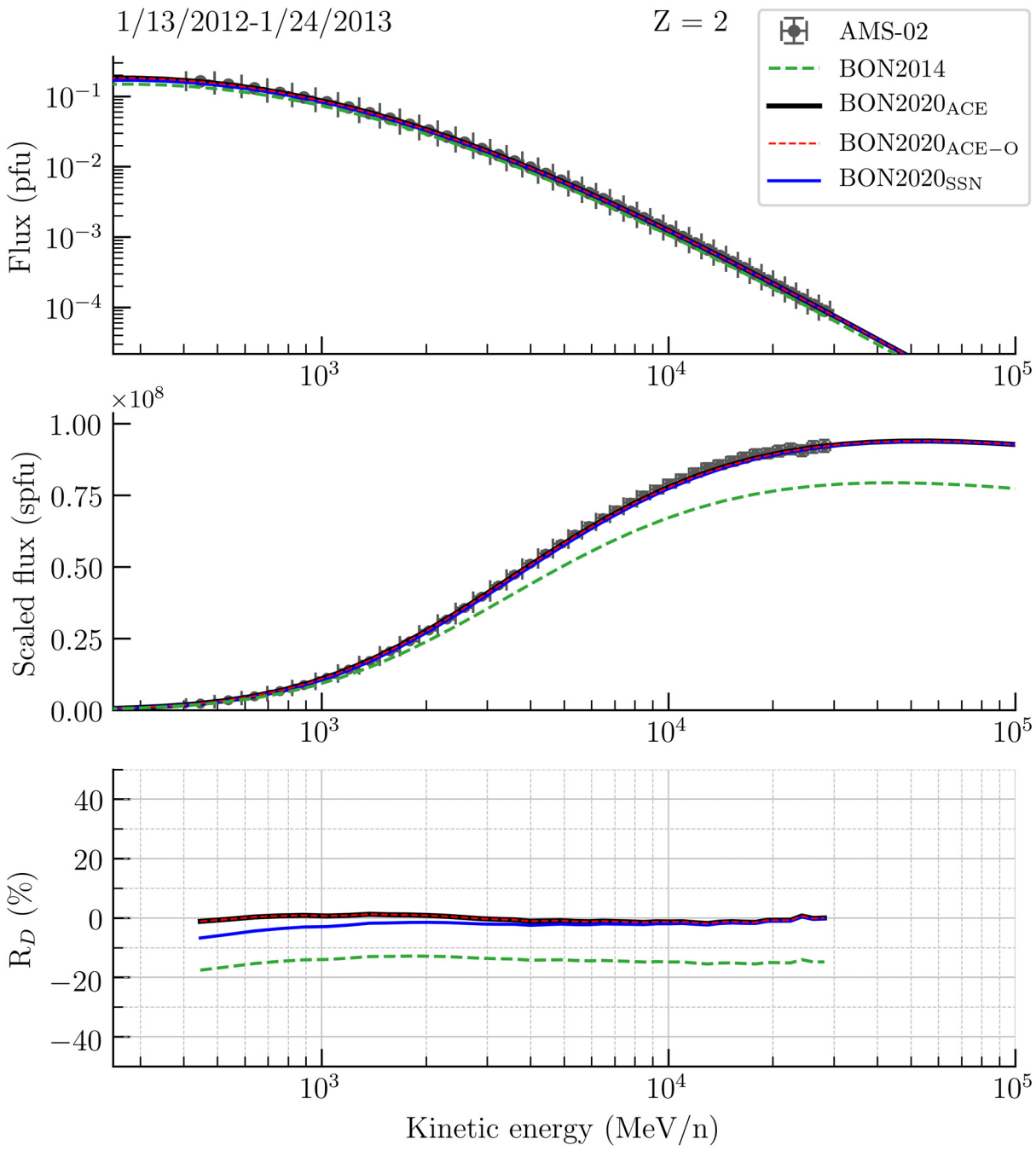

Figure D17. Comparison of model Z = 2 flux to AMS-02 measurements integrated over 1/13/2012-1/24/2013.

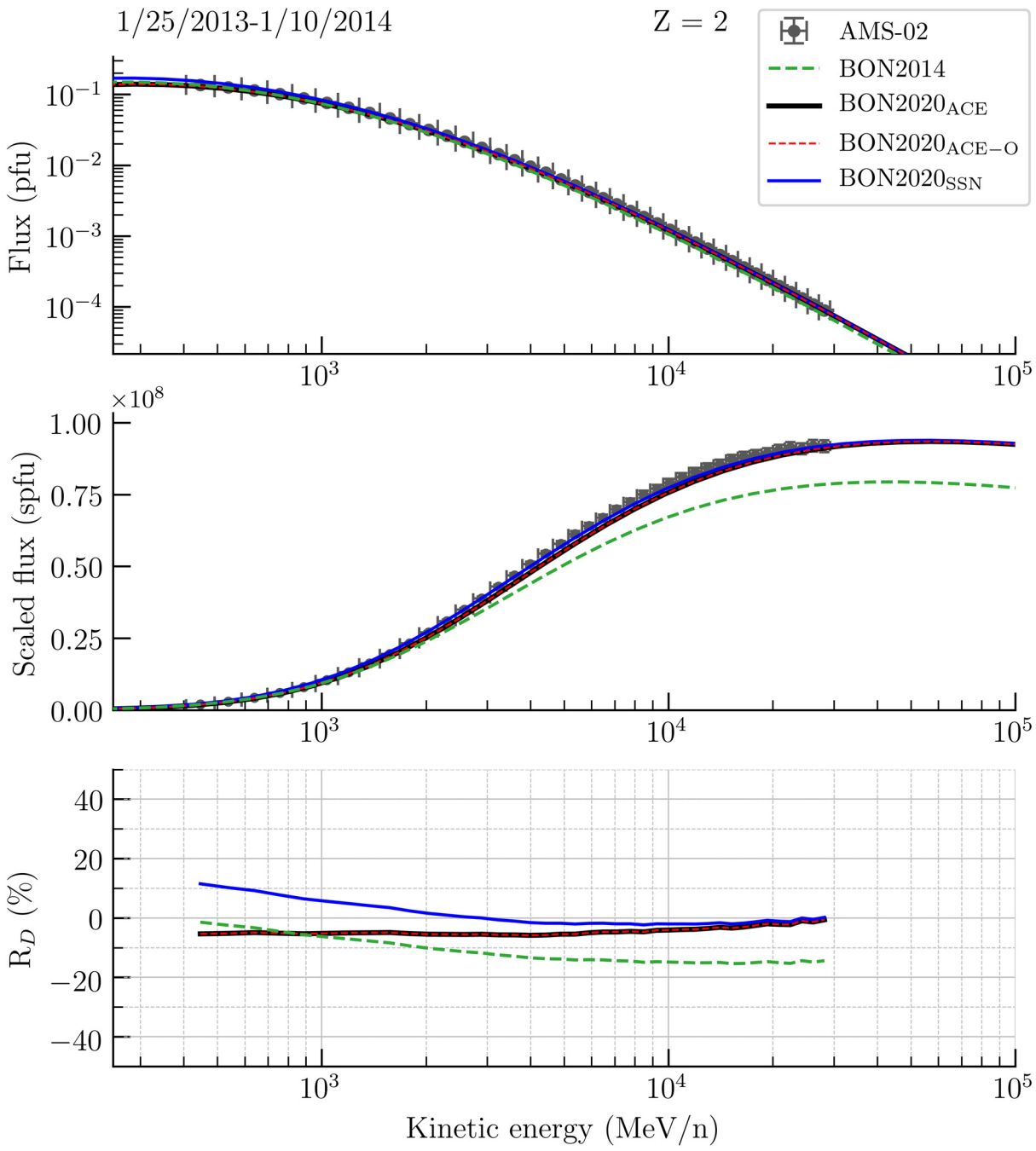

Figure D18. Comparison of model Z = 2 flux to AMS-02 measurements integrated over 1/25/2013-1/10/2014.

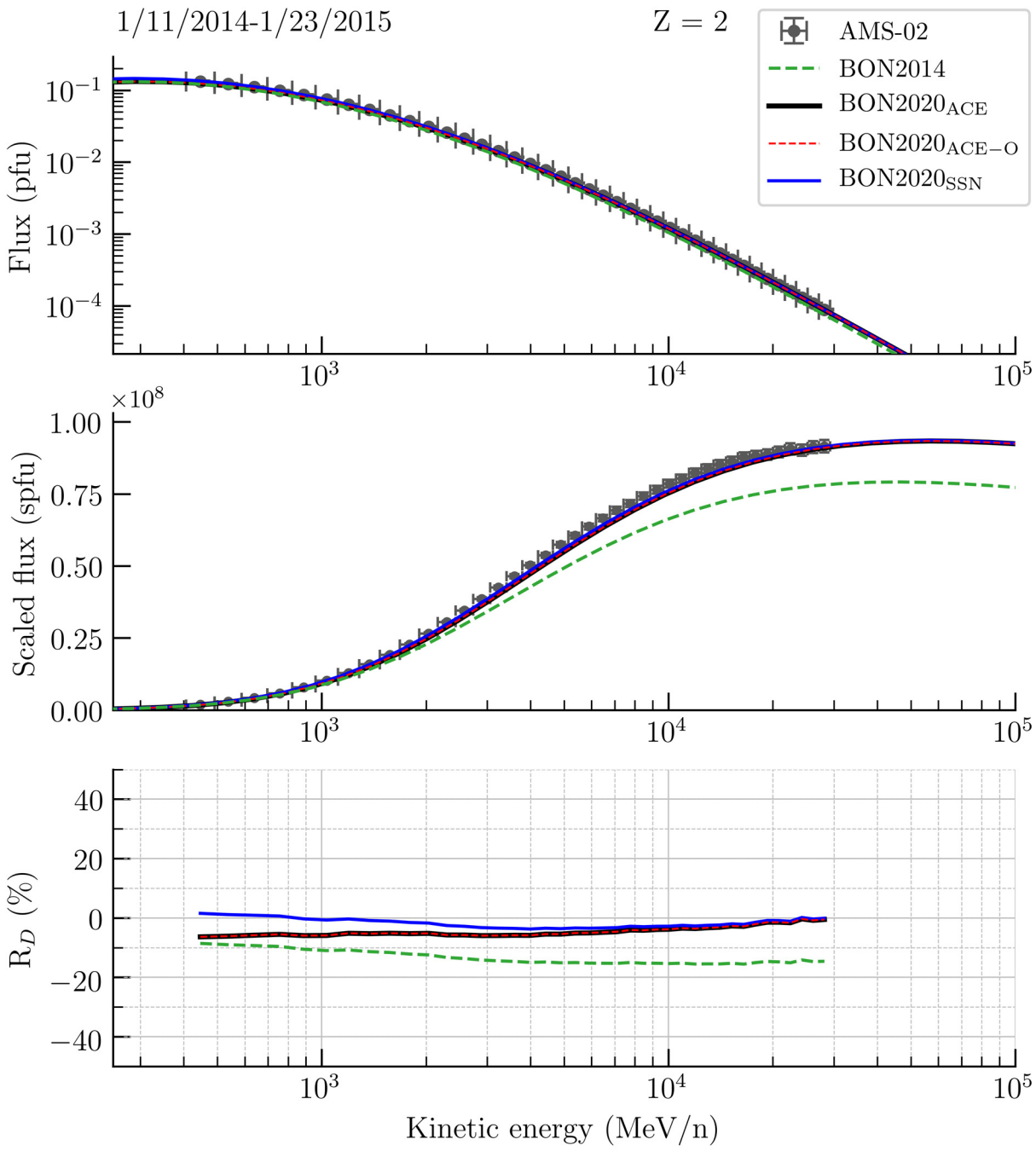

Figure D19. Comparison of model Z = 2 flux to AMS-02 measurements integrated over 1/11/2014-1/23/2015.

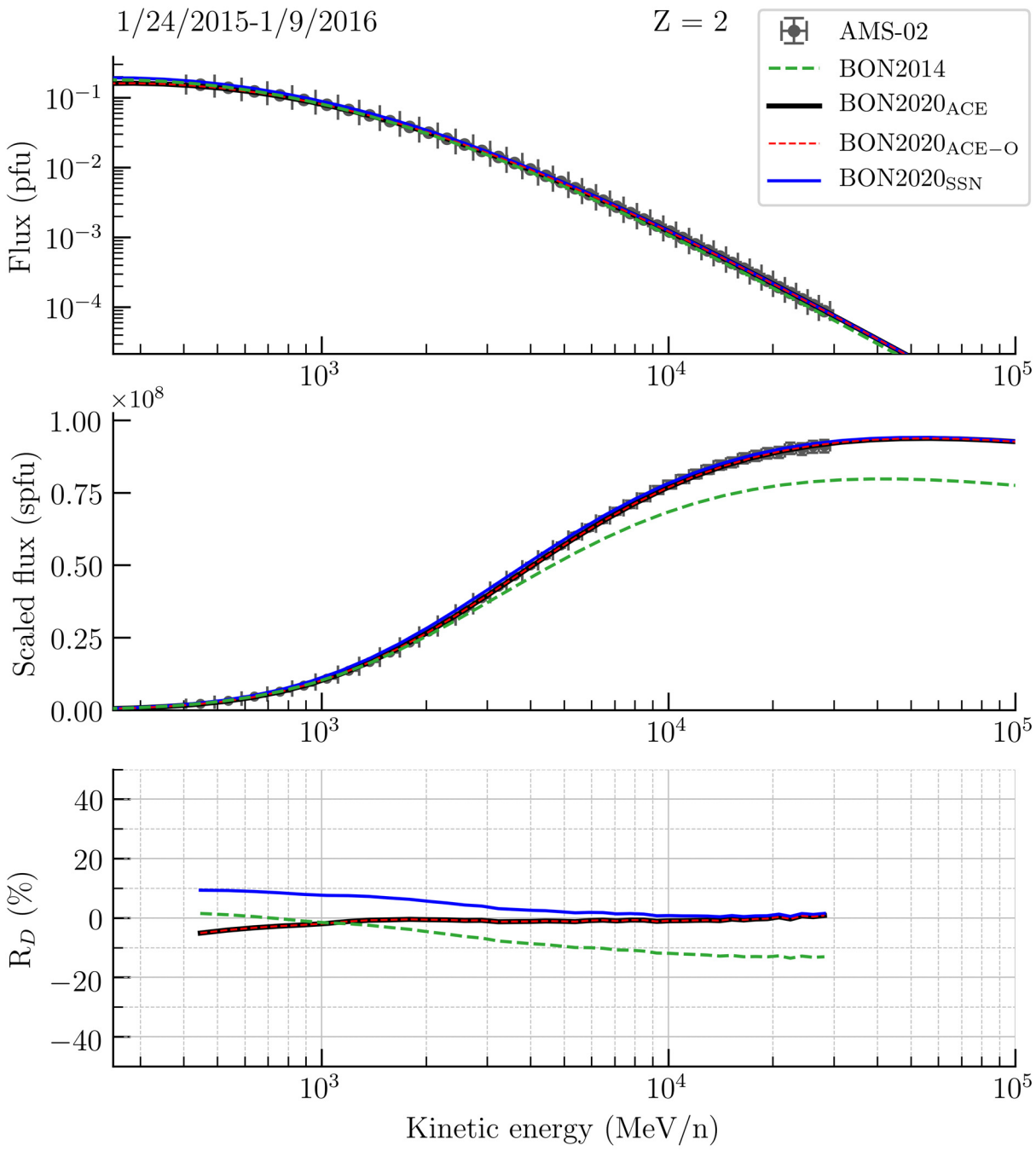

Figure D20. Comparison of model Z = 2 flux to AMS-02 measurements integrated over 1/24/2015-1/9/2016.

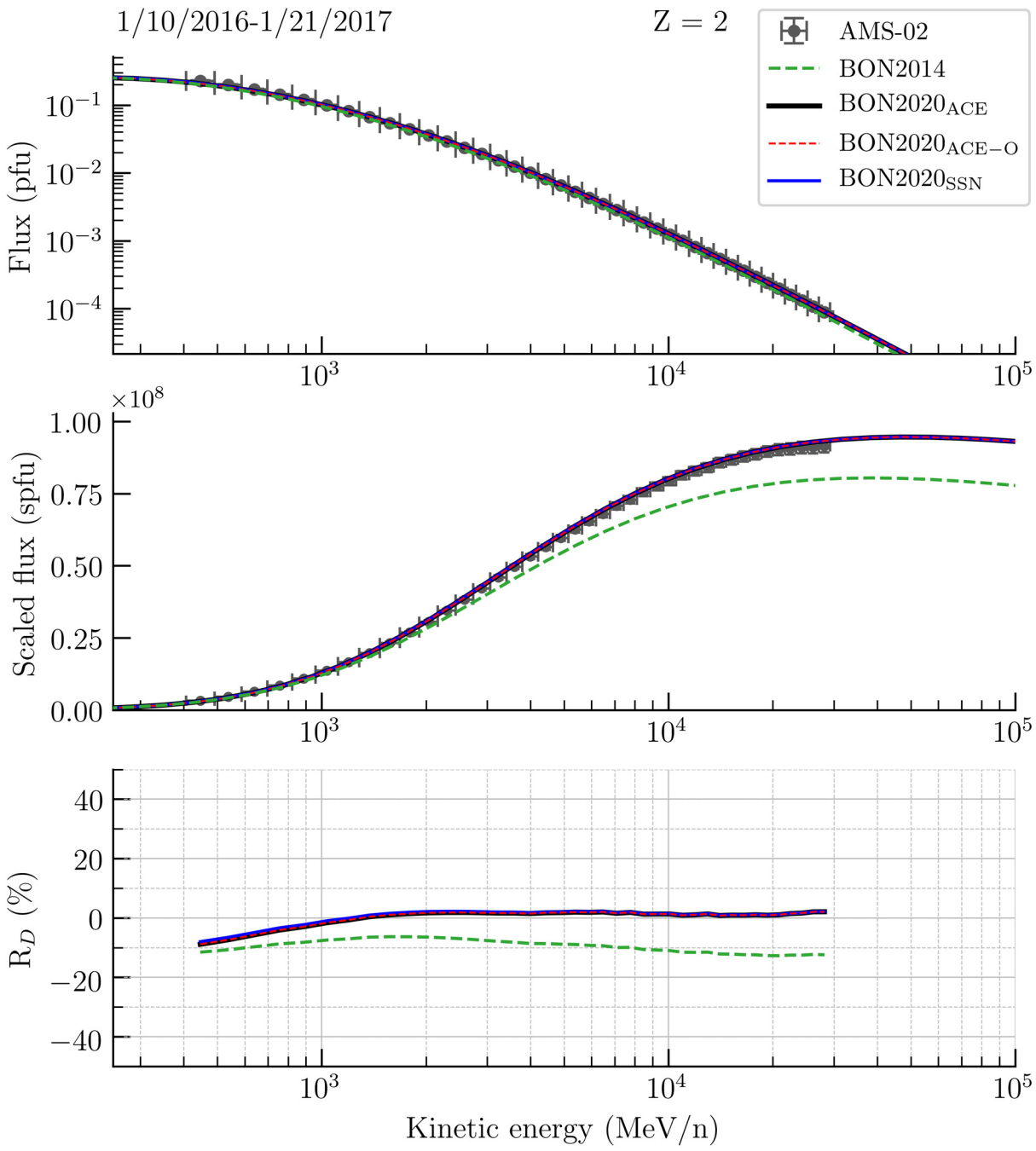

Figure D21. Comparison of model Z = 2 flux to AMS-02 measurements integrated over 1/10/2016-1/21/2017.

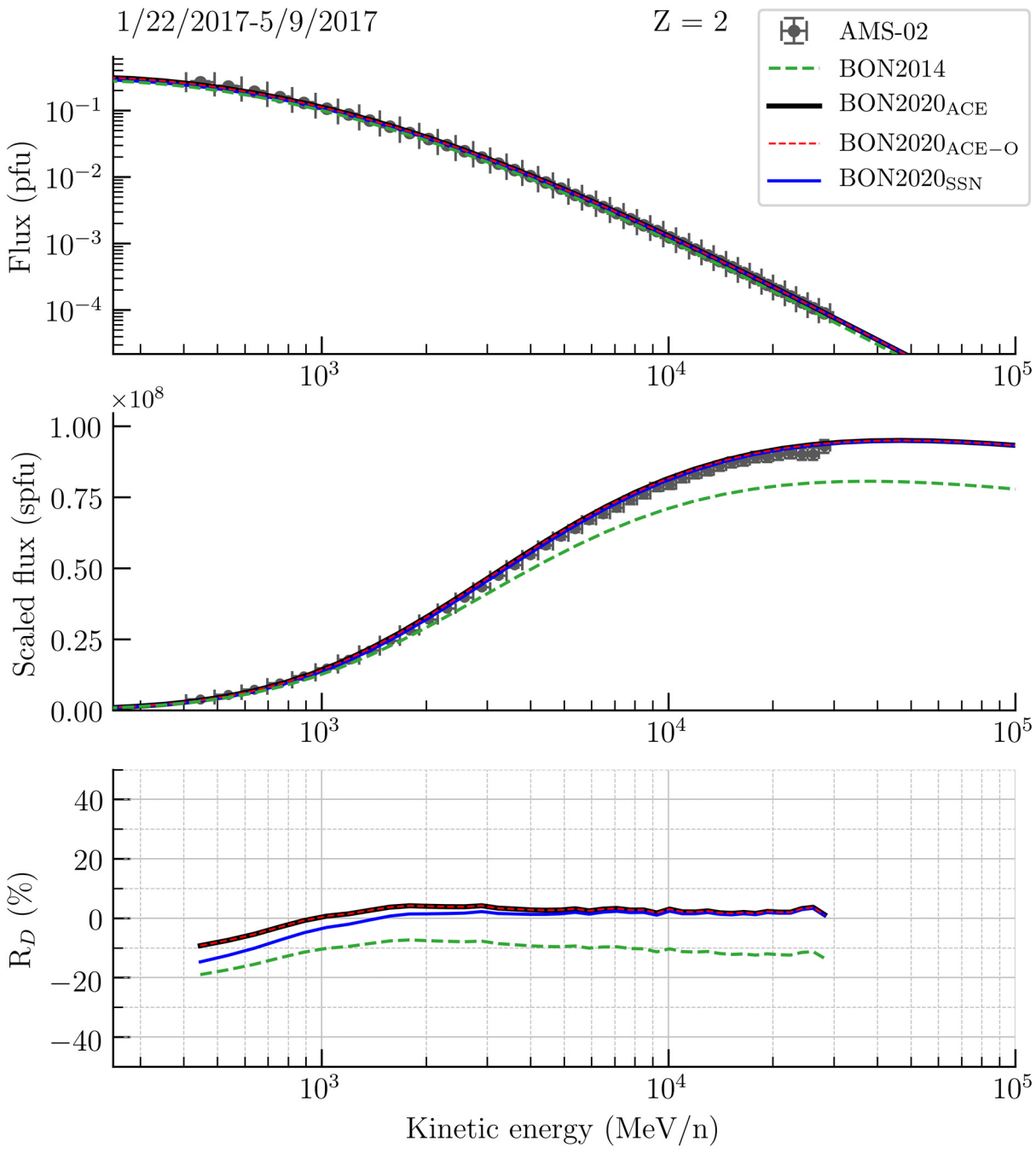

Figure D22. Comparison of model Z = 2 flux to AMS-02 measurements integrated over 1/22/2017-5/9/2017.

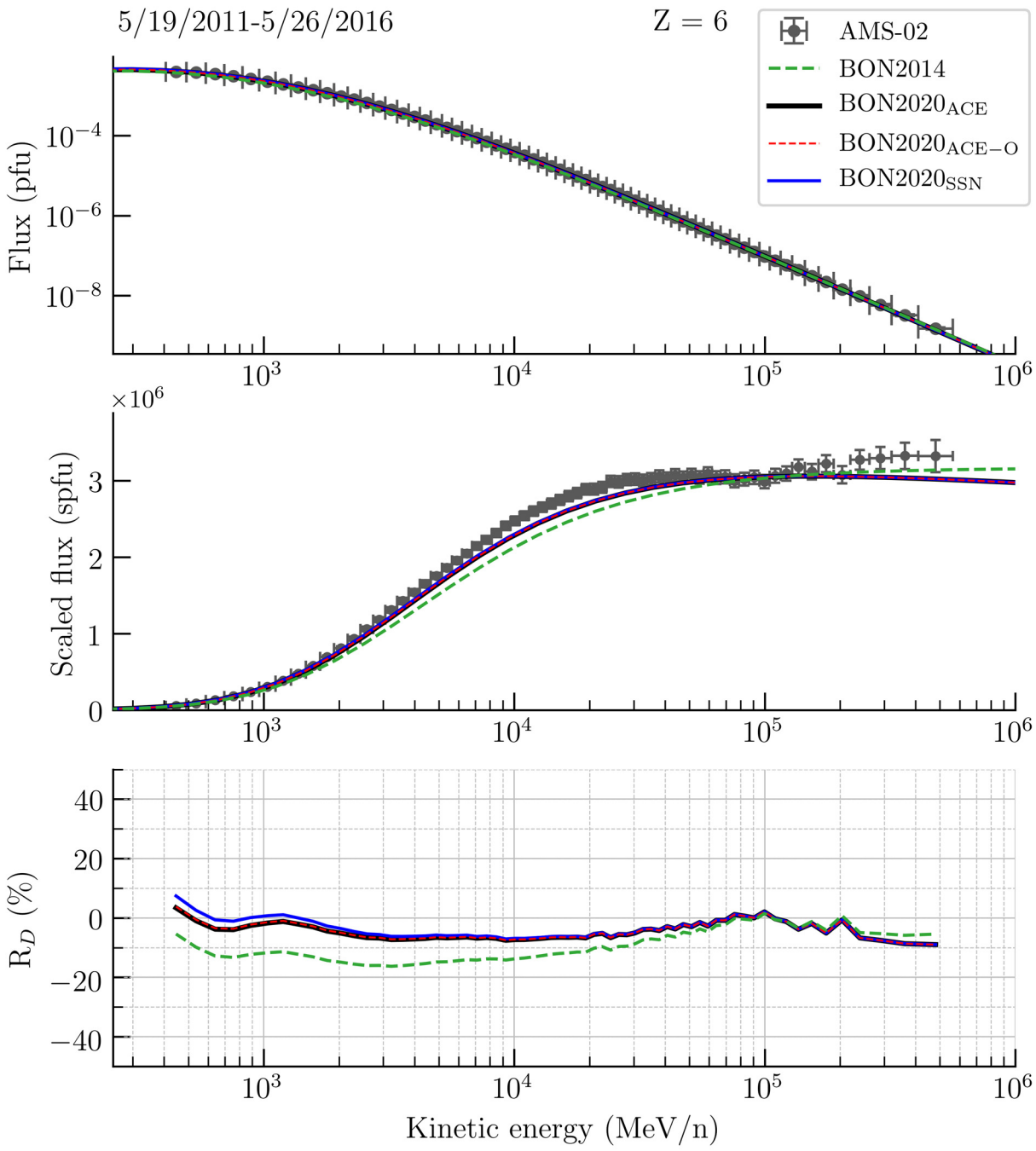

Figure D23. Comparison of model Z = 6 flux to AMS-02 measurements integrated over 5/19/2011-5/26/2016.

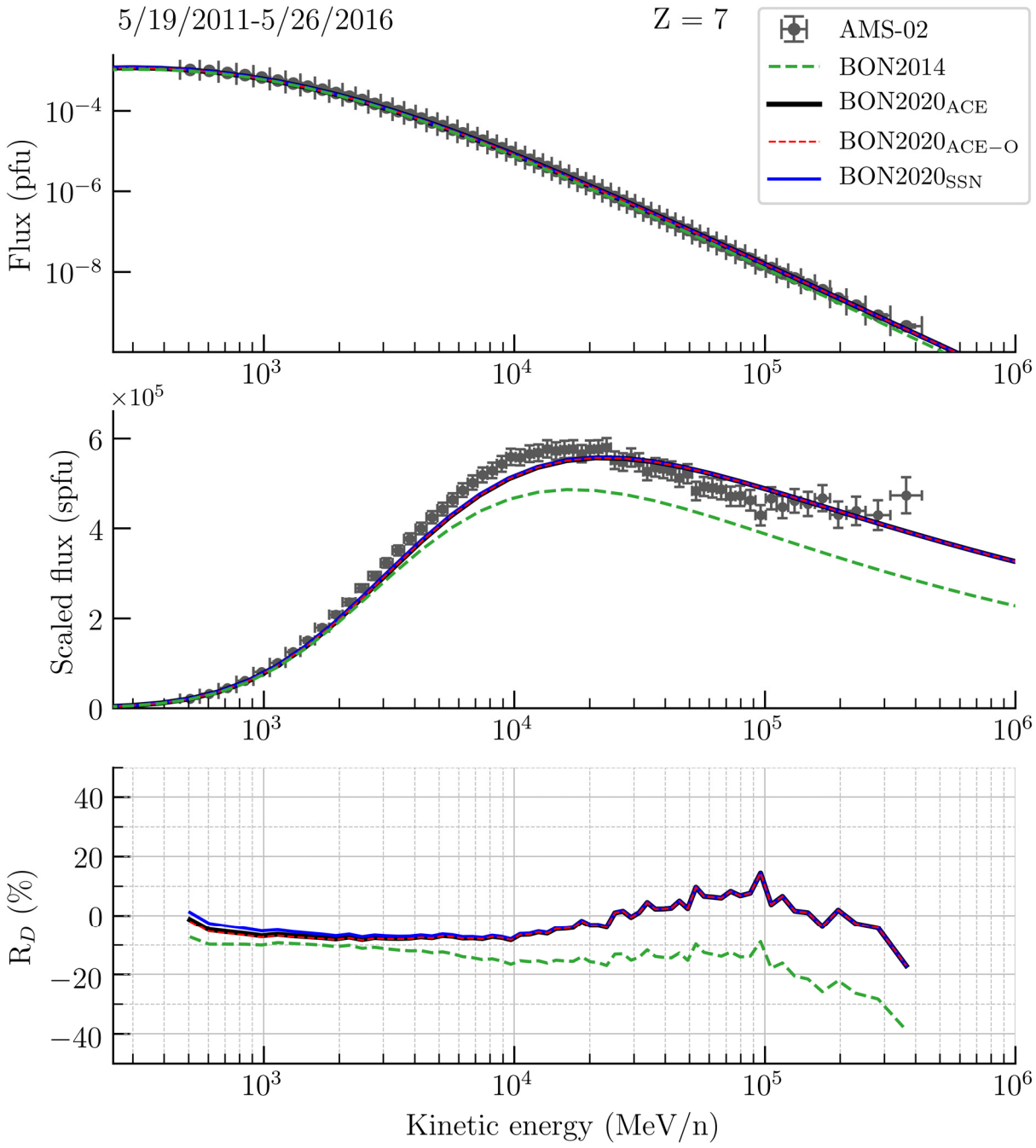

Figure D24. Comparison of model Z = 7 flux to AMS-02 measurements integrated over 5/19/2011-5/26/2016.

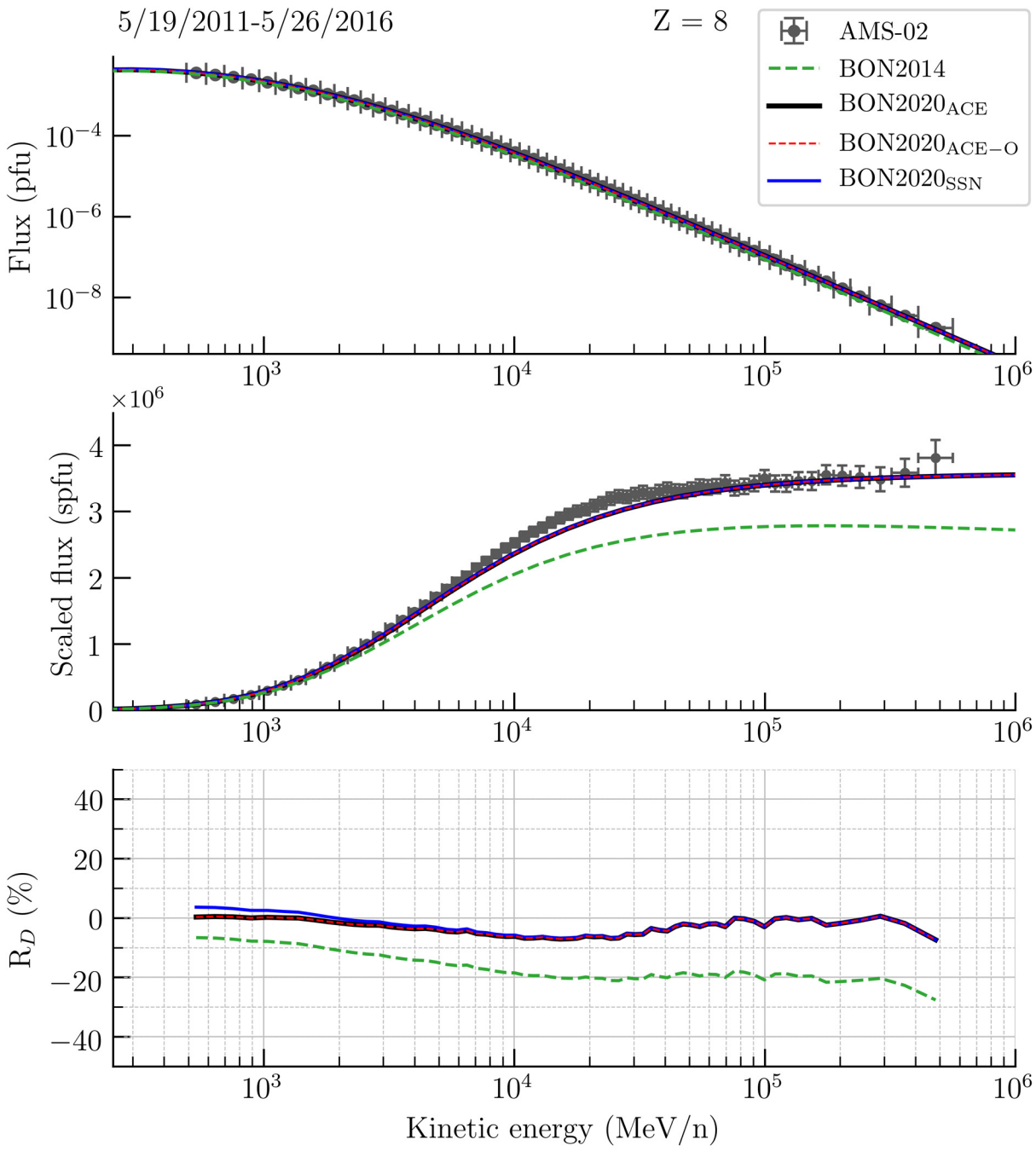

Figure D25. Comparison of model Z = 8 flux to AMS-02 measurements integrated over 5/19/2011-5/26/2016.

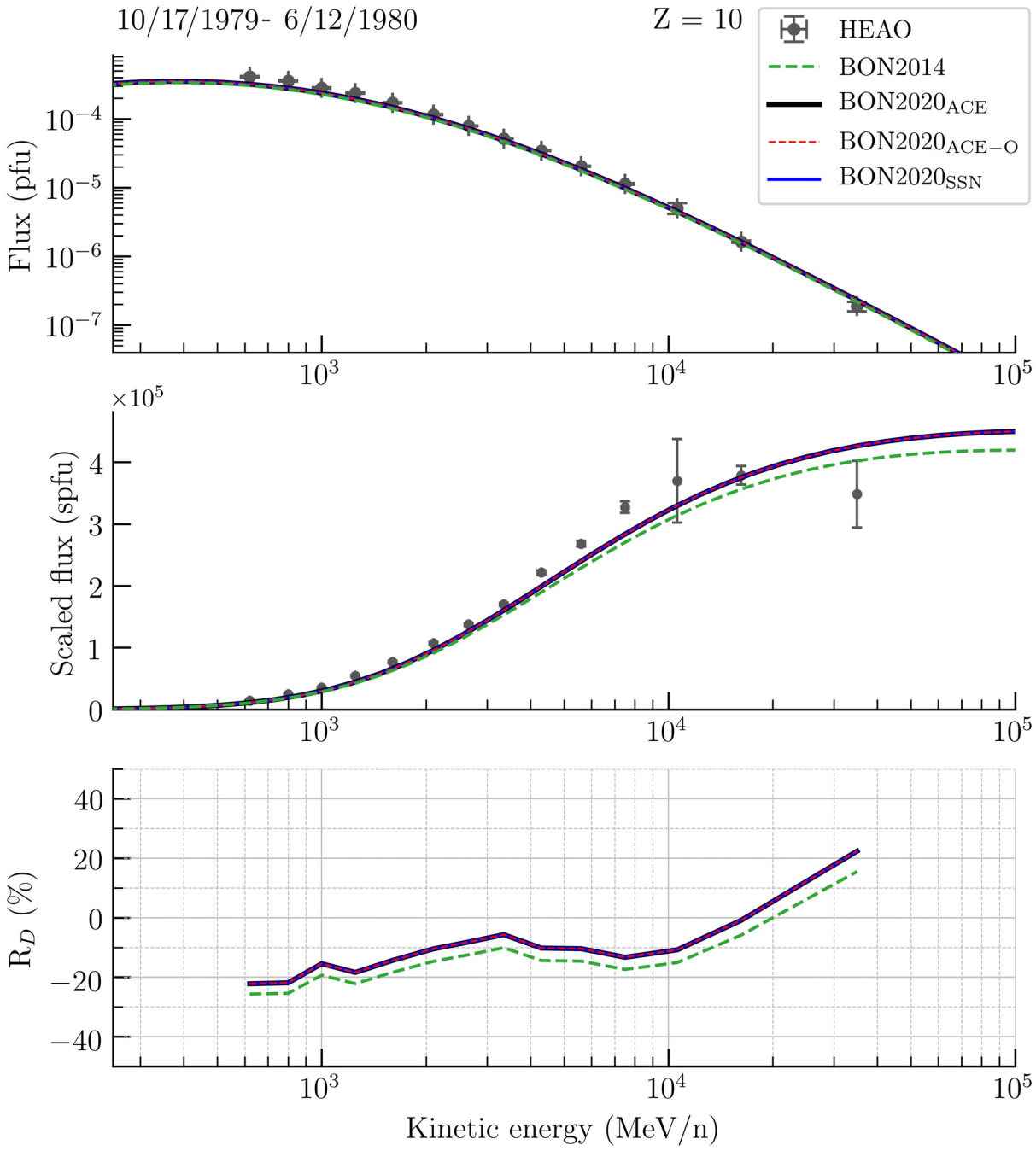

Figure D26. Comparison of model Z = 10 flux to HEAO measurements integrated over 10/17/1979-6/12/1980.

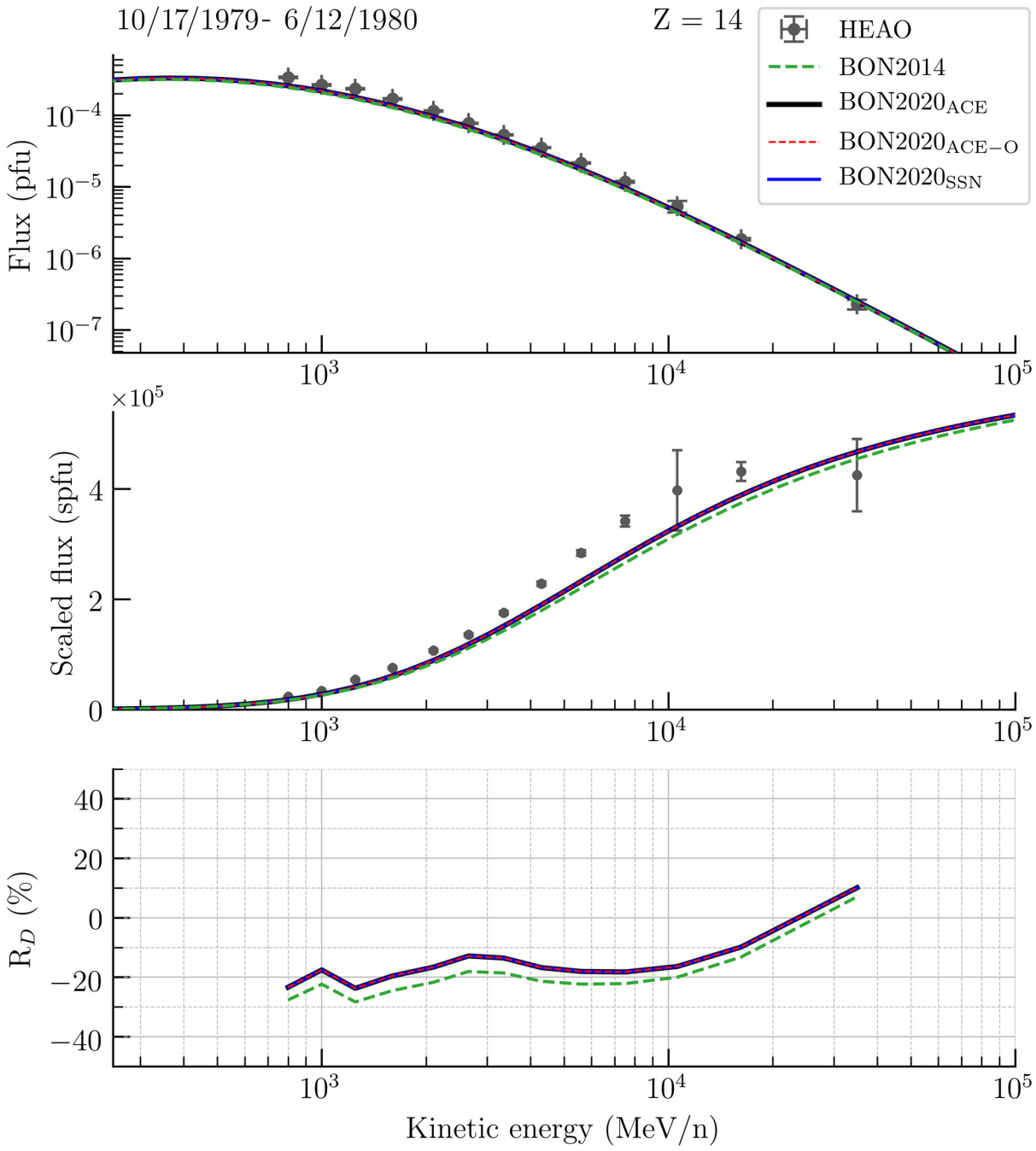

Figure D27. Comparison of model Z = 14 flux to HEAO measurements integrated over 10/17/1979-6/12/1980.

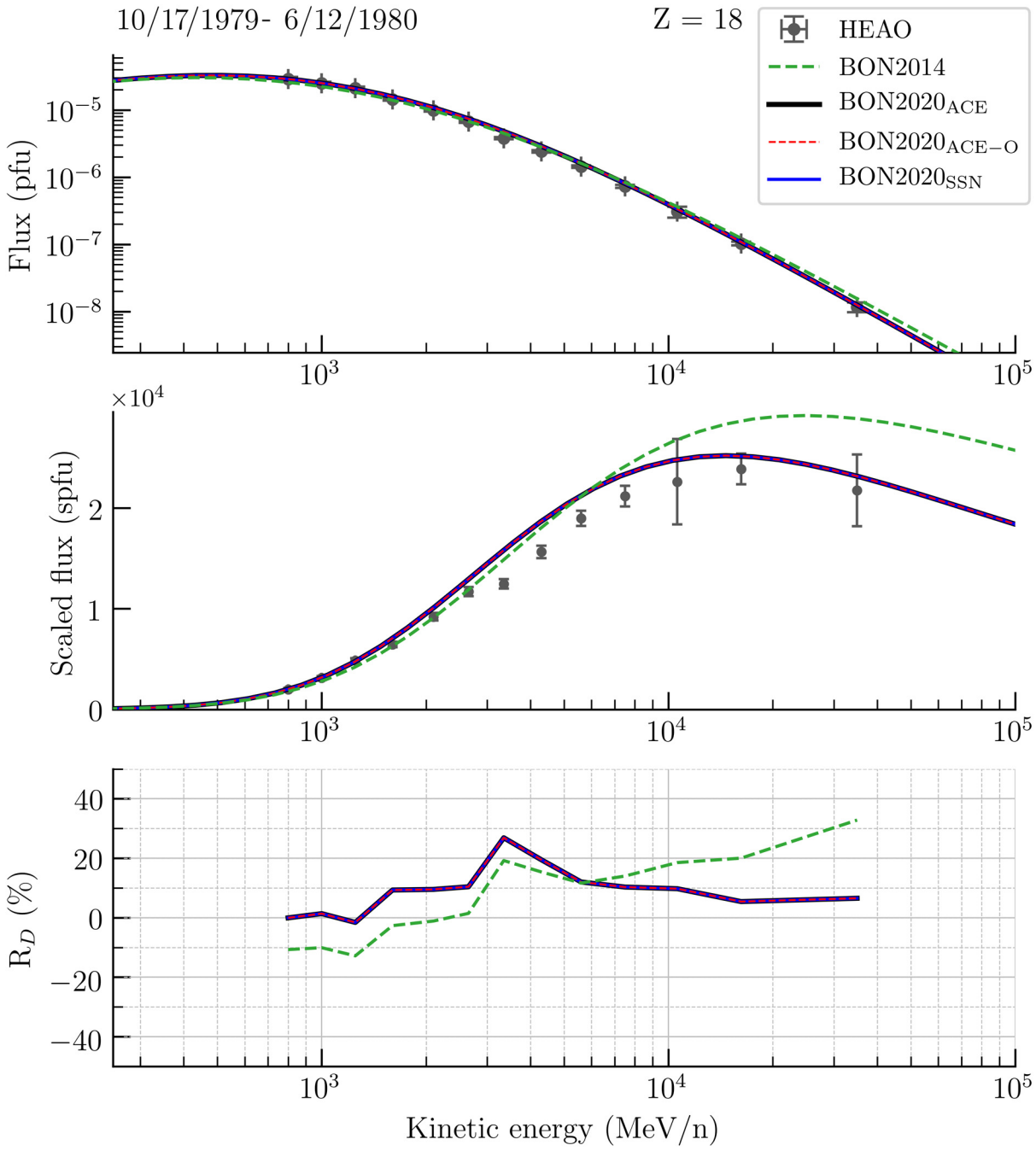

Figure D28. Comparison of model Z = 18 flux to HEAO measurements integrated over 10/17/1979-6/12/1980.

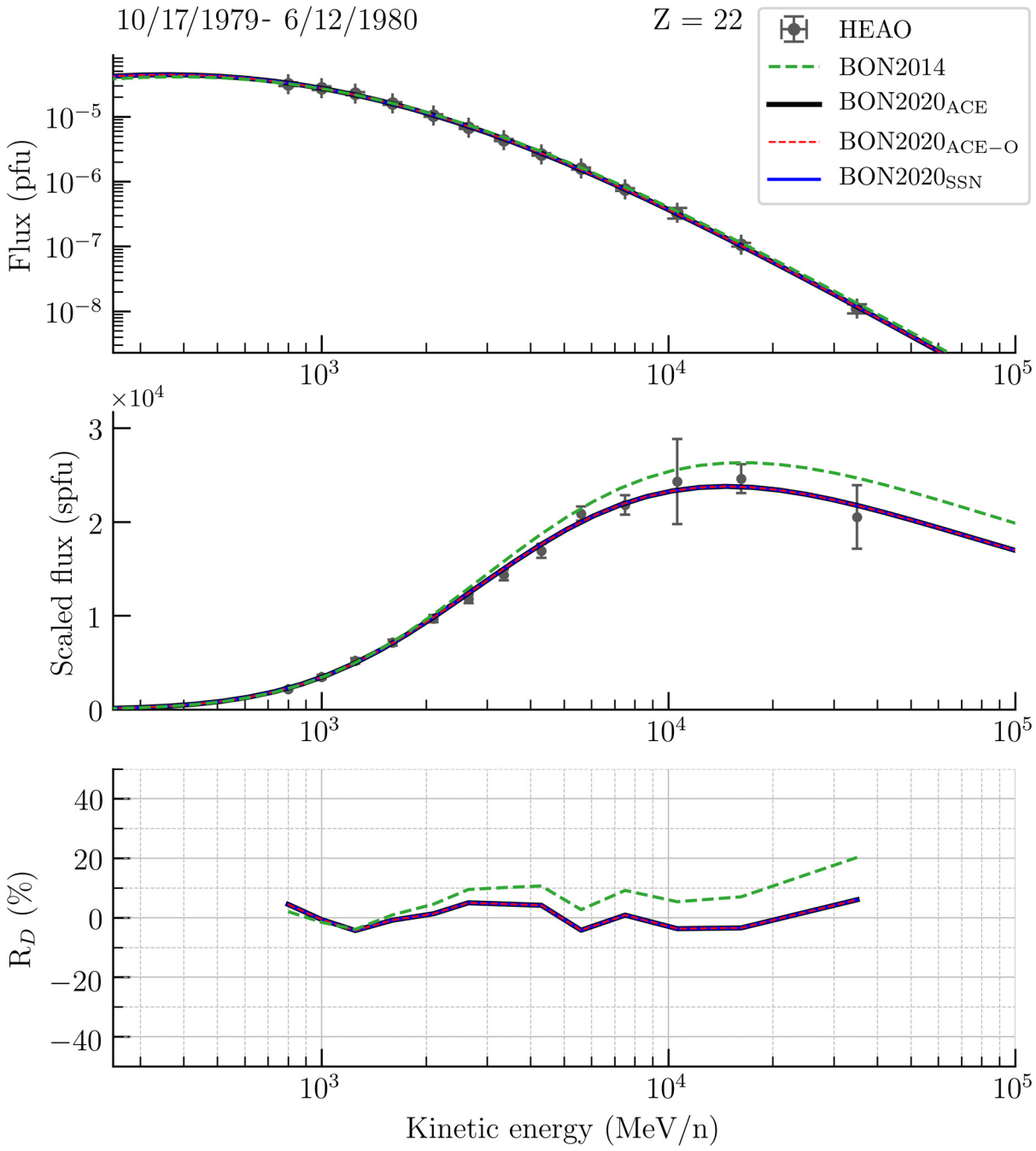

Figure D29. Comparison of model Z = 22 flux to HEAO measurements integrated over 10/17/1979-6/12/1980.

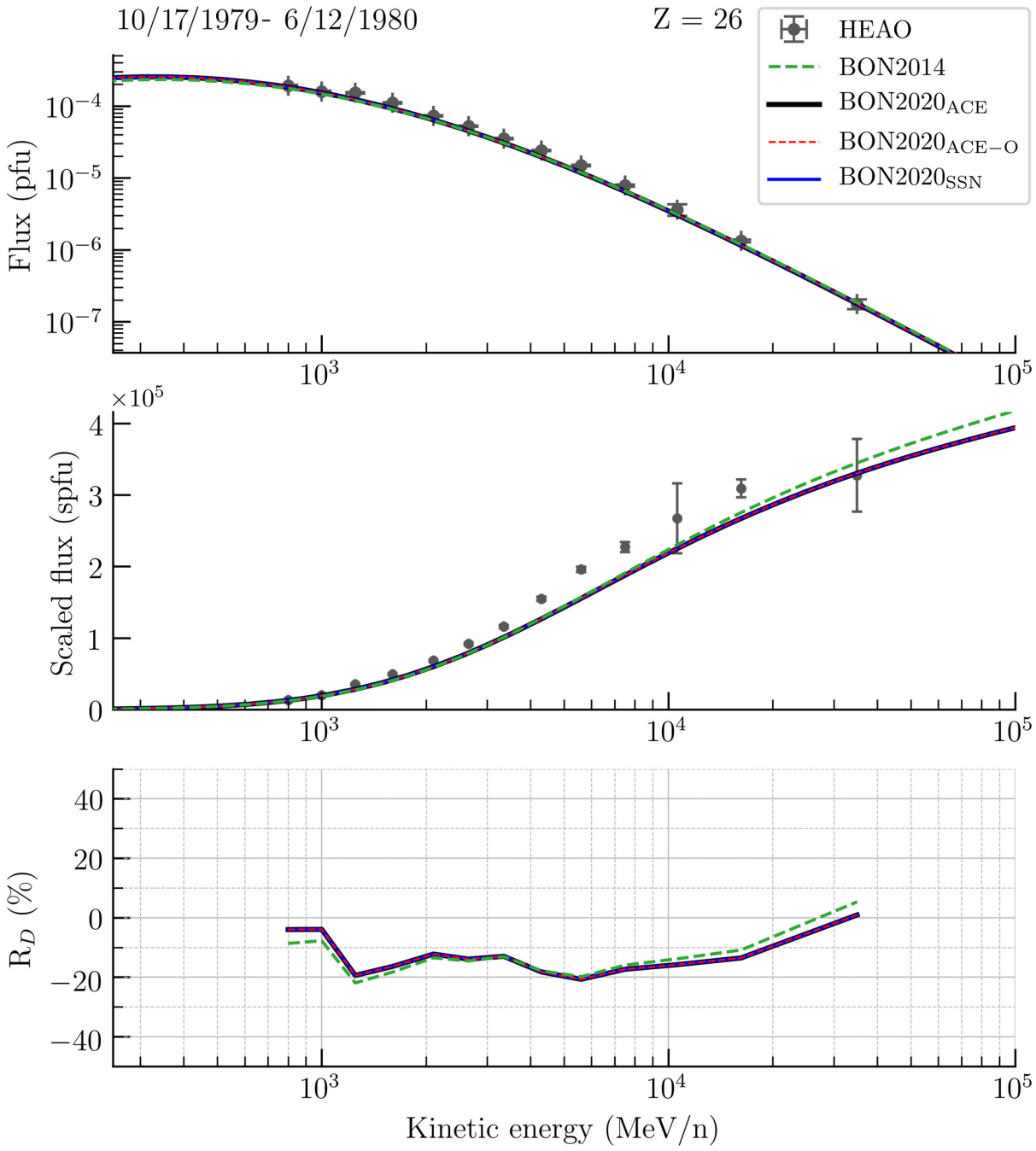

Figure D30. Comparison of model Z = 26 flux to HEAO measurements integrated over 10/17/1979-6/12/1980.

REPORT DOCUMENTATION PAGE

Form Approved
OMB No. 0704–0188

1. REPORT DATE *(DD-MM-YYYY)*	2. REPORT TYPE	3. DATES COVERED *(From - To)*
01-11-2019	Technical Publication	

4. TITLE AND SUBTITLE

The Badhwar-O'Neill 2020 Model

5a. CONTRACT NUMBER

5b. GRANT NUMBER

5c. PROGRAM ELEMENT NUMBER

6. AUTHOR(S)
Slaba, Tony C.; Whitman, Kathryn

5d. PROJECT NUMBER

5e. TASK NUMBER

5f. WORK UNIT NUMBER
089407.01.23

7. PERFORMING ORGANIZATION NAME(S) AND ADDRESS(ES)
NASA Langley Research Center
Hampton, Virginia 23681-2199

8. PERFORMING ORGANIZATION REPORT NUMBER
L–21072

9. SPONSORING/MONITORING AGENCY NAME(S) AND ADDRESS(ES)
National Aeronautics and Space Administration
Washington, DC 20546-0001

10. SPONSOR/MONITOR'S ACRONYM(S)
NASA

11. SPONSOR/MONITOR'S REPORT NUMBER(S)
NASA–TP–2019–220419

12. DISTRIBUTION/AVAILABILITY STATEMENT
Unclassified-Unlimited
Subject Category 93
Availability: NASA STI Program (757) 864-9658

13. SUPPLEMENTARY NOTES

14. ABSTRACT The Badhwar-O'Neill (BON) model has been used for some time to describe the galactic cosmic ray (GCR) environment encountered in deep space by astronauts and sensitive electronics. The most recent version of the model, BON2014, was calibrated to available measurements to reduce model errors for particles and energies of significance to astronaut exposure. Although subsequent studies showed the model to be reasonably accurate for such applications, modifications to the sunspot number (SSN) classification system and a large number of new high-precision measurements suggested the need to develop an improved and more capable model. In this work, the BON2020 model is described. The new model relies on daily integral flux from the Advanced Composition Explorer Cosmic Ray Isotope Spectrometer (ACE/CRIS) to describe solar activity. For time periods not covered by ACE/CRIS, the updated international SSN database is used. Parameters in the new model are calibrated to available data, which includes the new Alpha Magnetic Spectrometer (AMS-02) and Payload for Antimatter Matter Exploration and Light-nuclei Astrophysics (PAMELA) high-precision measurements. It is found that the BON2020 model is a significant improvement over BON2014. Systematic errors associated with BON2014 have been removed. The average relative error of the BON2020 model compared to all available measurements is found to be <1%, and BON2020 is found to be within +15% of a large fraction of the available measurements (26,269 of 27,646 __ 95%).

15. SUBJECT TERMS

GCR; Space Radiation; Cosmic rays; Radiation

16. SECURITY CLASSIFICATION OF:			17. LIMITATION OF ABSTRACT	18. NUMBER OF PAGES	19a. NAME OF RESPONSIBLE PERSON
a. REPORT	b. ABSTRACT	c. THIS PAGE			STI Help Desk (email: help@sti.nasa.gov)
U	U	U	UU	65	19b. TELEPHONE NUMBER *(Include area code)* (757) 864-9658